# Tor Vergata University

Department of Civil Engineering and Computer Science

GeoInformation Ph.D. program

XXVI Circle

UNIVERSITA' degli STUDI di ROMA
TOR VERGATA


# Multi-Sensor Remote Sensing Expert Systems for Detecting Anthropogenic Hydrocarbon pollution


Alireza Taravat

Supervisor: Prof. Fabio Del Frate


SUBMITTED IN PATRIAL FULFILMENT OF
THE REQUIREMENT FOR THE DEGREE OF
DOCTOR OF PHYLASOPHY AT
TOR VERGATA UNIVERSITY ROME, ITALY

November 2014

# Tor Vergata University

Department of Civil Engineering and Computer Science

GeoInformation Ph.D. program

XXVI Circle

UNIVERSITA' degli STUDI di ROMA
TOR VERGATA

The examining committee has read the thesis entitle "*Multi-Sensor Remote Sensing Expert Systems for Detecting Anthropogenic Hydrocarbon pollution*" by Alireza Taravat and recommended it in partial fulfilment of the requirements for the degree of Doctory of Philosophy.

Date: ………………

**GeoInformation XXVI Circle Ph.D. program coordinator:** *Prof. Domenico Solimini*

**Supervisor:** *Prof. Fabio Del Frate*

**Examining committee:**

Prof. Domenico Solimini

Prof. Giovanni Schiavon

Dr. Alessandro Burini

**Reviewers committee:**

Dr. Giuseppe Satalino

Dr. Michele Vespe

*This Ph.D. research is dedicated to my family (Maryam, Mom, Dad, My Sisters, and My Brother) with love. As I have already mentioned in my bachelor and master thesis, my family (although they are highly educated) don't read scientific things about GeoInformation, so if someone doesn't tell them about this, they'll never know. They still haven't noticed that these things are dedicated to them. This is my Ph.D. thesis – let's see how many more until they catch on. Maybe we can keep this a secret all the way to my professorship.*

*I would like to express my sincere gratitude to my advisor Professor Fabio Del Frate for the continuous support of my Ph.D. study and research, for his patience, motivation and enthusiasm. Besides my advisor, I would like to thank Professor Domenico Solimini for his encouragement, insightful comments, and his kindness.*

*Last but not the least, I thank my fellow labmates in EOLab Group for the discussions and for all the fun we have had in the last four years.*

# Contents

# Summary

As a major aspect of marine pollution, oil release into the sea has become a common phenomenon and it can have serious biological and economic impacts. Accurate detection and forecast of oil spill in a timely manner would be beneficial to resource management for monitoring the marine environment.

It is one of the most important applications for operational oceanography. It has been demonstrated that remote sensing is a tool that offers a non-destructive investigation method and has a significant added value to traditional methods.

This research presents different satellite sensors and oil spill detectability under varying conditions. In particular, I concentrate on the use of automatic approaches to detect oil spills in different imagery (in passive and active remote sensing systems). I conclude with a discussion of suggestions for further research with respect to oil spill detection systems.

In the first phase of my research, a study for examining the feasibility of passive remote sensing systems in order to detect oil spills pollutions has been done. The Landsat ETM+ images were used to study the oil spill in Gulf of Mexico. An attempt has been made to perform ratio operations to enhance the feature.

The study concluded that the bands difference between 660 and 560 nm, division at 660 and 560 and division at 825 and 560 nm, normalized by 480 nm provide the best result. Multilayer perceptron neural network classifier is used in order to perform a pixel-based supervised classification. The result indicates the potential of Landsat ETM+ data in oil spill detection.

In the second phase of my research, I have focused on active remote sensing systems for oil spill detection. Synthetic aperture radar (SAR) can provide

valuable synoptic information about the position and size of the oil spill due to its wide area coverage and day/night, and all-weather capabilities. Detection of oil spills from SAR imagery can be divided into three steps: (1) Dark feature detection, (2) Computation and extraction of physical and geometrical features characterizing the dark feature, and (3) accurate discrimination between oil spills and look-alikes such as ice, internal waves, kelp beds, natural organics, jellyfish, algae, low wind speed areas (wind speed < 3 m/s) and rain cells.

In fact, the extraction of the dark spots in the image is the first of three necessary steps, the other two being its characterization by using a set of features and the classification between oil spill and look-alike. Aside from the accuracy of the segmentation results, one of the most significant parameters for evaluating the performance in this context is the processing time which is necessary to provide the segmented image.

As a part of this research, I present a new fast, robust and effective automated method for oil-spill monitoring. A new approach has been generated from the combination of Weibull Multiplicative Model and neural network techniques to differentiate between dark spots and the background. First, the filter created based on Weibull Multiplicative Model is applied to each sub-image. Second, the sub-image is segmented by two different neural networks techniques (Pulsed Coupled Neural Networks and Multilayer Perceptron Neural Networks). As the last step, a very simple filtering process is used to eliminate the false targets. The proposed approaches were tested on 60 ENVISAT and ERS2 images which contained dark spots.

# Chapter I

# General Introduction

## A brief Overview of Oil spill

Petroleum products play an important role in modern society. There are typically ten to fifteen transfers involved in moving oil from the oil field to the final consumer. Oil spill scan occur during oil transportation or storage and spillage can occur in water, ice or on land. Marine oil spills can be highly dangerous since wind, waves and currents can scatter a large oil spill over a wide area within a few hours in the open sea (Fingas 2001). An oil spill may be due to a number of reasons, including transportation accidents (Figure. 1). In addition to accidents, the controlled release of oil by shipping operators and oil production platforms are major sources of oil spills (Gruner 1991). Environmental rules, regulations and strict operating procedures have been imposed to prevent oil spills, but these measures cannot completely eliminate the risk (Fingas 2001).

Figure. 1. Incidents can occur in bad weather, a fact that should be considered in contingency planning. (Environment Canada)

Once oil is spilled, it quickly spreads to form a thin layer on the water surface, known as an “oil slick”. As time passes, the oil slick becomes thinner, forming a layer known as a “sheen” which has a rainbow like appearance. Light oils are highly toxic but evaporate quickly. Heavy oils are less toxic but persist in the environment for a long time. Heavy oils can get mixed with pebbles and sandy beaches where they may remain for years (Environment Canada, 2007). Worldwide, fuels account for 48% of the total oil spilled into the sea worldwide, while crude oil spills account for 29% of the total (Brekke and Solberg 2005). The environmental impacts of oil spills can be considerable. Oil spills in water may severely affect the marine environment causing a decline in phytoplankton and other aquatic organisms.

The livelihood of many coastal people can be impacted by oil spills, particularly those whose livelihood is based on fishing and tourism (NOAA 2014). The movement of oil on land depends on various factors such as oil type, soil type and moisture content of the soil. Oil spilled on agricultural land can impact soil fertility and pollute ground water resources (Fingas 2001).

Normally, small-scale release of oil into the sea ascribed as “slick”, while large-scale ones called “spill” (Goodman 1989). More than 700 millions of gallons of oil released each year into ocean worldwide and about 50% of this amount is attributed to down to drain (Gradwohl 1995). 48% of the oil pollution is fuel oil and 29% is crude oil, tanker accidents contribute with only 5% of all pollution entering into the sea (Fingas 2001, Brekke and Solberg 2005). Although the discharge of is not always illegal. The oil discharge regulation (MARPOL 73/78) set that oil discharge into the sea are authorized below 15 parts per million, whereas in areas not identified as “special areas” this limit can be exceed. Oil on the surface cannot be observed clearly through fog and darkness (Fingas 2001). Accurate detection and forecast of oil spill in a timely manner would be beneficial to resource management for monitoring and conserve of the marine environment. It is one of the most important applications for operational oceanography.

## Types of Oil and their properties

Oil is a general term that describes a wide variety of natural substances of plant, animal, or mineral origin, as well as a range of synthetic compounds. The many different types of oil are made up of hundreds of major compounds and thousands of minor ones. As their composition varies, each type of oil or petroleum product has certain unique characteristics or properties. These properties influence how the oil behaves when it is spilled and determine the effects of the oil on living organisms in the environment (Fingas 2001).

Crude oils are mixtures of hydrocarbon compounds ranging from smaller, volatile compounds to very large, non-volatile compounds. This mixture of compounds varies according to the geological formation of the area in which the oil is found and strongly influences the properties of the oil. For example, crude oils that consist primarily of large compounds are viscous and dense.

Petroleum products such as gasoline or diesel fuel are mixtures of fewer compounds and thus their properties are more specific and less variable. Hydrocarbon compounds are composed of hydrogen and carbon, which are therefore the main elements in oils. Oils also contain varying amounts of sulphur, nitrogen, oxygen, and sometimes mineral salts, as well as trace metals such as nickel, vanadium, and chromium (Fingas 2001).

The following are the oils which are generally discussed in the related literature:

- A light crude oil: as produced in great abundance in western Canada or Louisiana
- A heavy crude oil: as imported to North America from Arabic countries
- An intermediate fuel oil (IFO): a mixture of a heavy residual oil and diesel fuel used primarily as a propulsion fuel for ships (the intermediate refers to the fact that the fuel is between a diesel and a heavy residual fuel)

- Bunker fuel: such as Bunker C which is a heavy residual fuel remaining after the production of gasoline and diesel fuel in refineries and often used in heating plants
- Crude oil emulsion: such as an emulsion of water in a medium crude oil
- Gasoline: as used in automobiles
- Diesel fuel: as used in trucks, trains, and buses

The properties of oil discussed here are viscosity, density, specific gravity, solubility, interfacial tension, and vapor pressure. Viscosity is the resistance to flow in a liquid. The lower the viscosity, the more readily the liquid flows. The viscosity of the oil is largely determined by the amount of lighter and heavier fractions that it contains. The greater the percentage of light components such as saturates and the lesser the amount of asphaltenes, the lower the viscosity. As with other physical properties, viscosity is affected by temperature, with a lower temperature giving a higher viscosity.

Density is the mass (weight) of a given volume of oil and is typically expressed in grams per cubic centimeter ($g/cm^3$). It is the property used by the petroleum industry to define light or heavy crude oils. Density is also important because it indicates whether a particular oil will float or sink in water. As the density of water is 1.0 $g/cm^3$ at 15°C and the density of most oils ranges from 0.7 to 0.99 $g/cm^3$, most oils will float on water. The density of oil increases with time, as the light fractions evaporate. Another measure of density is specific gravity, which is an oil’s relative density compared with that of water at 15°C. It is the same value as density at the same temperature.

Solubility in water is the measure of how much of an oil will dissolve in the water column on a molecular basis. Solubility is important in that the soluble fractions of the oil are sometimes toxic to aquatic life, especially at higher concentrations.

The oil/water interfacial tension, sometimes called surface tension, is the force of attraction or repulsion between the surface molecules of oil and water. Together with viscosity, surface tension is an indication of how rapidly and to what extent an oil will spread on water. The lower the interfacial tension with water, the greater the extent of spreading. In actual practice, the interfacial tension must be considered along with the viscosity because it has been found that interfacial tension alone does not account for spreading behavior.

The vapor pressure of an oil is a measure of how the oil partitions between the liquid and gas phases, or how much vapor is in the space above a given amount of liquid oil at a fixed temperature. Because oils are a mixture of many compounds, the vapor pressure changes as the oil weathers. Vapor pressure is difficult to measure and is not frequently used to assess oil spills.

## Oil in the Environment

When oil is spilled, a number of transformation processes occurs. The first is weathering, a series of processes whereby the physical and chemical properties of the oil change after the spill. The second is a group of processes related to the movement of oil in the environment. Spill modelling is also included in the section on oil movement. Weathering and movement processes can overlap, with weathering strongly influencing how oil is moving in the environment and vice versa. These processes depend very much on the type of oil spilled and the weather conditions during and after the spill.

The processes included in weathering are evaporation, emulsification, natural dispersion, dissolution, photo oxidation, and biodegradation. Evaporation is usually the most important weathering process. It has the greatest effect on the amount of oil remaining on water or land after a spill. Over a period of several days, a light fuel such as gasoline evaporates completely at temperatures above freezing, whereas only a small percentage of a heavier Bunker C oil evaporates. Emulsification (Figure. 2) is the process by which one liquid is dispersed into another one in the form of small droplets. Water droplets can remain in an oil layer in a stable form and the resulting material is completely different. These water-in-oil emulsions are sometimes called “mousse” or “chocolate mousse” as they resemble this dessert. Natural dispersion occurs when fine droplets of oil are transferred into the water column by wave action or turbulence.

Photo oxidation can change the composition of an oil. It occurs when the sun’s action on an oil slick causes oxygen and carbons to combine and form new products that may be resins. A large number of microorganisms are capable of degrading petroleum hydrocarbons. Many species of bacteria, fungi, and yeasts metabolize petroleum hydrocarbons as a food energy source. Bacteria and other degrading organisms are most abundant on land in areas where there have been petroleum seeps, although these microorganisms are found everywhere in the environment.

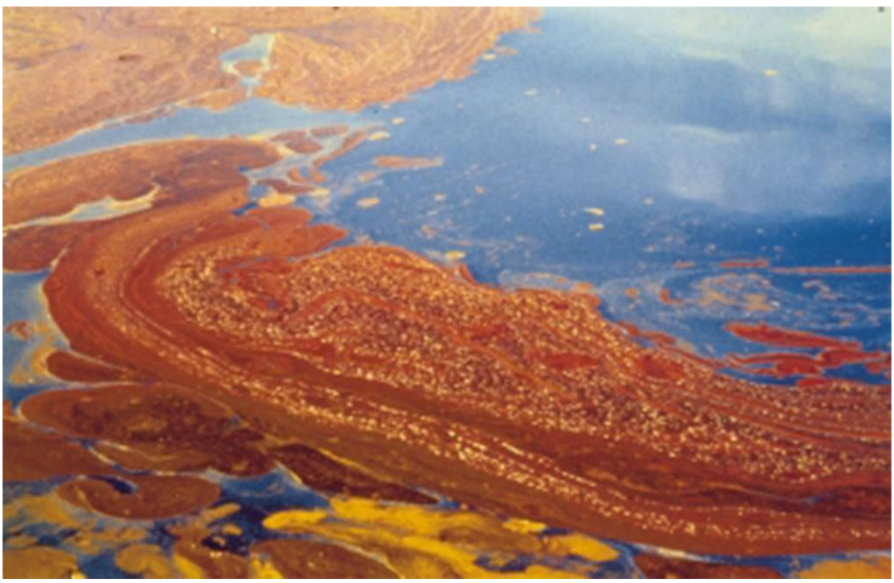

Figure. 2. A close-up of emulsified oil showing the patchiness of some slicks (NOAA 2014)

Oil spreads to a lesser extent and more slowly on land than on water. Spreading may be defined as the horizontal expansion of an oil slick due to gravity, inertia, viscous forces and interfacial tension.

Oil from controlled release experiments divides quickly into a thick region which contains the majority of the oil, surrounded by a much larger, thin region of surface sheen.

In calm water with minimal surface currents the driving forces of gravity and surface tension are opposed by inertial and viscous forces. Initially gravity and inertial forces dominate, later gravity and viscous forces, and finally surface tension and viscous forces (Fay 1971).

The relative magnitude of these forces, and thus the spreading rate of a slick, varies with the volume, age, density and viscosity of the oil, and with the amount of surface active materials present in the oil and sea-water.

Winds and currents also spread the oil out and speed up the process. Oil slicks will elongate in the direction of the wind and currents, and as spreading progresses, take on many shapes depending on the driving forces.

Oil sheens often precede heavier or thicker oil concentrations. If the winds are high (more than 20 km/h), the sheen may separate from thicker slicks and move downwind. In addition to their natural tendency to spread, oil slicks on water are moved along the water surface, primarily by surface currents and winds (Fay 1971).

If the oil slick is close to land and the wind speed is less than 10 km/h, the slick generally moves at a rate that is 100% of the surface current and approximately 3% of the wind speed (Fay 1971).

# Remote Sensing of Oil Spills

Visual detection of an oil spill is not reliable as oil can be confused with other substances, e.g. sea weeds and fish sperm. Moreover, oil on the surface cannot be observed clearly through fog and darkness (Fingas 2001). Remote sensing can be used for detecting and monitoring oil spills. Remote sensing technologies for oil spill surveillance have been reviewed by many authors.

Laser fluorosensors can detect oil under the water surface and on various backgrounds including snow or ice (Brown and Fingas 2003a). (Fingas, Brown et al. 1998) found that no single sensor can give all the information required for oil spill contingency planning. Currently, many coastal nations have proper maritime surveillance systems in place to detect and monitor oil spill (Brown and Fingas 2005).

There are many sensors available to detect oil spills on various kinds of surfaces. Multi-temporal imaging captured by remote sensing sensors can provide important information required to model the spread of an oil spill (Natural Resources Canada 2014). Oil spill models may be useful for cleanup operations and controlling the oil spill.

Remote sensing devices for oil spill detection include infrared video and photography, thermal infrared imaging, airborne laser fluorosensors, airborne and spaceborne optical sensors, and airborne and space-borne SAR (Natural Resources Canada 2014).

Satellite remote sensing suffers from low spatial and temporal resolution although it provides a synoptic view and a more cost effective system than an airborne platform, which is typically used for oil spill surveillance.

Sensors can provide the following information for oil spill contingency planning (Gruner 1991):

- The location and spread of an oil spill over a large area
- The thickness distribution of an oil spill to estimate the quantity of spilled oil
- A classification of the oil type in order to estimate environmental damage and to take appropriate response activities
- Timely and valuable information to assist in clean-up operations

Infrared, visible and UV sensors will not be able to detect oil in inclement weather such as heavy rain or fog (Goodman 1994). A brief description of sensors useful for oil spill detection is given in the following sections.

### Visible Sensors

Thermal and visible scanning systems as well as aerial photography were commonly used in airborne remote sensing sensors at the start of 1970 (Wadsworth, Looyen et al. 1992). Visible sensors (passive sensors operating in the visible region of the light) are still widely used in oil spill remote sensing despite many shortcomings. The reflectance of oil is higher than that of water but oil also absorbs some radiation in the visible region. Sun-glint and wind sheen may create a similar impression to an oil sheen. Moreover, sea weeds and a darker shoreline may be mistaken for oil. Visible sensors are less costly and easy to use; therefore, they are often used for preliminary screening in coastal areas (Goodman 1994, Fingas, Brown et al. 1998).

Improvements in sensor technologies have led to the development of hyperspectral sensors such as Airborne Visible/Infrared Imaging Spectrometer (AVIRIS) and Airborne Imaging Spectrometer for Applications (AISA). A hyperspectral image consists of ten to hundreds of spectral bands and can provide a spectral signature for an object. However, conventional techniques for multispectral data analysis cannot be used to investigate hyperspectral images (Landgrebe 2003). (Plaza, Pérez et al. 2001) have reported the use of hyperspectral data for oil spill detection. The extensive spectral information can be used to discriminate between light and crude oil. Minute concentrations of crude oil can be detected using hyperspectral images.

## Infrared Sensors

The oil absorbs solar radiation and emits some part of it as the thermal energy mainly in the thermal infrared region (8-14 μm). Oil has a distinctively different spectral signature in the thermal infrared region compared to the background water in infrared region (Salisbury, Daria et al. 1993).

TIR is typically used for oil spill detection in the IR region. Thick oil absorbs greater amounts of radiation and as a result it appears hot in TIR. The oil of intermediate thickness appears cool in this region, but thin sheens cannot be detected in TIR. The thickness of the minimum detectable layer lies between 20 and 70 μm (Neville, Thompson et al. 1979, Belore 1982, Hurford 1989, Goodman 1994). A plausible theory is that a moderately thin layer of oil on the water surface causes destructive interference of the thermal radiation waves emitted by the water, thereby reducing the amount of thermal radiation emitted by the water (Fingas 2001).

The change from hot to cold layer occurs between 50 and 150 μm (Fingas and Brown 1997). At night, the reverse behavior is observed: heat loss in oil is faster than in water and therefore, thick oil appears cooler than water (Samberg 2005). Thus, infrared sensors can provide some information about the relative thickness of oil slicks. These sensors are unable to detect emulsions of oil in water as emulsions contain 70% of water and thermal properties of emulsion are similar to the background water (Fingas and Brown 1997).

Thermal radiation from sea weeds and the shoreline appear similar to the radiation arising from the oil which may lead to a false targets result. The infrared sensors are relatively cheap remote sensing technologies which can be used to detect oil spills and are hence widely used systems for oil spill surveillance (Brown and Fingas 2005).

Infrared cameras are now very common and commercial units are available from several manufacturers. Scanners with infrared detectors have been used recently. The older type of infrared detectors, however, required cooling to avoid thermal noise, which would overwhelm any useful signal. Liquid nitrogen, which provides about 4 hours of service, was traditionally used to cool the detector. New, smaller sensors use closed-cycle or Sterling coolers, which operate on the cooling effect created by an expanding gas. While a gas cylinder or compressor must be transported with this type of cooler, refills or servicing may not be required for days at a time (Goodman 1994).

Most infrared sensing of oil spills takes place in the thermal infrared at wavelengths of 8 to 14µm. One sensor, which is designed as a fixed-mounted unit, uses the differential reflectance of oil and water at 2.5 and 3.1µm (Seakem Oceanography 1988). Tests of a midband infrared system (3.4 to 5.4µm) over the Tenyo Maru oil spill showed no detection in this range.

Specific studies in the thermal infrared (8 to 14µm) show that there is no useful spectral structure in this region (Salisbury, Daria et al. 1993). Tests of a number of infrared systems show that spatial resolution is extremely important when the oil is distributed in windrows and patches, emulsions are not always visible in the IR, and cameras operating in the 3- to 5-µm range are only marginally useful. The relative thickness information in the thermal infrared can be used to direct countermeasures equipment to thicker portions of the oil slick, but is not useful forensically. Oil detection in the infrared is not effective, however, as several false targets can interfere, including seaweed, shoreline, and oceanic fronts (Fingas and Brown 1997).

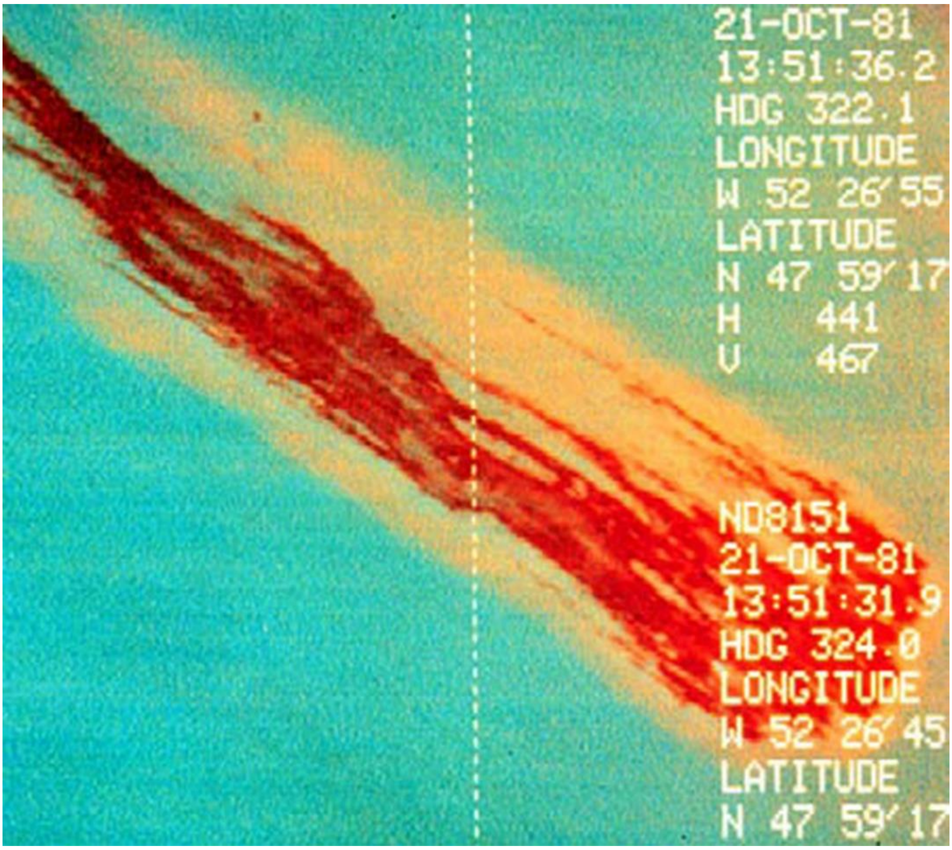


Figure. 3. An infrared image of a slick as taken in 1981. Note the annotation providing essential times and positions.

## Ultraviolet Sensors

UV scanners capture the ultraviolet radiation reflected by the sea surface. A UV sensor is a passive sensor as it uses reflected sunlight in the ultraviolet region (0.32-0.38 micron) for detecting oil spills. Oil has stronger reflectivity than water in the UV region. Even a very thin oil film has a strong reflectance in the UV region. Very thin sheens of thickness (less than 0.1 micron) can be detected using a UV sensor. However, UV sensors cannot detect oil thickness greater than 10 micron. UV images can only give information about the relative thickness of the oil slick (Gruner 1991).

Figure. 4. Under UV light, the Gulf of Mexico oil spill lights up orange-yellow on the beaches of Gulf Islands National Seashore while clean sand glows purple in a long-exposure picture.

False detection may occur due to the wind sheen, sun glint and sea weeds. Interferences in UV are different from IR and a combination of these two techniques can provide improved results for oil spill detection (Goodman 1994, Fingas and Brown 1997). The ultraviolet images can be overlayed with infrared images to generate an oil spill relative thickness map. UV images are based on the reflected sunlight and hence cannot operate in the night. Most laser fluorosensors used for oil spill detection employ an ultraviolet laser emitting between 300 and 355 nm (Barbini 1991, Calleri 1993, Anderson, Neff et al. 1994, Fingas and Brown 1997).

These excitation wavelengths are a compromise in that they can excite all three classes of oil with reasonable efficiency. Shorter-wavelength lasers would excite lighter oils efficiently but are less efficient at exciting crude and heavy refined oils. Figure 5 shows the discrimination in spectra obtained using a fluorosensor targeting three fuels with nearly identical physical properties. Such discrimination is not the case with heavier oils.

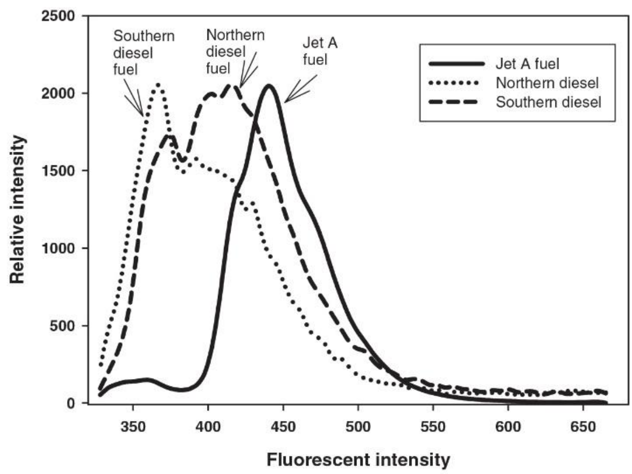


Figure. 5. Spectra of three fuels with similar physical properties showing the spectral differences in them using a fluorosensor.

There are several reasonably priced, commercially available ultraviolet lasers in the 300 to 355 nm region, including the XeCl excimer laser (308 nm), the nitrogen laser (337 nm), the XeF excimer laser (351 nm), and the frequency-tripled Nd:YAG (355 nm). With excitation in this wavelength region, there exists a spectrally broad fluorescent return due to organic matter, centered at 420 nm.

This is known as Gelbstoff or yellow matter and must be accounted for. The signal due to Gelbstoff disappears when the oil layer is optically thick (10 to 20μm). It can, however, be an interfering signal when attempting to detect thin films of light oils on water. Typically, crude oil fluorescence return is in the region of 400 to 550 nm, with the maximum centered in the 480 nm region.

Laser fluorosensors have significant potential for the remote sensing of petroleum oils because they can discriminate between oiled and unoiled weeds and detect oil in a variety of marine and terrestrial environments including on water, snow, ice, and beaches. Tests on shorelines show that this technique has been very successful (Dick 1992).

## Radiometers

Microwave radiometers detect the presence of an oil film on water by measuring an interference pattern excited by the radiation from space. The apparent emissivity factor of water is 0.4 compared to 0.8 for oil (O'Neil 1983, Ulaby 1989). This passive device can detect this difference in emissivity and could therefore be used to detect oil. In addition, as the signal changes with thickness, in theory, the device could be used to measure thickness.

This detection method has not been very successful in the field, however, as several environmental and oil specific parameters must be known. In addition, the signal return is dependent on oil thickness but in a cyclical fashion.

A given signal strength can imply any one of two or three signal film thicknesses within a given slick. Microwave energy emission is greatest when the effective thickness of the oil equals an odd multiple of one quarter of the wavelength of the observed energy. Biogenic materials also interfere, and the signal-to-noise ratio is low. In addition, it is difficult to achieve high spatial resolution (might need resolution in meters rather than the typical tens of meters for a radiometer) (Goodman 1994).

In summary, passive microwave radiometers may have potential as all-weather oil sensors. Their potential as a reliable device for measuring slick thickness, however, is uncertain at this time.

## Radar

Capillary waves on the ocean reflect radar energy, producing a “bright” image known as sea clutter. Since oil on the sea surface dampens capillary waves, the presence of an oil slick can be detected as a “dark” sea or one with an absence of this sea clutter (Nunziata 2008). Unfortunately, the oil slick is not the only phenomenon detected in this way. There are many interferences or false targets, including freshwater slicks, wind slicks (calms), wave shadows behind land or structures, seaweed beds that calm the water just above them, glacial flour, biogenic oils, and whale and fish sperm (Frysinger 1992, Gens 2008). Despite these limitations, radar is an important tool for oil spill remote sensing because it is the only sensor that can be used for searches of large areas and it is one of the few sensors that can “see” at night and through clouds or fog.

The two basic types of imaging radar that can be used to detect oil spills and for environmental remote sensing in general are Synthetic Aperture Radar (SAR) and Side-Looking Airborne Radar (SLAR). SLAR is an older but less expensive technology that uses a long antenna to achieve spatial resolution.

Search radar systems, such as those frequently used by the military, cannot be used for oil spills because they usually remove the clutter signal, which is the primary signal of interest for oil spill detection. Furthermore, the signal processing of this type of radar is optimized to pinpoint small, hard objects, such as periscopes. This signal processing is very detrimental to oil spill detection.

SLAR has predominated airborne oil spill remote sensing, primarily because of the lower price (Dyring 2004, Zielinski 2004). There is some recognition among the operators that SLAR is very subject to false hits, but solutions are not offered. Experimental work on oil spills has shown that X-band radar yields better data than L- or C-band radar (Intera Technologies 1984).

It has also been shown that vertical antenna polarizations for both transmission and reception (VV) yield better results than other configurations (Intera Technologies 1984, Macklin 1992). The ability of radar to detect oil is also limited by sea state.

Sea states that are too low will not produce enough sea clutter in the surrounding sea to contrast to the oil, and very high seas will scatter radar sufficiently to block detection inside the troughs. Indications are that minimum wind speeds of 1.5 m/s (~3 knots) are required to allow detectability, and a maximum wind speed of 6 m/s (~12 knots) will again remove the effect (Huhnerfuss, Alpers et al. 1996, Marghany, Cracknell et al. 2009).

The most accepted limits are 1.5 m/s (~3 knots) to 10 m/s (~20 knots). This limits the environmental window of application of radar for detecting oil slicks. Gade et al. studied the difference between extensive systems from a space-borne mission and a helicopter-borne system (Gade, Alpers et al. 1997). They found that at high winds, it was not possible to discriminate biogenic slicks from oil. At low-wind speeds, it was found that images in the L-band showed discrimination. Under these conditions, the biogenic material showed greater damping behavior in the L-band. Okamoto et al. studied the use of ERS-1 using an artificial oil and found that an image was detected at a wind speed of 11m/s, but not at 13.7 m/s (Okamoto 1996).

SAR uses the forward motion of the aircraft to synthesize a very long antenna, thereby achieving very good spatial resolution, which is independent of range, with the disadvantage of requiring sophisticated electronic processing. Though inherently more expensive, the SAR has greater range and resolution than the SLAR. In fact, comparative tests show that SAR is vastly superior (Bartsch 1987, Fingas and Brown 1997).

SAR can be polarimetric imaging that is horizontal-horizontal (HH), vertical-vertical (VV), and cross combinations of these. Several researchers have shown that VV is best for oil spill detection and discrimination (Migliaccio 2007). Migliaccio et al. showed that the co-polarized phase differenced for example, the difference between the HH and VV phases can be used to discriminate oil slicks from biogenic slicks (Migliaccio 2007). A larger standard deviation for the slick, compared to the sea, typically indicates that it is oil.

In summary, radar optimized for oil spills is useful in oil spill remote sensing, particularly for searches of large areas and for nighttime or foul weather work. The technique is highly prone to false targets, however, and is limited to a narrow range of wind speeds. Because of the all-weather and day night capability, radar is now the most common means of remote sensing.

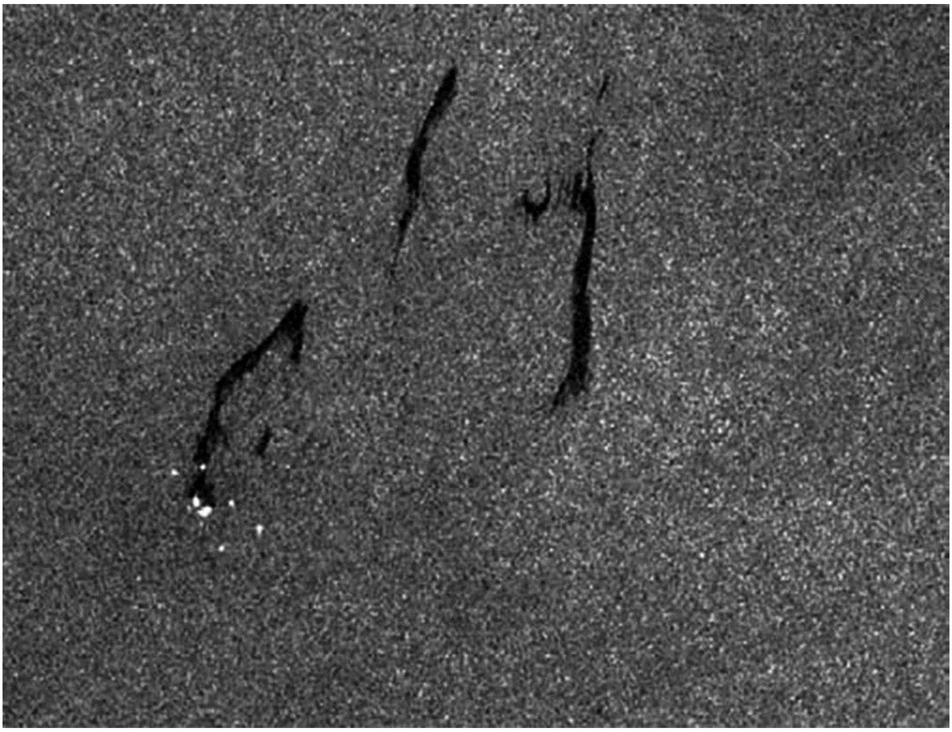

Figure. 6. A satellite Radarsat-I image of a large area of sea during the raising of the Irving Whale barge. These dark areas are actually oil, as confirmed by ground observation. The white spots in the center are ships.

Figure. 7. An image of the source of the oil shown in Figure 6. The ships shown here appear as white spots in the radar image in Figure 6. Photography by Environment Canada.

# Introduction to Machine Learning algorithms

Machine learning algorithms attempt to identify patterns and interrelationships among variables in a data set, usually by the use of some form of inductive generalization. The field of machine learning is vast and interdisciplinary, encompassing fields from biology, mathematics, computer science, and engineering, and I will therefore provide only a cursory review of the salient issues and considerations. The interested reader is encouraged to consult excellent references (V. Vapnik 1998, D. J. C. MacKay 2003, C. M. Bishop 2007, S. Haykin 2008) for further information.

## Artificial Neural Networks (ANNs)

Artificial Neural Networks (ANNs) are computational modeling tools that have recently emerged and found extensive acceptance in many disciplines for modeling complex real-world problems. ANNs may be defined as structures comprised of densely inter-connected adaptive simple processing elements (called artificial neurons or nodes) that are capable of performing massively parallel computations for data processing and knowledge representation (Hecht Nielsen 1988, Schalkoff 1997).

Although ANNs are drastic abstractions of the biological counterparts, the idea of ANNs is not to replicate the operation of the biological systems but to make use of what is known about the functionality of the biological networks for solving complex problems. The attractiveness of ANNs comes from the remarkable information processing characteristics of the biological system such as nonlinearity, high parallelism, robustness, fault and failure tolerance, learning, ability to handle imprecise and fuzzy information, and their capability to generalize (Jain 1996).

Artificial models possessing such characteristics are desirable because (Schalkoff 1997):

- Nonlinearity allows better fit to the data,
- Noise insensitivity provides accurate prediction in the presence of uncertain data and measurement errors,
- High parallelism implies fast processing and hardware failure-tolerance,
- Learning and adaptively allow the system to update (modify) its internal structure in response to changing environment,
- Generalization enables application of the model to unlearned data. The main objective of ANN-based computing (neurocomputing) is to develop mathematical algorithms that will enable ANNs to learn by mimicking information processing and knowledge acquisition in the human brain.

ANN-based models are empirical in nature, however they can provide practically accurate solutions for precisely or imprecisely formulated problems and for phenomena that are only understood through experimental data and field observations.

In 1958, Rosenblatt introduced the mechanics of the single artificial neuron and introduced the 'Perceptron' to solve problems in the area of character recognition (Hecht Nielsen 1988). Basic findings from the biological neuron operation enabled early researchers to model the operation of simple artificial neurons. An artificial processing neuron receives inputs as stimuli from the environment, combines them in a special way to form an input ($\xi$), passes that over through a linear threshold gate, and transmits the (output, y) signal forward to another neuron or the environment, as shown in Fig. 8. Only when e exceeds (i.e., is stronger than) the neuron's threshold limit (also called bias, b), will the neuron fire (i.e, becomes activated). Commonly, linear neuron dynamics are assumed for calculating ξ (S. Haykin 2008). The net input is computed as the inner (dot) product of the input signals (x) impinging on the neuron and their strengths (w). For (n) signals, the perceptron neuron operation is expressed as:

$$y = \begin{cases} 1, & if \sum_{i=1}^{n} w_i x_i \geq b, \\ 0, & if \sum_{i=1}^{n} w_i x_i < b, \end{cases}$$

with 1 indicating 'on' and 0 indicating 'off (Fig. 8), or class A and B, respectively, in solving classification problems. Positive connection weights (wi > 0) enhance the net signal (ξ) and excite the neuron, and the link is called excitory, whereas negative weights reduce ξ and inhibit the neuron activity, and the link is called inhibitory.

The system comprised of an artificial neuron and the inputs as shown in Fig. 8 is called the Perceptron which establishes a mapping between the inputs activity (stimuli) and the output signal. In the mentioned equation, the neuron threshold may be considered as an additional input node whose value is always unity (i.e., x = 1) and its connection weight is equal to b.

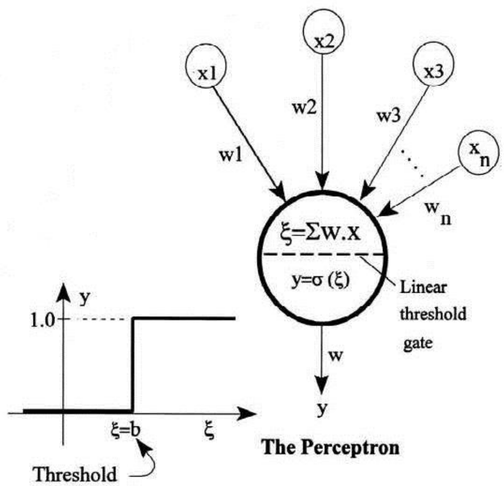


Figure. 8. Signal interaction from n neurons and analogy to signal summing in an artificial neuron comprising the single layer perceptron

## Feedforward Neural Networks

Feedforward neural networks propagate the inputs (the input layer) through a set of computational nodes arranged in layers to calculate the network outputs. The output layer is the final layer of the neural network and usually contains linear elements (Hecht Nielsen 1988). The layers between the input layer and the output layer are called hidden layers and usually contain nonlinear elements. This network topology is depicted graphically in Figure. 9. The various types of feedforward neural networks differ primarily in the nonlinear functions (the so-called activation functions) that are used in the hidden layer nodes and the training algorithms that are used to optimize the free parameters of the network (C. M. Bishop 2007).

In general, the connections shown in Figure. 9. need not be fully populated: some optimization strategies start with a large number of hidden nodes and "prune" the network by eliminating connections, and possibly nodes, as training progresses.

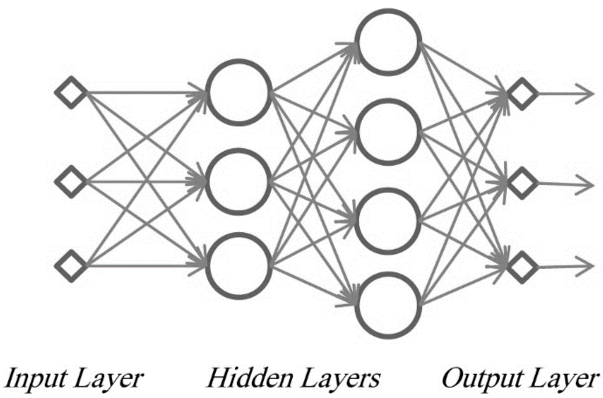


Figure. 9. The general structure of a multilayer feedforward neural network is shown, including forward connections between successive layers

### *Multilayer Perceptron Networks*

The perceptron is the basic structural element of feedforward multilayer perceptron networks. The inputs to a perceptron are weighted, summed over the n inputs, translated, and passed through an activation function. The perceptron is shown graphically in Figure. 8, and the transfer function can be written as follows (Hecht Nielsen 1988, S. Haykin 2008):

$$y = f\left(\sum_{i=1}^{n} w_i x_i + b\right)$$

where $x_i$ is the $i^{th}$ input, $w_i$ is the weight associated with the $i^{th}$ input, b is the bias, f (·) is the activation function of the perceptron, and y is the output.

The activation functions are generally chosen to be strictly increasing, smooth (continuous first derivative), and asymptotic. Perceptrons with sigmoidal (soft limit) activation functions are commonly used in the hidden layer(s), and the identity function is used in the output layer. The logistic function is defined as follow (C. M. Bishop 2007):

$$f(x) = \frac{1}{1 + e^{-x}}$$

However, a multilayer perceptron trained with the backpropagation algorithm may, in general, learn faster when the activation function is antisymmetric, that is, f (−x) = −f (x). The logistic function is not antisymmetric, but can be made antisymmetric by a simple scaling and shifting, resulting in the hyperbolic tangent function:

$$f(x) = \tanh x = \frac{e^x - e^{-x}}{e^x + e^{-x}}$$

These linear and hyperbolic tangent activation functions are shown in Figure. 10. The simple form of sigmoidal function and its derivative allows fast and accurate calculation of the gradients needed to optimize selection of the weights and biases and carry out second order error analysis (S. Haykin 2008).

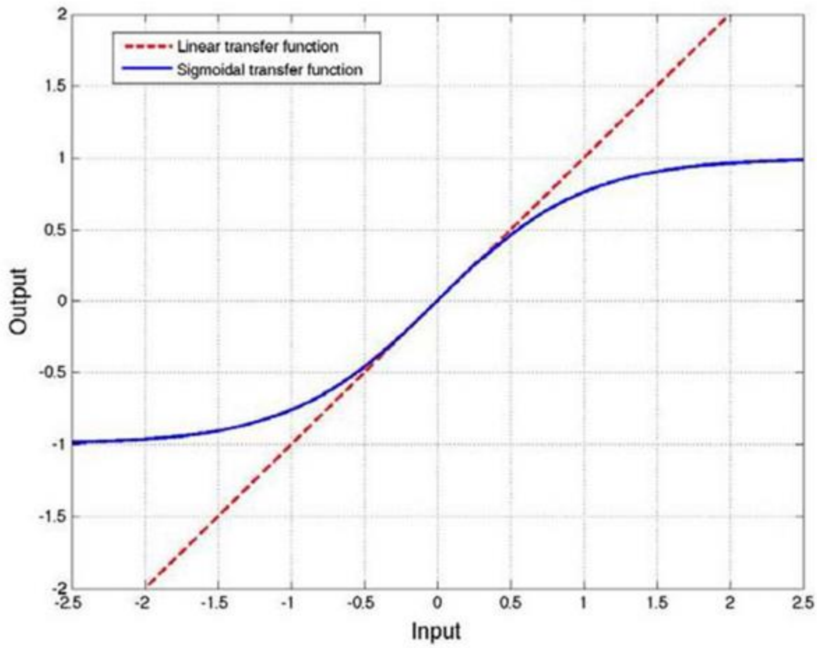


Figure. 10. Two common neural net transfer functions are shown: hyperbolic tangent (solid curve) and linear (dashed curve)

### *Feedforward Multilayer Perceptron Neural Networks*

Networks Perceptrons can be combined to form a multilayer network. In this type of network, individual perceptrons are arranged in layers, and the perceptrons in each layer all use the same transfer function. The inputs to the network are fed to every node of the first layer, and the outputs of each layer (except the output layer) are fed to every node of the next layer. An example of a two-layer network (that is, two hidden layer and one output layer) is shown in Figure. 9.

In Figure. 8, n is the number of inputs, $w_{ij}$ is the weight associated with the connection from the $i^{th}$ input to the $j^{th}$ node in the hidden layer, $b_i$ is the bias of the $i^{th}$ node, m is the number of nodes in the hidden layer, f (·) is the transfer function of the perceptrons in the hidden layer, with the weight between the $i^{th}$ node and the output node, c is the bias of the output node, g(·) is the transfer function of the output node, and y is the output. We can then relate the network output to the inputs as follows:

$$y = g\left(\sum_{j=1}^{m} u_i f\left(\sum_{i=1}^{n} w_{ij} x_i + \; b_j\right) + c\right)$$

### Radial Basis Function Networks

Multilayer perceptron networks, while powerful, often have complicated error surfaces and therefore higher likelihoods of suboptimal training and instability. Radial basis function networks use simple activation functions that tend to be localized. This simplicity and localization reduces the complexity of the error surfaces, but many nodes are needed to represent features that are active over large regions of the radial basis functions input space which are based on the distance metric.

Radial basis function is applicable to a wide range of problems in machine learning ranging from pattern recognition, function approximation, interpolation, and mixture modeling. Common radial basis functions (with width parameter σ) include (Hecht Nielsen 1988):

Multiguadric: $\Phi(r) = \sqrt{r^2 + \sigma^2}$

Inverse multiguadric: $\Phi(r) = 1/\sqrt{r^2 + \sigma^2}$

Gaussian: $\Phi(r) = e^{(-r^2/2\sigma^2)}$

and more sophisticated functions can be readily constructed by replacing the Euclidean distance metric given by the Mahalanobis distance metric:

$$r_m = \sqrt{(X - X_i)^T C_{XX}^{-1} (X - X_i)}$$

Most radial basis functions are quasi-orthogonal, that is, the product of two basis functions, whose centers are far away from each other with respect to their widths, is almost zero. If we collect the scalar basis functions $\varphi_i$ (each with a center $X_i$ and width $\sigma_i$) into a vector basis function Φ(X), we can estimate the target function as follows:

$$Y = f(X) = \mathbf{W}\Phi(X)$$

where each row of the weighting matrix **W** assigns a linear combination of the bias functions to an output. Given m basis functions and n dimensions in the output vector, the size of the weighting matrix **W** is n × m. The training algorithm determines **W**, $X_i$ , and $\sigma_i$ by minimizing a cost function, usually a form of sum-squared error of the network outputs relative to the targets:

$$C(.) = \|Y - T\|^2$$

## Supervised and Unsupervised Learning

Learning algorithms extract mathematical features and characteristics from a set of training data, and the "learning" is often enabled either by some kind of reinforcement or competition. Learning can be either supervised or unsupervised. Supervised learning uses pairs of data arranged as inputs and targets. Each input has associated with it a target, and the learning algorithm infers the relationship between the inputs and the targets as the training proceeds. Multilayer perceptron networks and support vector machines are examples of supervised learning. Unsupervised learning methods do not require input target pairs; the algorithm itself decides what target is best for a given input and organizes accordingly. Pulsed coupled neural networks is an example of unsupervised learning (C. M. Bishop 2007, S. Haykin 2008). Semi-supervised approaches are also possible, where both types of learning are used within the same algorithm.

## Network Training

The process of deriving the network weights and biases to best fit the ensemble of input and target vectors is called training. The components of network training involve assembly of the data set, selection of network topology, network initialization, and optimization of weights and biases (including regularization, if necessary). Once the network is trained, it is imperative that performance evaluation and error analysis techniques are used to ensure the network generalizes well (that is, produces a reasonable output for an unseen input) (C. M. Bishop 2007).

### Initialization

Numerical optimization methods are often initialized to appropriate starting values from which optimization proceeds. Initialization for neural network training is especially important because the error surfaces are often complex. The general objective when initializing the weight and bias values is to maximally span the search space and exercise all of the available information in the input and target data. This initialization is typically carried out by assigning random values to the weights and biases. Substantial improvements to training time and resistance to local minima can be achieved by selecting the initial weight and bias values so that the active regions of all node transfer functions are utilized when training begins (C. M. Bishop 2007).

### Backpropagation Learning

After initialization, the weights and biases are tuned to best represent the relationships present in the training set. The sigmoidal activation functions are continuous and differentiable and are thus amenable to optimization algorithms based on gradient descent. Backpropagation learning is one such algorithm. The simplest implementation of backpropagation updates the network weights and biases in the direction in which the cost function decreases most rapidly, the negative of the gradient. The backpropagation algorithm calculates updates efficiently by propagating the errors back through the network (thus the name “backpropagation”) (C. M. Bishop 2007).

In this research, I focus on feedforward multilayer perceptron (FFMLP), Redial Bases Function (RBF) and Pulsed Coupled Neural Networks (PCNN) neural networks due to their simplicity, flexibility, and ease of use.

## Pulse-Coupled Neural Networks

In the late 1980s, Eckhorn et al. discovered that the midbrain in an oscillating way created binary images that could extract different features from the visual impression when they had studied the cat visual cortex (Eckhorn 1989, Eckhorn 1990). Based on these binary images the actual image is created in the cat brain. Due to this discovery they developed a neural network, called Eckhorn's model, to simulate this behavior. In the early 1990s, Rybak et al. also found the similar neural behavior based on the study of the visual cortex of the guinea pig and developed a neural network, called Rybak's model (Rybak, Shevtsova et al. 1991, Rybak, Shevtsova et al. 1992). Because Eckhorn's model and Rybak' model provided a simple, effective way for studying synchronous pulse dynamics in networks, they are recognized as being very potential in image processing (Johnson and Padgett 1999, Johnson, Padgett et al. 1999, Ranganath and Kuntimad 1999).

The PCNN is a single layer, two-dimensional, laterally connected network of integrate-and-fire neurons, with a 1:1 correspondence between the image pixels and network neurons. This is a neural network without any training needed. The output images at different iterations typically represent some segments or edges information of the input image. As a new generation of neural network, the PCNN is good at digital image processing and applied in other fields. More contents will be introduced in the latter sections.

During the last decade, the PCNN has undergone rapid development. Johnson and Padgett (Johnson and Padgett 1999, Johnson, Padgett et al. 1999) published a comprehensive survey of the PCNN in 1999. Considering that most of methods published before 1999 are summarized in the literature (Johnson and Padgett

1999, Johnson, Padgett et al. 1999, Waldemark, Millberg et al. 2000), they are no longer given emphasis in the related literature.

### *Description of PCNN models*

The PCNN neuron's structure is shown in Figure. 11. The neuron consists of an input part, linking part and a pulse generator. The neuron receives the input signals from feeding and linking inputs.

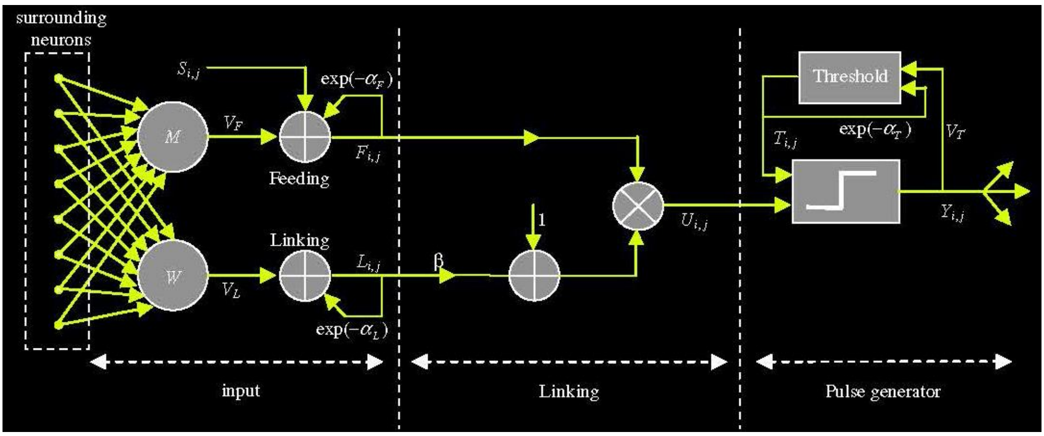


Figure. 11. PCNN's neuron model (Johnson and Padgett 1999)

Feeding input is the primary input from the neuron's receptive area. The neuron receptive area consists of the neighboring pixels of corresponding pixel in the input image. Linking input is the secondary input of lateral connections with neighboring neurons. The difference between these inputs is that the feeding connections have a slower characteristic response time constant than the linking connections. The standard PCNN model is described as iteration by the following equations (Johnson and Ritter 1993, Johnson 1994, Ranganath and Kuntimad 1999):

$$F_{i,j}[n] = e^{-\alpha_F} F_{i,j}[n-1] + V_F \sum_{k,l} w_{i,j,k,l} Y_{i,j}[n-1] + S_{i,j}$$

$$L_{i,j}[n] = e^{-\alpha_L} L_{i,j}[n-1] + V_L \sum_{k,l} m_{i,j,k,l} Y_{i,j}[n-1]$$

$$U_{i,j}[n] = F_{i,j}[n](1 + \beta L_{i,j}[n])$$

$$Y_{i,j}[n] = \begin{cases} 1 & U_{i,j}[n] > T_{i,j}[n] \\ 0 & otherwise \end{cases}$$

$$T_{i,j}[n] = e^{-\alpha_T} T_{i,j}[n-1] + V_T Y_{i,j}[n]$$

In these equations, $S_{i,j}$ is the input stimulus such as the normalized gray level of image pixels in (i,j )position, $F_{i,j}[n]$ is the feedback input of the neuron in (I,j), and $L_{i,j}[n]$ is the linking item. $U_{i,j}[n]$ is the internal activity of neuron, and $T_{i,j}[n]$ is the dynamic threshold. $Y_{i,j}[n]$ stands for the pulse output of neuron and it gets either the binary value 0 or 1. The input stimulus (the pixel intensity) is received by the feeding element and the internal activation element combines the feeding element with the linking element.

The value of internal activation element is compared with a dynamic threshold that gradually decreases at different iterations. The internal activation element accumulates the signals until it surpasses the dynamic threshold and then fires the output element and the dynamic threshold increases simultaneously strongly. The output of the neuron is then iteratively fed back to the element with a delay of one iteration.

The inter-connections **M** and **W** are the constant synaptic weight matrices for the feeding and the linking inputs, respectively, which are dependent on the distance between neurons. Generally, **M** and **W** (normally **W=M** refer to the Gaussian weight functions with the distance. **β** is the linking coefficient. $\alpha_F$, $\alpha_L$ and $\alpha_T$ are the attenuation time constants of $F_{i,j}[n]$, $L_{i,j}$ [n] and $T_{i,j}$ [n], respectively. $V_F$; $V_L$, and $V_T$ denote the inherent voltage potential of $F_{i,j}[n]$, $L_{i,j}$ [n] and $T_{i,j}$ [n], respectively.

For the feeding channel, $\alpha_F$ determines the rate of decay of the feeding channel. Larger $\alpha_F$ causes faster decay of the feeding channel. $V_F$ can enlarge or reduce the influence from surrounding neurons. Matrix **W** refers to the mode of inter-connection among neurons in the feeding receptive field. Generally, the size of **W** denotes the size of the feeding receptive field. The value of matrix element $w_{ijkl}$ determines the synaptic weight strength. In most cases, this channel is simplified via $\alpha_F = 0$ and $V_F = 0$.

Different from the feeding channel, the link channel usually keep itself as it is. The link channel also has three parameters ($\alpha_L$; $V_L$, and M) that have the same function to the parameters ($\alpha_F$; $V_F$, and W, respectively. It is noteworthy that the mode of inter-connection should be designed carefully according to the task of data processing (e .g. image de-noising), for it has a great effect on the output of PCNN. Usually, the inter-connection employs the Gaussian weight functions with the distance.

The linking coefficient β is an important parameter, because it can vary the weighting of the linking channel in the internal activity. Hence, its value is usually depended on different demands. For example, if much influence from the linking channel is expected, β should be given larger value. All neurons often have the same value of β. It is not absolute. Each neuron can have its own value of β.

For the pulse generator, $\alpha_T$ indicates the rate of decay of the threshold in the iterative process. Because it directly decides the firing time of neuron, $\alpha_T$ is a significant parameter. Smaller $\alpha_T$ can make the PCNN work in a meticulous way but it will take much time to finish the processing. On the contrary, larger $\alpha_T$ can decrease more running time of PCNN. $V_T$ decides the threshold value of fired neuron. If expecting that neuron just fires one time, you can give $\alpha_T$ a huge value.

Image processing is a main application of the PCNN, and most of the papers which are focus on this field can be divided into: image segmentation, image denoising, object and edge detection, feature extraction and pattern recognition, image enhancement, image fusion, and other applications. The three subsections (image denoising, image enhancement, image fusion) refer to applications in image preprocessing. It shows that PCNN has excellent preprocessing capabilities. Other subsections describe other kinds of applications in image processing.

# ANNs for analysis of remotely sensed data

Remote sensing is an efficient tool for monitoring the Earth at low cost and in a short time. Nevertheless, when a strict accuracy assessment is made (e.g. based on an unbiased sample and independent classification of verification sites), the results obtained from remote sensing are often disappointing (Zhu, Yang et al. 2000), which makes any improvement in the methods of analysis crucial. Since the beginning of the 1990s, artificial neural networks (ANNs), also known as neural networks, have been applied to the analysis of remote sensing images with promising results (Atkinson and Tatnall 1997). Many authors have reported considerable advantages of ANNs over conventional methods. In brief, the rapid uptake of neural approaches in remote sensing is due mainly to their widely demonstrated ability to:

- learn complex patterns, taking into account any nonlinear complex relationship between the explicative and the dependent variables (Lek and Guegan 1999) which include almost all the problems in remote sensing filed,
- generalize in noisy environments, which makes ANNs robust solutions in the presence of incomplete or imprecise data (Foody 2004),

- incorporate a priori knowledge and realistic physical constraints into the analysis (Foody 1995) and,
- incorporate different types of data into the analysis because of the absence of assumptions about the data set used (e.g. normally distributed data) (Civco 1993, Benediktsson and Sveinsson 1997).

This last characteristic allows the incorporation of data from different sensors and ancillary data such as elevation, slope, texture or categorical data such as thematic maps (Foody, Boyd et al. 2003, Foody and Cutler 2006, C. M. Bishop 2007), thus facilitating synergistic studies (Benediktsson, Swain et al. 1990, Benediktsson, Swain et al. 1993, Benediktsson and Sveinsson 1997). An additional advantage of the ANN approach is that ANNs perform supervised classification using less training data than the other supervised machine learning algorithms because the rules of recognition of a category are based on the characteristics not only of the training data of this particular category class but also of the other classes (Paola and Schowengerdt 1995).

Moreover, ANNs allow fuzzy classifications considering the activation values as fuzzy membership measures of belonging to a class (Civco 1993, Arora and Foody 1997, Carpenter, Gopal et al. 1999, Mas 2004, Foody and Cutler 2006). These fuzzy values can also be interpreted in terms of classification certainty (Gong, Pu et al. 2001).

As a result of these qualities, ANNs have been reported to perform more accurately than other techniques such as statistical classifiers, particularly when the feature space is complex and the source data have different statistical distributions (Benediktsson, Swain et al. 1990, Schalkoff 1997).

Comparative studies have shown that ANNs may be used to classify remotely sensed data more accurately than maximum likelihood (Civco 1993, Paola and Schowengerdt 1995, Frizzelle and Moody 2001, Kavzoglu and Mather 2003, Murthy, Raju et al. 2003, Seto and Liu 2003, Liu, Gopal et al. 2004, Chitroub 2005) or others techniques such as regressions or tree approaches (Borak and Strahler 1999, Joshi, De Leeuw et al. 2006).

However, comparative studies between a novel and a conventional method tend to be biased because authors proposing a new method are usually more familiar with their own new algorithm than the one used for comparison, and articles that present a new method that performs better than conventional ones are more likely to be published (Carpenter, Gopal et al. 1999, Michelson, Liljeberg et al. 2000, Del Frate and Salvatori 2004, Pu and Gong 2004, Shupe and Marsh 2004, Del Frate, Latini et al. 2010, Avezzano, Velotto et al. 2011, Avezzano, Del Frate et al. 2012).

# Chapter II

# Passive Oil Spill Remote Sensing expert systems

Case study: Oil Spill Gulf of Mexico 2010

**Taravat, A.** and F. DelFrate (2012). "*Development of band ratioing algorithms and neural networks to detection of oil spills using Landsat ETM+ data*." ***EURASIP Journal on Advances in Signal Processing*** 107.

**DOI**: 10.1186/1687-6180-2012-107

## Optical properties of oil spill

The exploitation of optical satellite images allows for large areas monitoring and remote zones control, providing more frequent information if compared to the use of SAR images only. Moreover, the possibility of detecting oil spills by optical satellite sensors has been demonstrated (Otremba and Piskozub 2001, Hu, Müller-Karger et al. 2003, Hu, Li et al. 2009).

It is the optical properties and chemistry (OH, CN, and CH bonds) of oil that makes it detectable by remote sensing techniques in marine environment (Barbara E. Ornitz 2002).

Due to the chemical structures of HC, absorption features appear in the near infrared (NIR) region of the electromagnetic spectrum which extends from the upper wavelength end of the visible region (about 770 nm) to 3000 nm. Those are due to overtones or combinations of fundamental stretching vibrational bands that occur in the mid-infrared region (Skoog and LEARY 1991). The bonds involved are usually C-H (e.g. aromatics), O-H (e.g. phenols), and N-H (e.g. amines). Among those, aromatics group is the common form of HC pollution in coastal marine environments.

The absorption properties of crude oils are determined by the concentration and chemical identity of the constituent aromatic hydrocarbons (Figure. 12). The aromatic fraction is known to vary from oil to oil and leads to considerable differences in absorption spectra. Light absorption depends on the size of chromophores, heteroatom content and chelation with transition metals. Typical oil spectra show strong absorption at short wavelengths, with an exponential decay towards longer wavelengths. The position of this absorption edge ranges from UV or violet for the lightest oils to far red or even NIR for the heaviest crudes (Mullins, S. et al. 1992, Mullins and Y. 1992, Wang and O.C. 1994).

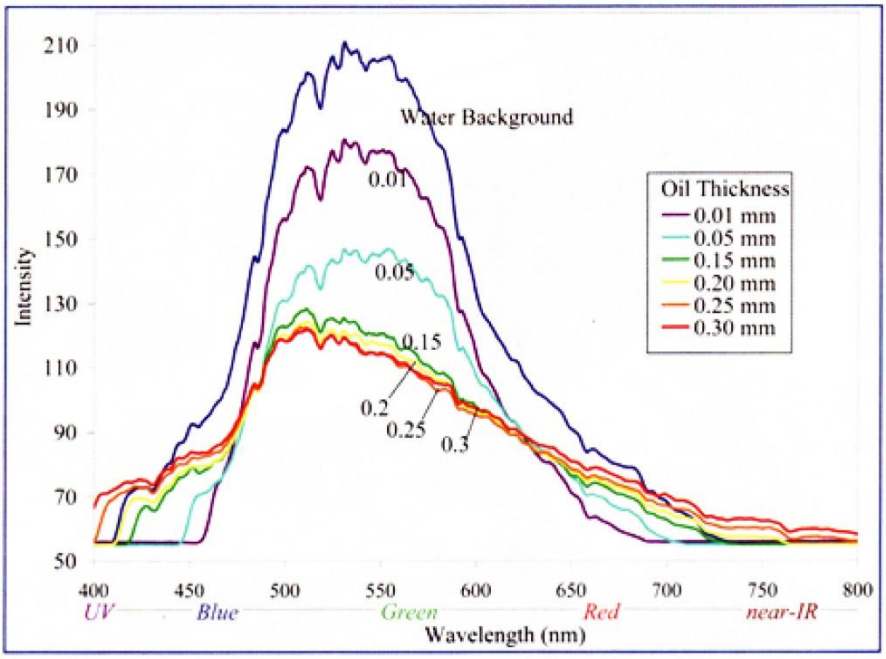


Figure. 12. Reflectance spectra of progressively crude oil films over deep-water background. Note the changes in the green-red parts of the spectrum with increasing oil thickness (Svejkovsky, Muskat et al. 2009)

Refined oils have been subject to fractionation, and as a result will have a population of chromophores which is truncated at either the large chromophore end (light refined oils) or at the small chromophore end (heavy refined oils). The wavelength dependence of their absorption coefficients will be correspondingly anomalous. The absorption coefficient of light refined oils decreases abruptly towards visible wavebands, while heavy refined oils have lower absorption in the UV, but much larger decay widths extending well into the NIR.

Un-emulsified neat oil is a relatively uniform mixture of compounds where discontinuities in density and refractive index are on a scale which is small compared to the wavelength of visible light. Thus scattering is also likely to be small, and of a magnitude and wavelength-dependence close to that of pure sea-water. Hence absorption dominates, even for light refined oils. From an optical perspective, the effect of an oil layer on water can be described in detail by two main processes; first, the specular reflection of light off the surface of the oil layer, and more importantly, and second, the absorption of up-welling light from the water column by the overlying oil layer (Otremba and Piskozub 2001, Wettle, Daniel et al. 2009).

The refractive index of oil, is higher than that of sea-water ($n_{sw} \approx 1.34$) at visible and NIR wavelengths (Wettle, Daniel et al. 2009). There is considerable variation between oil types, with heavy oils usually having a higher refractive index. Typically, crude oils lie in the range 1.57-1.67 in the UV and 1.48-1.52 in the visible part of the spectrum (Osadchy, Shifrin et al. 1994). The most obvious effect of the difference in refractive index is seen in specular reflection at the air-sea interface for clean and oil-covered surfaces. The relative refractive index also influences scattering of light by dispersed oil micelles, or by water droplets within emulsified oil.

The contrast of sea areas polluted by oil depends on the form of the oil substance. It is negative, positive, or zero with film, and only positive with suspensions (Otremba and Piskozub 2001). In the visible region of the electromagnetic spectrum, oil has a higher surface reflectance than water (Svejkovsky, Muskat et al. 2009). So, reliable identification of oil spill by remote sensing is only possible if the difference in measured radiance between an oil covered and a clean surface is greater than the background variability (Figure. 13).

### *Water in oil emulsion*

In emulsions, scattering of light by water droplets, and absorption and fluorescence by the oil matrix all influence upwelling radiance. Light absorption in emulsions depends on the absorption coefficients of both the oil and the entrained sea-water, each weighted by their respective concentrations.

For most crude and heavy refined oils, the oil absorption coefficient will be many orders of magnitude greater than that of water, and will dominate, especially at shorter wavelengths - even for emulsions with  80% water.

The main effect of the water droplets will be through backscattering of incident light. As soon as spilt oil begins to take up water, scattering increases. As a result the emulsion will often appear brighter than neat surface oil. Possible exceptions to this are highly absorbing dark crudes and heavy fuel oils where absorption dominates scattering even at red to near-infrared wavelengths (Fingas 2001).

Lighter oils with lower absorption coefficients may appear golden, orange, red, brown or grey when emulsified - the exact color depends on the position of the oil's absorption and its decay width. For very light oils (usually only light refined oils), this means that emulsions will appear white or cream (Fingas 2001).

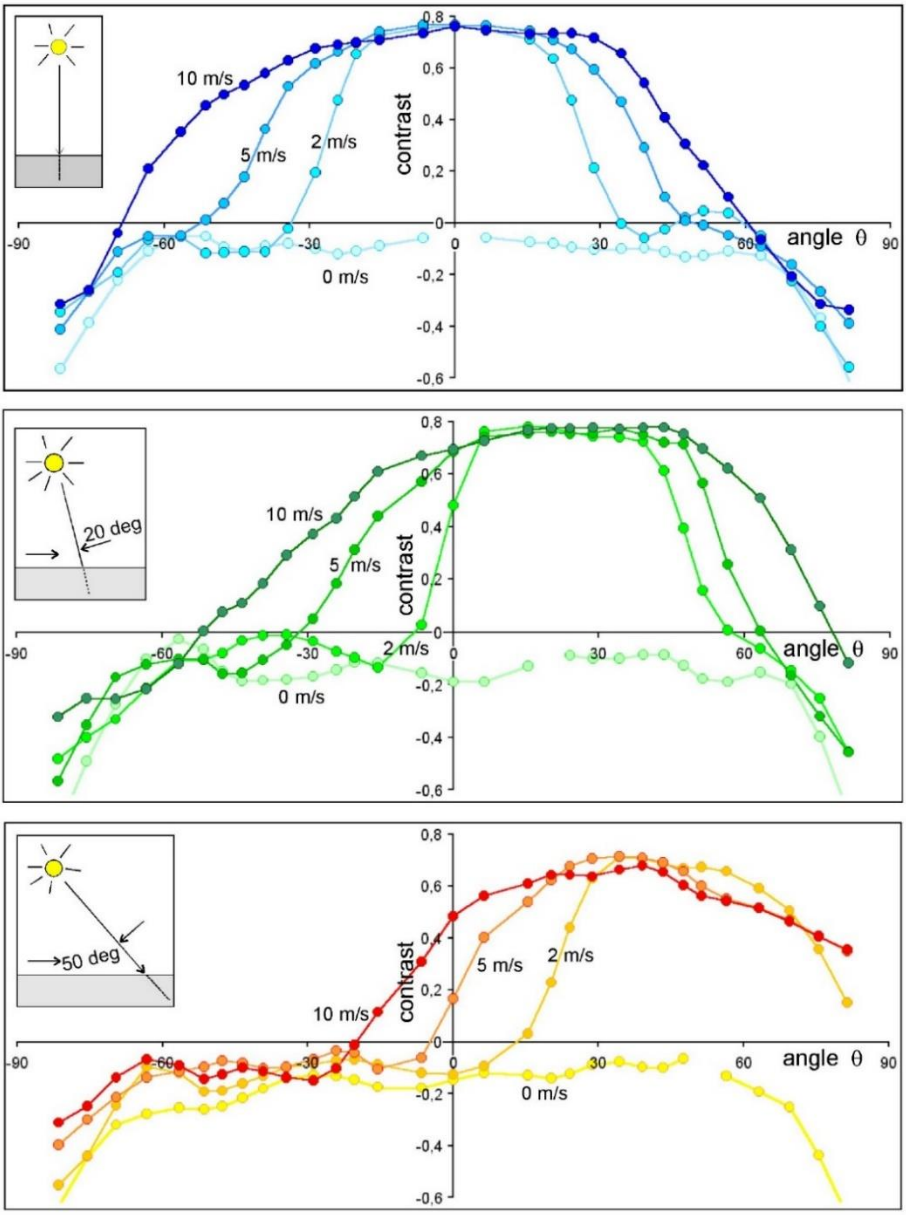


Figure. 13. Contrast of an oil film on a sea surface at various light incidence angles (0º upper, 20º middle, 50º lower) and at various wind speeds (0 m/s,2 m/s,5 m/s,10 m/s) (Otremba and Piskozub 2001)

# Experimental results

In addition to SAR, there are other spaceborne remote sensing devices that have some potential for oil spill monitoring. (Friedman, Pichel et al. 2002) compare a RADARSAT-1 SAR image with a corresponding Sea-viewing Wide Field-of-view Sensor (SeaWiFS, visible sensor) image. SeaWiFS measures high levels of chlorophyll for areas with algal bloom, while the SAR images have low backscatter levels in these regions.

It is concluded that multiple data sets can be used to discriminate between, for example, algal blooms and man-made slicks. (Shepherd 2004) point out that additional information (in addition to SAR) about algal bloom is desirable, particularly in the Baltic Sea. This could be taken from optical imagery, from alga maps or other related information.

A drawback of the SeaWiFS sensor is its coarse spatial resolution of ~1 km. (Hu, Müller-Karger et al. 2003) demonstrate the possibility of oil spill monitoring by the Moderate-Resolution Imaging Spectroradiometer (MODIS) instrument with the spatial resolution of ~500 m, carried onboard the NASA satellites Terra and Aqua, by an example from Lake Maracaibo, Venezuela. Optical remote sensing instruments for oil spill response on airborne and satellite platforms, including acronym definitions are described in Table. 1.

Expert systems can augment the limited availability of experienced observers by providing rapid image analysis for oil spill detection. An effective approach uses a neural network trained on a range of images of oil of different types, thicknesses, oil-free water, sunglint, and typical sea surface features (However, to the best of the authors' knowledge, automatic oil spill detection by neural networks in optical data is not reported in the literature). A fuzzy logic classification algorithm produces a geo-referenced map of oil spill classes (Svejkovsky, Muskat et al. 2009, Leifer, Lehr et al. 2012). Note that significant sunglint, or surface layer reflection inherently reduces oil slick detection of any thickness.

| Instrument (satellite) | Bands (# bands) | Band range (nm) | Resolution (km) | Swath (km) | Revisit[A] (days) | Rapid response |
|---|---|---|---|---|---|---|
| LandSat 5, LandSat 7 | Vis, NIR, TIR (8 bands) | 450–12,500 nm | 0.030–0.120 | 185 | 16 | No |
| LandSat TM | Vis, NIR, TIR (7 bands) | 450–12,500 | 0.03, 0.120 | 185 | 1–3/16 | No |
| MODIS (Terra, Aqua) | Vis, MIR, TIR (36 bands) | 405–14,385 | 0.25, 0.5, 1.0 | 2330 | 1–2 | Yes |
| ASTER (Terra) | VNIR, NIR, TIR (14 bands) | 520–11,650 | 0.015/0.03/0.09 | 60 | 4–16 | No |
| MISR (Terra) | Vis, NIR (4 bands) | 446.4–866.4 | 0.275–1.1 | 360 | 2–9 | No |
| MERIS (ENVISAT) | Vis–NIR (15 bands) | 412.5–900 | $2.36 \times 0.30$–$1.04 \times 1.2$ | 1150 | 3 | |
| HICO | Vis–NIR (90 bands) | 390–1040 | 0.95 | 43 | – | No |
| Quickbird | Vis–NIR (4 bands) | 450–900 | .00061/0.0024 | 16.4 | 1–3.5 | Yes |
| AVHRR/3 (POES) | Vis, MIR, TIR (6 bands) | 580–12,500 | 1.09 | 2440 | 0.5 | No |

Table. 1. Summary of oil spill remote sensing relevant Optical spaceborne sensors

I observe that in the case of optical data, where a spectral signature for each pixel is available, a pixel-based algorithm can be designed. This is not possible with SAR where the detection is usually implemented starting from a single-band acquisition. This means that a preliminary image segmentation is necessary to extract the dark spot and an object classification to distinguish between actual oil spill and look-alikes is then applied.

In this phase of my research, I have tried to perform ratio operations to enhance the oil spots, extracting the features by an MLP neural network, and demonstrate the potential of Landsat ETM+ data in oil spill monitoring in the Gulf of Mexico based on the optical properties of oil slicks detected by neural network.

## Material and method

Landsat ETM+ images for the area from 29º N to 27º N and 87º W to 90º W for Gulf of Mexico, acquired in $1^{st}$, $10^{th}$, and $17^{th}$ May 2010 were used to study the previously known oil spills (USGS 2010). Landsat ETM+ has eight bands which may be combined in various ways by assigning one band to each of the three visible channels: red, green, and blue, to create a false color image.

Sub-images containing oil spills were extracted using the Area of Interest tool of ENVI (Environment for Visualizing Images) software to spare disk space and to make classification and image interpretation more expedient and focused. The data were then projected in Geo (lat/long) projection and WGS84 datum. Further the image was exported into *.TIFF format for further analysis (slick detection, feature extraction, spectral enhancement, and filtering).

The stripes in Landsat ETM+ data (caused by the Scan Line Corrector in the ETM+ instrument failed On May 31, 2003) have been removed by a developed model which identifies stripe positions based on edge-detection and applies line-tracing algorithms.

Pixels not affected by striping are used to construct spline functions describing spatial gray level distributions of an image. Detected stripes are corrected by replacing the pixels with more reasonable gray values computed from constructed spline functions.

To produce optimal contrast and variation for color composition of those individual bands, ratio operations were applied to the images with various band combinations. For the classification test, MLPs have been considered, which have been found to have the best suited topology for pixel level classifications (C. M. Bishop 2007).

The net was trained using the back propagation algorithm, which uses a gradient search technique and iteratively adjusts the weight coefficients in the network to minimize an error function equal to the mean square difference between the desired and the actual net output (C. M. Bishop 2007).

## Result and discussion

The earlier studies carried out by (Hu, Müller-Karger et al. 2003) reported that the shorter wavelengths were more sensitive to optical signature of oil; therefore, Landsat ETM+ data in spectral bands B1 (480 nm), B2 (560 nm), B3 (660 nm), B4 (825 nm) have been used in this study (Hu, Müller-Karger et al. 2003).

As it is already mentioned, the refractive index of oil is greater than that of sea water, but there are possibilities of masking the data, while performing atmospheric corrections (Srivastava and Singh 2010). Therefore, in order to identify the oil spill area, just geometrically corrected data have been used.

To identify the spectral signature of oil spill, a spectral profile along transect (*A*) was plotted. The visual interpretation in individual bands did not produce significant signature of oil (Figure. 14). In order to identify the specific signatures of oil spill by enhancing the contrast, band ratio operations were performed. The ratios were computed using 65 different combinations of bands.

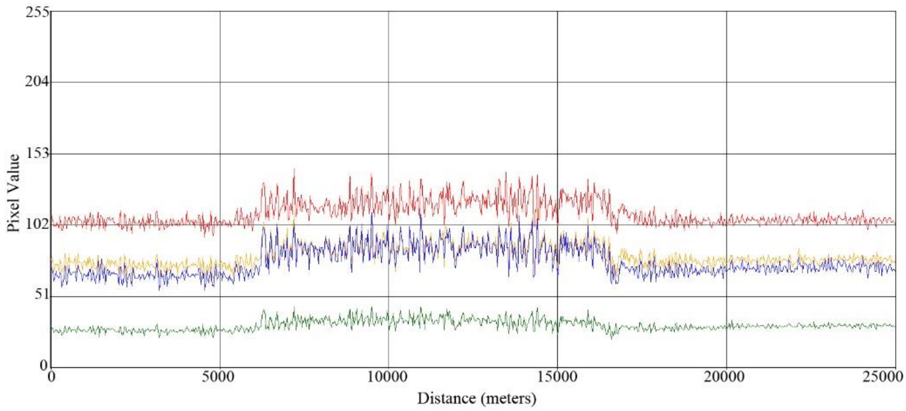


Figure. 14. Profile along transect A (1st May 2010, Original Image) for bands B1 (480 nm), B2 (560 nm), B3 (660 nm), B4 (825 nm).

To determine which combination showed the best contrast between the surface slick and surrounding clear ocean water, I extracted data along several transect lines for each band combination (Hu, Li et al. 2009).

The ratio combinations that showed excellent contrast (about -0.2, defined as $(R_s- R_c)/R_c$ where "$R_s$" and "$R_c$" stand for slick luminance and clear water luminance, whereas the contrast of the original bands are about 0.07) and the most significant for retrieving oil spill are given below:

RS1=(B4/B2)/B1

RS2=(B3/B2)/B1

RS3=(B3-B2)/B1

These combinations can be interpreted based on spectral signature of oil and water background in landsat ETM+. Oil and water background show steadily increasing reflectance spectrum between wavelength 475-675 nm, while they have different level of absorption in 675-800 nm, thus, information of oil spill could be extracted by band ratio of B4/B2 and B3/B2 (Svejkovsky, Muskat et al. 2009). There is a decrease in water background reflection from 550-750 nm; so to get some information on background the difference of bands 3 and 2 can be applied. Additionally, the difference between bands 3 and 2 is useful to visualize the data in RGB format.

The shorter wavelength at blue (B1) is normally found to be contaminated with the signatures of biogenic materials. Therefore, for removing biogenic materials effects, the results were normalized with respect to 480 nm (Srivastava and Singh 2010).

Color-composite images can be created by assigning RS1, RS2, and RS3 values, computed from the Landsat ETM+ data into red, green, and blue channels, respectively. The algorithm developed for oil spill was applied for the data of Gulf of Mexico on 1$^{st}$, 10$^{th}$, and 17$^{th}$ May 2010. Figure 15a presents the ratio image of Gulf of Mexico at May 1$^{st}$, 2010. The oil spill signatures were very well identified along transect A (Figure. 16).

When thick oil spots are present in clear, deep ocean water, strong yellow and orange tones in the color-composite image are indicative of areas containing them (Figure. 15a).

These tones result from the relatively higher values of RS1 and RS2 and relatively lower values for RS3 for oil spot as compared to clear, deep ocean water (Figure. 16). Blue and purple tones indicate the absence of oil or insufficient quantity or thickness to cause spectral differences associated with oil in spectral bands.

Figure. 15. Band ratioing and classification results. (a) Color composite of band ratioing for Landsat ETM+ data collected May 1st, 2010, in the Gulf of Mexico. (b) NN classification result of image (a). (c) Result of thresholding method applied on image (a). (Next Page Figure' caption)

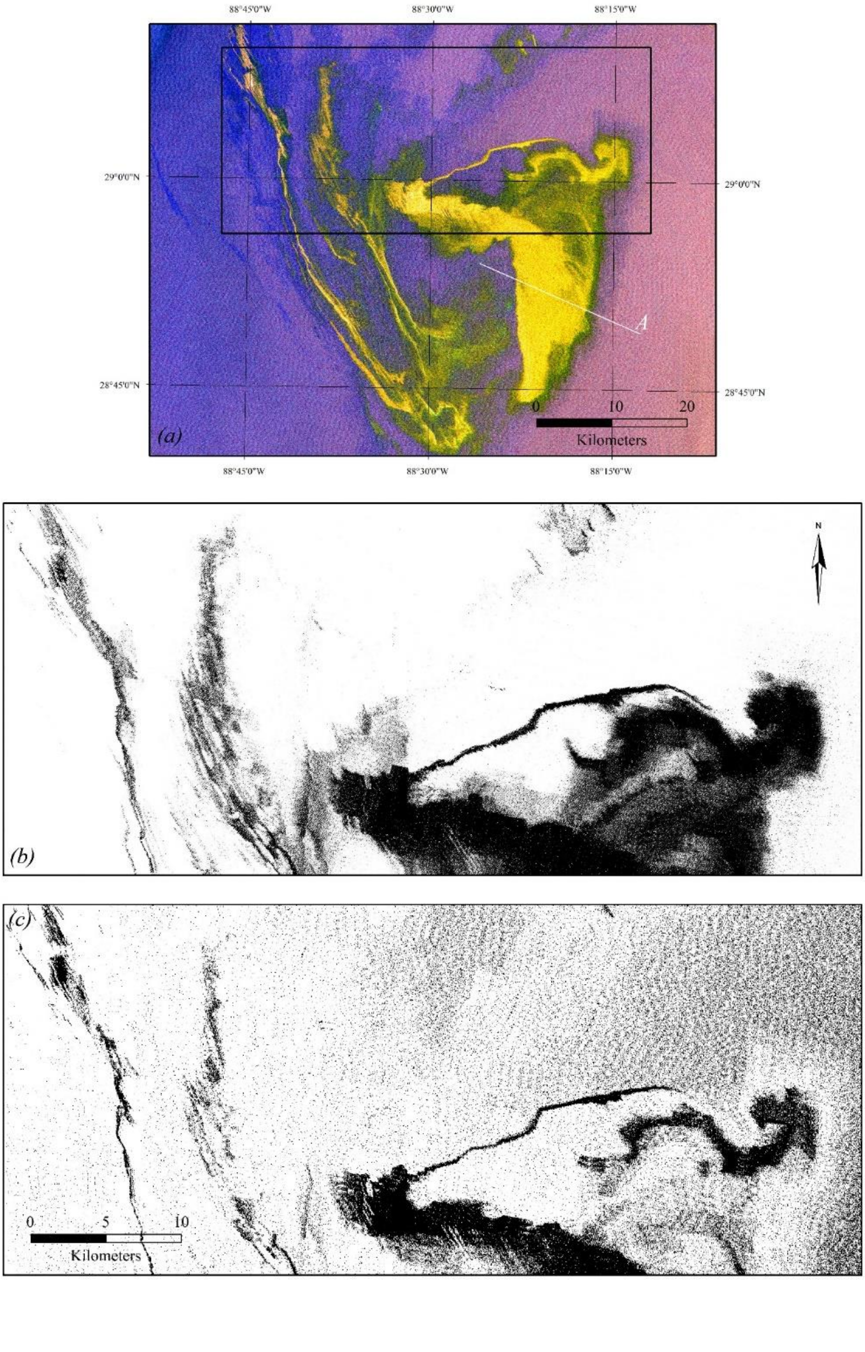
88°45'0"W
88°30'0"W
88°15'0"W
29°0'0"N
28°45'0"N
A
0
10
20
Kilometers
(a)
N
(b)
(c)
0
5
10
Kilometers

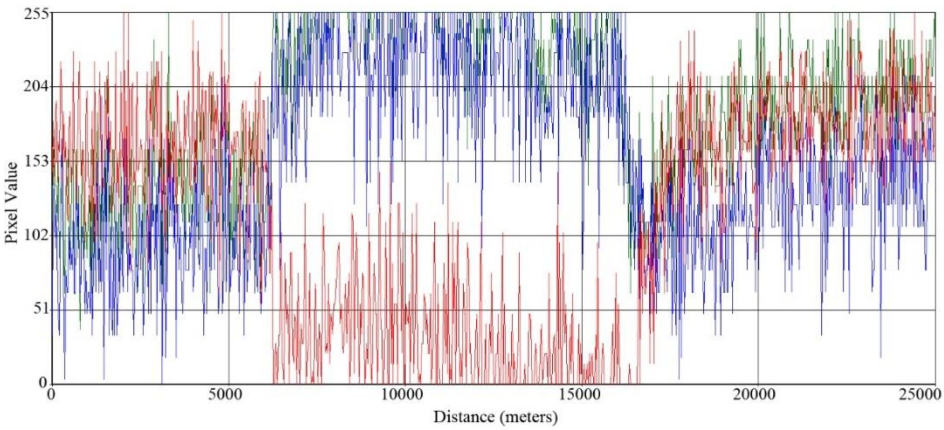


Figure. 16. Profile along transect A ($1^{st}$ May 2010, Image output of band rationing operation).

Once the best ratios to discriminate between the pixels contain oil and clear water have been determined, an MLP algorithm for pixel classification has been designed. The result has been compared with the result of Multiband thresholding algorithm which is the combined result of AND operation for thresholded RS1 and RS3 bands.

Several attempts have been made to properly select the number of units to be considered in the hidden layers. The pixels for train/test the net are 80,152 pixels which have been extracted from one image ($10^{th}$ May 2010, Gulf of Mexico) (Figure. 17). The training sets contain 60% and the test sets contain 40% of all pixels which are not belonging to the training set.

Pixel selection for train/test set has been done randomly and repeated six times; so the presented results of root mean square error (RMSE) errors are the average of these repetitions for each topology (Figure. 18). The topology 3-4-2 has been finally chosen for its good performance in terms of classification accuracy, RMSE, and training time.

The number of about 10,000 training cycles was sufficient to get the network learned. The input of the net consists of RS1, RS2, and RS3 bands and the output providing classified pixels in terms of oil spill or others and one MLP NNs has been used for classifying all images.

Figure. 17. (*Next Page Figure' caption*) Band ratioing and classification results. (a) Sub-images of color composite of band ratioing for Landsat ETM+ data collected May 17th, 2010, in the Gulf of Mexico. (b) Sub-images of color composite of band ratioing for Landsat ETM+ data collected May 10th, 2010, in the Gulf of Mexico, used for training the NN. (c) NN classification result of image (a). (d) NN classification result of image (b).

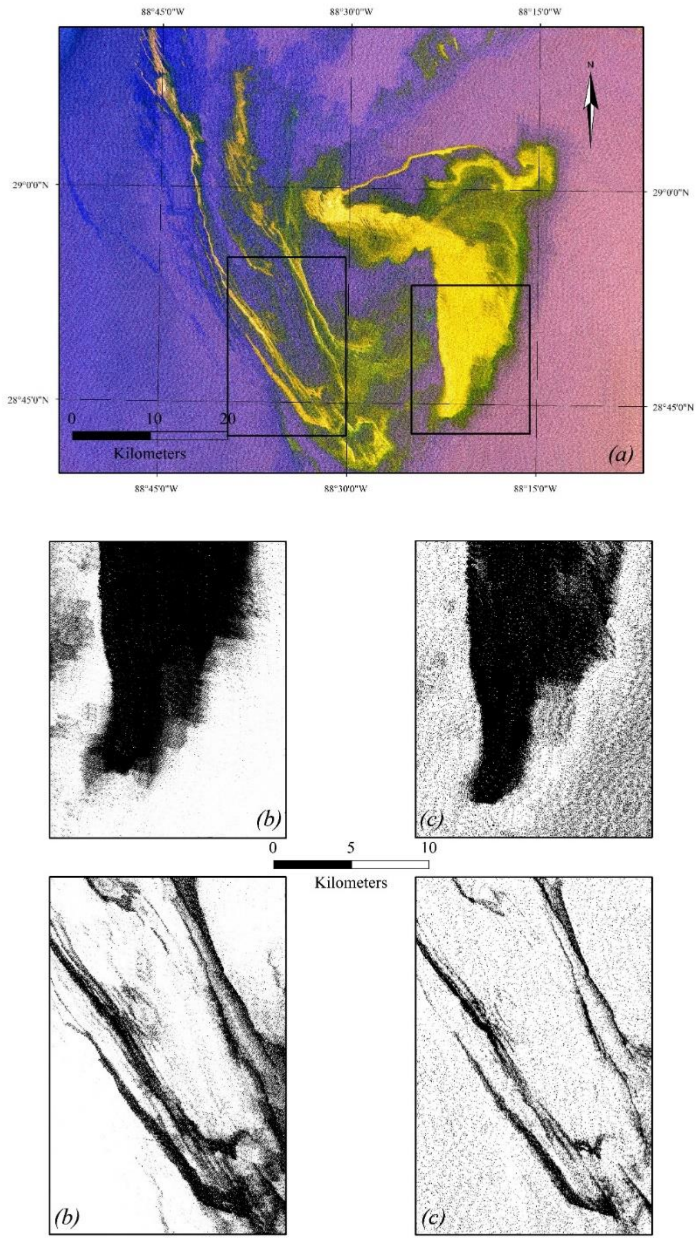
88°45'0"W
88°30'0"W
88°15'0"W
N
29°0'0"N
29°0'0"N
28°45'0"N
28°45'0"N
0
10
20
Kilometers
(a)
88°45'0"W
88°30'0"W
88°15'0"W
(b)
(c)
0
5
10
Kilometers
(b)
(c)

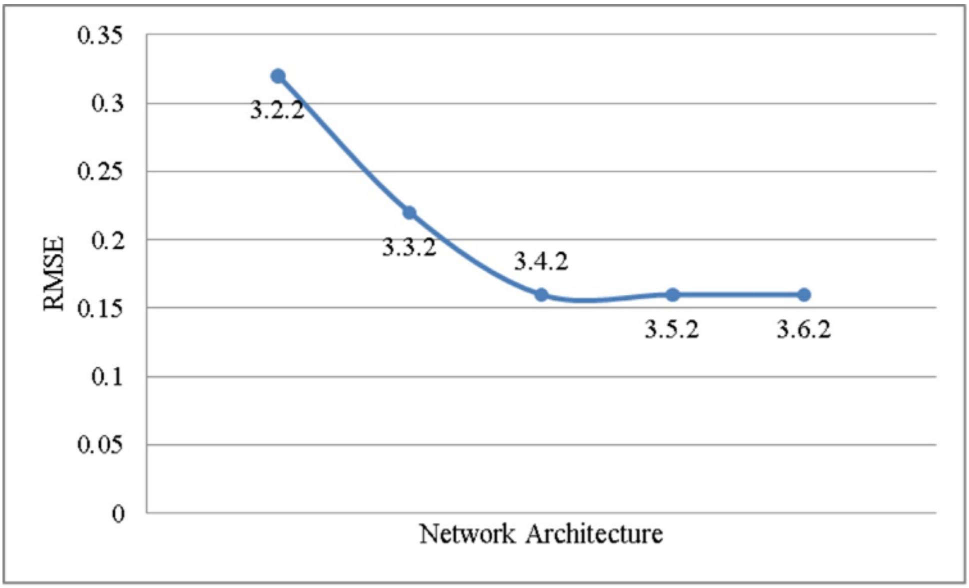


Figure. 18. RMSE errors for different NN topologies

Accuracy assessment has been carried out considering the other two images (1st May 2010, 17th May 2010). For both of them 5,000 pixels have randomly been selected and then labeling made by visual interpretation.

As it has been shown in Table. 2, the overall rate of the accurately classified pixels in image collected at 1st May 2010 is 97%, whereas the accuracy of the same image segmented by thresholding method is 43%. Also in the second test image (17th May 2010) the performance of the neural classification is satisfactory with an overall accuracy of 95%.

| Image | Well classified Pixels | Misclassified pixels | Accuracy % |
|---|---|---|---|
| ETM+ (1$^{th}$, May 2010) | 4850 | 150 | 97% |
| ETM+ (10$^{th}$, May 2010) | 4950 | 50 | 99% |
| ETM+ (17$^{th}$, May 2010) | 4750 | 250 | 95% |

Table. 2. The error matrix of classified images shows the accuracy assessment

In Figures. 15b and 19b, some subareas of image collected at May 1$^{st}$ 2010 have been shown, where the better advantage of NN can clearly be observed based on visual interpretation.

The neural network simulator (SNNS) developed at the University of Stuttgart, Stuttgart, Germany, has been used for the classification algorithm implementation and proved to be a high level and reliable software package (Zell A., Mamier G. et al. 1995).

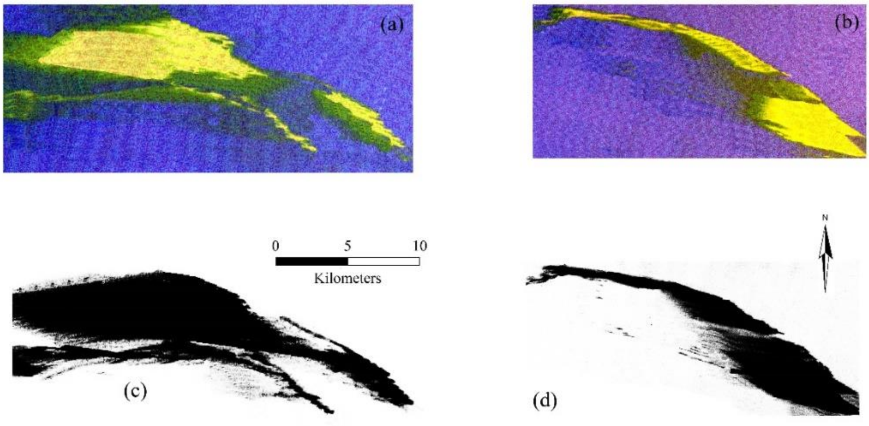


Figure. 19. Band ratioing and classification results. (a and b) Color composites of band ratioing for Landsat ETM+ data collected May 1st, 2010, in the Gulf of Mexico. (c and d) NN classification results of the images (a and b).

## Conclusion

In this study, the potential of Landsat ETM+ to automatically detect and extract oil spill in marine environment has been presented and demonstrated. The band ratioing approach found to work well for the identification of potential hydrocarbon contaminants in water.

It has been observed that the bands difference between bands 3 (660 nm) and 2 (560 nm), division ratio of bands 3 (660 nm) and 2 (560 nm) and division ratio of bands 4 (825 nm) and 2 (560 nm) normalized by band 1 (480 nm) were most suitable to retrieve oil spill.

MLPs with different topologies have been applied to a set of features describing oil spill characteristics in order to perform a supervised classification. Best performances are obtained using an MLP neural network with 3:4:2 topology trained by the standard backpropagation algorithm. This algorithm has been designed for Landsat ETM+ data but it can be applied on different multispectral data (WorldView2, Spot, etc.).

The largest challenge in detection of oil spills in SAR images is accurate discrimination between oil spills and look-alikes. Natural films cannot always be properly distinguished from oil spills based on a SAR image alone but additional information can be derived from optical sensors. Future oil spill systems should incorporate oil spill information from multisensory studies.

# Chapter III

# Active Oil Spill Remote Sensing expert systems

**Taravat, A.,** D. Latini and F. Del Frate (2014). "*Fully Automatic Dark-Spot Detection From SAR Imagery With the Combination of Nonadaptive Weibull Multiplicative Model and Pulse-Coupled Neural Networks.*" ***Geoscience and Remote Sensing, IEEE Transactions 52(3).***
**DOI:** 10.1109/TGRS.2013.2261076

**Taravat, A.,** F., Del Frate (2013). "*Weibull multiplicative model and machine learning models for full-automatic dark-spot detection from SAR images.*" ***Int. Arch. Photogramm. Remote Sens. Spatial Inf. Sci.*** XL-1/W3: 421-424
**DOI:** 10.5194/isprsarchives-XL-1-W3-421-2013

## Introduction

As I have already mentioned in chapter I, a numbers of remote sensing systems are available for detecting oil slicks, passive (i.e., optical sensors, infrared/ultraviolet systems, microwave radiometers) and active (i.e., laser fluorosensors and radar systems) (Fingas 2001, Brekke and Solberg 2005). Among them, synthetic aperture radar (SAR) (Table 2) can provide valuable synoptic information about the position and size of the oil spill due to its wide area coverage and day/night, and all-weather capabilities (Brekke and Solberg 2005, Ferraro, Meyer-Roux et al. 2009).

Detection of oil spills from SAR imagery can be divided into three steps (Brekke and Solberg 2005, Jones, Thankappan et al. 2006, Thankappan 2007):

- Dark feature detection,
- Computation and extraction of physical and geometrical features characterizing the dark feature, and
- Accurate discrimination between oil spills and look-alikes such as ice, internal waves, kelp beds, natural organics, jellyfish, algae, threshold wind speed areas (wind speed < 3 m/s) and rain cells.

These procedures can be done manually or automatically (Del Frate, Petrocchi et al. 2000, Nirchio, Sorgente et al. 2005, Karathanassi, Topouzelis et al. 2006, Keramitsoglou, Cartalis et al. 2006, Solberg, Brekke et al. 2007). As a preliminary task, dark-spot detection is a critical step prior to feature information extraction and classification. Furthermore, the accuracies of feature extraction and classification greatly rely on the accuracy of dark-spot detection. In addition, dark-spot detection is traditionally the most time-consuming of the three steps. Thus, an efficient and effective dark-spot detection approach is essential for developing automated oil-spill detection systems (Shu, Li et al. 2010).

In the literature, various types of models have been proposed for detecting dark spots. Manual selection by cropping a broader area containing the dark formation (Del Frate, Petrocchi et al. 2000, Lichtenegger, Calabresi et al. 2000). Threshold algorithms (adapted or not) (Solberg and Theophilopoulos 1997, Solberg, Storvik et al. 1999, Nirchio, Sorgente et al. 2005, Solberg, Brekke et al. 2007, Chang, Tang et al. 2008). Marked point and spatial density thresholding methods (Li and Li 2010, Shu, Li et al. 2010), wavelets (Wu and Liu 2003, Derrode and Mercier 2007) (Liu, Peng et al. 1997), fractal dimension estimation (Benelli and Garzelli June 28-July 2, 1999) (Marghany, Hashim et al. 2007), support vector machines (Mercier and Girard-Ardhuin 2006) and neural networks (Topouzelis, Karathanassi et al. 2007, Topouzelis, Karathanassi et al. 2008, Topouzelis, Stathakis et al. 2009).

There are two main difficulties occurring when using the automatic model for dark spots detection: (1) Speckles in SAR imagery due to the constructive and destructive interferences of the reflections from surfaces and (2) the contrast between dark spots and the background can vary, depending on the type of dark spot, the local sea state, the resolution, polarization and incidence angle of the SAR imagery (Bartsch 1987, Hielm 1989, Hühnerfuss 1996, Topouzelis 2008).

In the first phase of my research on SAR based oil spill remote sensing expert systems, I have tried to develop a fast, robust and effective automated approach that is adequate for practical oil-spill monitoring. The combination of non-adaptive Weibull Multiplicative Model (WMM) (Fernandes 1998, Fernandes 2001) with Pulse Coupled Neural Network (PCNN) (Karvonen 2004, Taravat, Latini et al. 2014) technique has been explored for achieving this goal.

Apart from using the common machine learning algorithms, the proposed approach further employs a WMM to enhance the separability between dark spots and the background. The idea is to separate the detection process into two main steps, WMM enhancement and Pulse Coupled Neural Network (PCNN) segmentation.

In the second phase of my research on active oil spill remote sensing expert systems, the combinations of adaptive Weibull Multiplicative Model (WMM) (Fernandes 1998, Fernandes 2001) with Multilayer Perceptron Neural Networks (MLP) (Karathanassi, Topouzelis et al. 2006, Topouzelis, Karathanassi et al. 2007, Topouzelis, Karathanassi et al. 2008), Radial Bases Function Neural Networks (RBF) (Topouzelis, Karathanassi et al. 2007), Support Vector Machine (SVM) (Pal and Mather 2005) have been explored too.

In both phases, first, the filter created based on weibull multiplicative model is applied to each sub-image which contains dark spots. Second, the sub-images are segmented by MLP, SVM, and PCNN. As the last step, a very simple filtering process is used to eliminate the false targets. A flowchart of the procedures is illustrated in Figure. 20.

| Satellite (Sensor) | Owner | Band |
|---|---|---|
| SEASAT | NASA | L |
| ALMAZ | RSA | S |
| ERS-1 | ESA | C |
| ERS-2 | ESA | C |
| RADARSAT-1 | CSA | C |
| RADARSAT-2 | CSA | C |
| ENVISAT (ASAR) | ESA | C |
| ALOS (PALSAR) | JAXA | L |
| TerraSAR-X | DLR | X |
| Cosmos Skymed-1/2 | ASI | X |
| Sentinel-1 | ESA | C |

Table. 2. Summary of oil spill remote sensing relevant Active spaceborne sensors

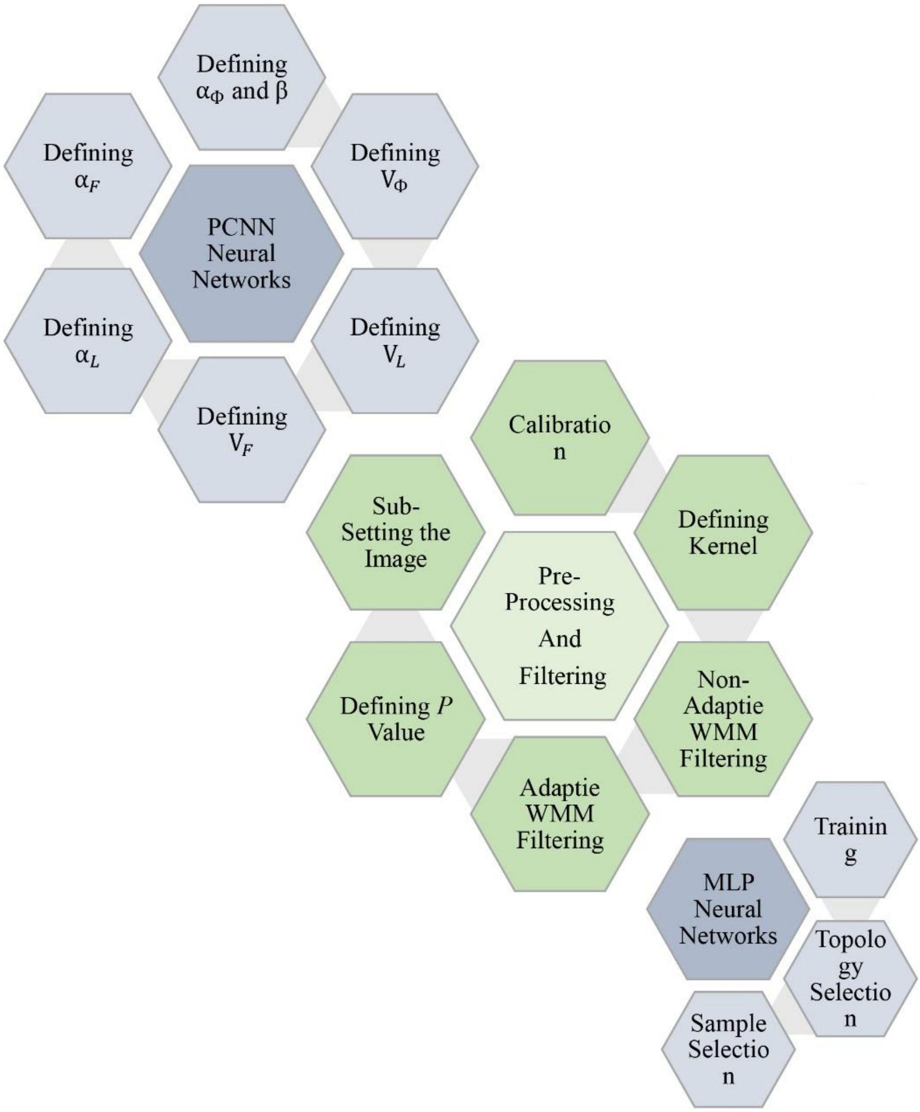


Figure. 20. An overview of the two phases of my research on active oil spill remote sensing expert systems.

## Fundamental properties of speckle in SAR images

### *Speckle Formation*

When a radar illuminates a surface that is rough on the scale of radar wavelength, the return signal consists of waves reflected from many elementary scatterers within a resolution cell. The distances between the elementary scatterers and the receiver vary due to the surface roughness, and, therefore, the received waves, although coherent in frequency, are no longer coherent in phase. A strong signal is received, if the waves add relatively constructively; a weak signal, if the waves are out of phase.

A SAR image is formed by coherently processing the returns from successive radar pulses. This effect causes a pixel to pixel variation in intensity, and this variation manifests itself as a granular pattern, called speckle. This pixel-to-pixel intensity variation in SAR images has a number of consequences, the most obvious one being that the use of a single pixel intensity value as a measure of distributed targets' reflectivity would be erroneous (Goodman 1976).

### *Rayleigh Speckle Model*

Consider a large number of scatterers in a resolution cell. The received signal is a vector sum of waves reflected from the scatterers. Let x and y denote its real and imaginary components. The intensity, I, defined as $I = x^2 + y^2$, is exponentially distributed (Ulaby 1989),

$$P_1(I) = (1/\sigma^2) \exp(-I/\sigma^2), \qquad I \geq 0$$

with mean $M_1(I) = \sigma^2$, and variance $var_1(I) = \sigma^4$. The amplitude, A, which is the square root of I, has a Rayleigh distribution,

$$P_i(A) = (2A / \sigma^2) \exp(-A^2 / \sigma^2), \qquad A > 0$$

with mean, $M_1(A) = \sigma \sqrt{\pi}/2$ , and variance, $Var_1(A) = (4-\pi)\ \sigma^2 / 4$

### *Filtering techniques for speckle reduction*

Speckle noise pixels do not reflect their real value measured on earth, so it is necessary to eliminate them by filtering radar images before doing any processing to obtain satisfactory results (Brekke and Solberg 2005).

A mean filter is often used for reducing speckle noise in radar images, even though it is not effective in preserving boundaries between different pixel values because this algorithm averages the pixel values at the active window. Median filter has been widely used with satisfactory results by Goodenough et al. (Goodenough, Guindon et al. 1980), Henninger and Carney (Henninger and Carney 1983), Mueller et al. (Mueller and Hoffer 1989).

More sophisticated spatial filtering techniques have been developed by Heigster (Heigster 1982), Mueller et al. (Mueller and Hoffer 1989), Touzi et al. (Touzi., Lopes et al. 1988), Lopes et al. (Lopes, Touzi et al. 1990, Lopes, Nezry et al. 1993), Nezry et al. (Nezry, Lopes et al. 1991), and Lee et al. (Lee 1980).

Moreover, a combination of different filters have proved to be appropriate (Topouzelis, Karathanassi et al. 2007). Liu et al. (2010) used A 3 × 3 Lee filter, followed by a 5 × 5 Lee filter and a 7 × 7 Median filter applied to the original image (Liu, Zhao et al. 2010). Topouzelis et al. (2008) used a combination of the Lee and Local Region filters (Topouzelis, Karathanassi et al. 2008). The combination applied to his study includes application of a 3 × 3 Lee filter to the original image, followed by a 5 × 5 Lee filter and a 7 × 7 Local Region filter which has been previously used with success for speckle removal for SAR (Rio and Lozano-García 2000, Karathanassi, Topouzelis et al. 2006).

Lee and Local Region filters had been widely used for speckle removal by several researchers (Sheng and Xia 1996, Arvelyna, Oshima et al. 2001, Capstick and Harris 2001).

### *Weibull Multiplicative Model (WMM) filter*

Traditionally, invoking the central limit theorem, it has been assumed that the real and the imaginary parts of the received wave follow Gaussian distribution which in turn lead to the Rayleigh distribution (Kuruoglu and Zerubia 2004).

Another popular model is the Weibull distribution which has shown high degree of success in modeling urban scenes and sea clutter (Most of the models were suggested based on empirical observations and were case specific) (Sekine and Mao 1990, Lee, Jurkevich et al. 1994, Fernandes 1998).

In this research I have used WMM (with the assumption that the amplitude or the intensity image has the Weibull distribution) in order to remove speckle and enhance the contrast between the dark spot and the background (Fernandes 2001). In SAR images the texture is embedded in the speckle, which is originated by the coherent reflection of waves in a rough surface.

WMM applies a non-linear transformation to generate the texture image from the original speckled image. The extraction of the texture image from the Weibull-distributed SAR image employs the local estimation of the scale and form parameters of the Weibull distribution (Fernandes 1998).

The Weibull-distributed random variable x with form parameter $\gamma_x > 0$ and scale parameter $\beta_x > 0$, has a probability density function given by:

$$f(x) = \frac{\gamma_x}{\beta_x}\left(\frac{x}{\beta_x}\right)^{\gamma_x - 1} \quad exp\left[-\left(\frac{x}{\beta_x}\right)^{\gamma_x}\right]$$

The m-order moment can be expressed as,

$$E[x^m] = m\beta_x^m \quad \Gamma(\mathrm{m}/\gamma_x)/\,\gamma_x$$

For $\gamma_x$= 2, the Weibull distribution becomes a Rayleigh distribution, for $\gamma_x$ = 1, it becomes an exponential distribution. It can be shown that $x^a$ with a > 0 is also Weibull distributed. If, z $= x^a$ with form and scale parameters given by, $\gamma_z = \gamma_x/a$ and $\beta_z = \beta_x^a$ follows that,

$$f(z) = \frac{\gamma_z}{\beta_z}\left(\frac{z}{\beta_z}\right)^{\gamma_z - 1} \quad exp\left[-\left(\frac{z}{\beta_z}\right)^{\gamma_z}\right]$$

Consider b, with a > b > 0 in such a way that:

$$\mathrm{z} = x^a = x^b x^{a-b} = \frac{x^b}{E[x^b]} E[x^b] x^{a-b} = st$$

Where (s) is the speckle, with unitary mean and (t) is the texture of the Weibull-distributed variable (z). z is the variable for the SAR image.

$$\mathrm{s} = x^b/E[x^b] \qquad\qquad \mathrm{t} = x^{a-b}E[x^b]$$

In this form, it is possible to express z as a multiplication of s by t, where s is the speckle and t is the texture of the Weibull-distributed variable z. The texture t has Weibull distribution with form and scale parameter given, respectively, by:

$$\gamma_t = {}^{\gamma_x}/_{(a-b)} \qquad \beta_t = \beta_x^{a-b} E[x^b]$$

and the speckle has Weibull distribution with form and scale parameter given, respectively, by:

$$\gamma_s = {}^{\gamma_x}/_{b} \qquad \beta_s = \beta_x^{b} / E[x^b]$$

Let

$$p = b/a\,, \quad 0 \le p < 1$$

Then

$$\text{t} = x^{a-b} E[x^b] = x^{a(p-1)} E[x^{ap}] = z^{(1-p)} E[z^p]$$

using p-order moment equation $\text{E}[z^p]$,

$$t = p\beta_z^p \quad \Gamma(\text{p}/\gamma_z)\text{z}^{1-p}/\,\gamma_z$$

Where t can be considered as the filtered image and the factor $0 \le p < 1$ gives the filtering intensity. If $p$ is close to one, then $a \approx b$ and the texture t is constant (high filtering) and if $p$ is close to zero then $a >> b$ and t ≈ z (low filtering). For each pixel in the Weibull-distributed image, $\gamma_z$ and $\beta_z$ are locally estimated in a window of dimension *N*x*N* surrounding the pixel to be filtered (Figure. 21).

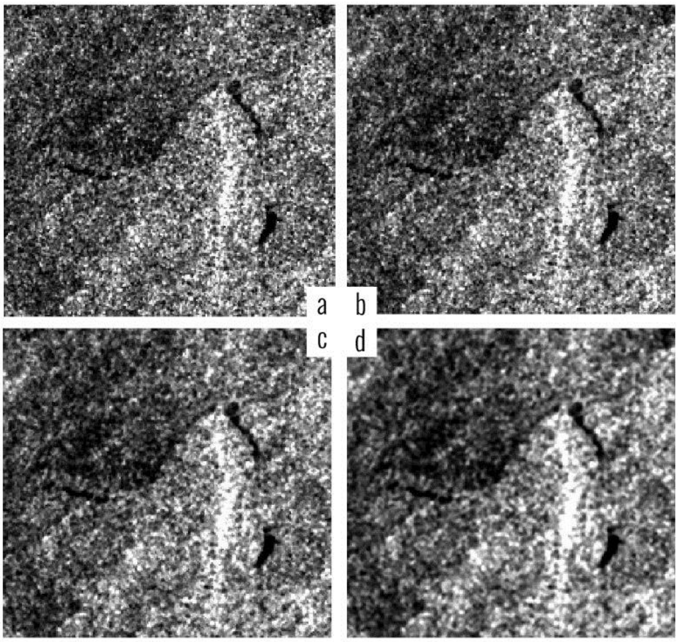


Figure. 21. Shows the effect of P parameter in an amplitude SAR C-band ENVISAT image. (a)The original image, (b) P=0.2, window 3x3, (c) P=0.5, window 3x3, (d) P=0.8, window 3x3.

The form parameter $\gamma s$ can be set as the mean or mode of $\gamma_z$ in the whole image. Using $\gamma_s = {}^{\gamma_x}/_{b}$ , it can be obtained that $\gamma_x = \gamma_s b$. Through $\gamma_z = \gamma_x / a$ and p = b/a < 1, p can be calculated adaptively as a function of $\gamma_z$ that is estimated locally as $\gamma_z / \gamma_s$ and the texture becomes:

$$t = \beta_z^{\gamma_z/\gamma_s}\, \Gamma(1/\gamma_s) \mathrm{z}^{1-(\gamma_z/\gamma_s)} / \gamma_s$$

If $\gamma_z \rightarrow \gamma_s$ , there is a stark filtering in the image and if $\gamma_z \ll \gamma_s$ there is a weak filtering and, if $\gamma_z > \gamma_s$ the texture equation holds, but it is not Weibull-distributed anymore.

## Experimental results: first phase (the combination of Non-adaptive WMM and PCNN)

In order to test the efficiency of the proposed approach, I used ENVISAT ASAR and ERS2 SAR data. ERS-2 SAR and ENVISAT-ASAR operate in C-band (4–8 GHz, λ 3.75–7.5 cm). ERS-2 SAR images of the precision image (PRI) product have a pixel size of 12.5 m x 12.5m with a swath width of 100 km.

ENVISAT ASAR images include the Image Mode (IM) and Wide Swath Mode (WSM) products. The IM product is similar to the PRI product of the ERS-2 SAR, while the WSM product has a spatial resolution of 150 m with a swath width of 450 km.

The dataset has been categorized into 4 groups (Table. 3) based on different types of dark spot and different sea status (Figure. 22). After calibration process, sub images containing anomalies were extracted to make extraction and image interpretation more expedient. The test dataset contains 40 images with 256×256 pixels, 20 images with 512×512 pixels. This 60 images dataset contains all potential anomalies detected under a variety of sea conditions.

Table. 1. Dark spot types categories based on different types of dark spots and different sea statues

| Dark spot types | Description |
|---|---|
| Massive Well-Defined Dark Spot | A massive dark spot located within a homogeneous background where the boundary between the dark spot and the surrounding water is very clear |
| Linear Well-Defined Dark Spot | A linear dark spot located within a homogeneous background where the boundary between the dark spot and the surrounding water is very clear (eg. Oil spills discharged by ships) |
| Massive Not Well-Defined Dark Spot | A massive dark spot within a homogeneous background where the boundary between the dark feature and the surrounding water is not well defined |
| Linear Not Well-Defined Dark Spot | A linear dark spot within a homogeneous background where the boundary between the dark feature and the surrounding water is not well defined |

Standard radar image pre-processing procedures using the Next ESA SAR Toolbox (NEST) version 4C-1.1 software were applied to the images. This included radiometric calibration to generate a backscatter ($\sigma^0$) image, and geometric correction to georeference the input images into the Universal Transverse Mercator projection with the World Geodetic System 1984 as datum.

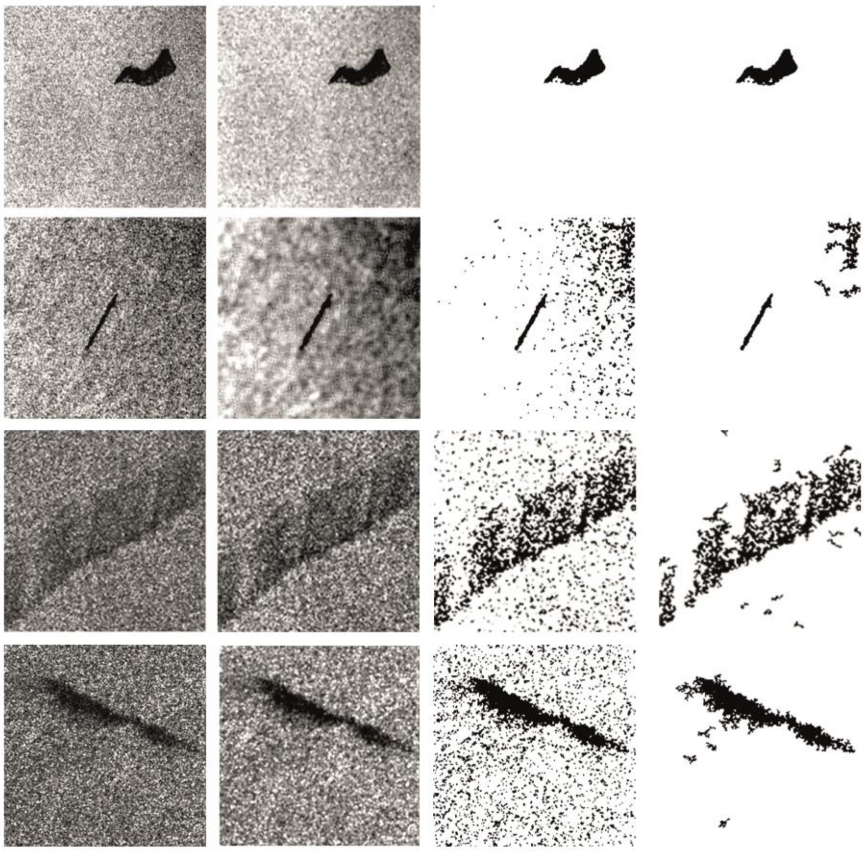

Figure. 22. Results of the proposed approach on four typical examples. (First Col) Original SAR images after pre-processing. (Second Col) Non-adaptive WMM Filtering. (Third Col) PCNN results. (Fourth Col) final results after post processing.

The first column of Figure. 22. shows the original images after pre-processing. The results of non-adaptive WMM filter and PCNN segmentation are presented in the second and third column Figure. 22, respectively.

In fourth column of Figure. 22 the final results after post processing have been shown. A well-defined massive dark spot and linear dark spot located within a homogeneous background where the boundary between the dark spot and the surrounding water is very clear are displayed in the first and second rows, respectively. The third and fourth rows show the detection of a not-well-defined massive dark spot and linear dark spot within a homogeneous background (the boundary between the dark feature and the surrounding water is not well defined) (Li and Li 2010, Shu, Li et al. 2010).

In PCNN model the setting of the parameters ($\alpha_L$, $\alpha_F$, $\alpha_\theta$, $V_L$, $V_F$, $V_\theta$ and $\beta$) represents the fundamental task in phase of design project, because it must have the capability, and sensitivity, to fit at the dynamics range of the backscattering values in the scene.

The parameters values need some adjustment according to the type of data. However, no further tuning is in general necessary once the sensor (Envisat, Cosmosky-Med, TerraSAR-X, RADARSAT-1 ScanSAR, etc…) and the product (Wide Swath, Spotlight, Strip map, etc…) are defined. The best visual detection results are the results where the WMM model removes the noisy pixels in the images while preserving texture information.

In this experimental work a unique best setting has been obtained (by trial and error) for both ENVISAT and ERS products, using parameter's values as follow: $\alpha_L$=0.3, $\alpha_F$=1, $\alpha_\theta$=1, $V_L$=0.6, $V_F$=0.8, $V_\theta$=1.2 and $\beta$=0.4. The 3x3 square matrixes of synaptic weights M and W are defined with a linking radius r=1.5, therefore the considered pixel receives linking inputs from the eight neighbors.

The weighting factor for a linking input is $1/d^2$, where d is defined as the Euclidean distance from the considered pixel. For every elaboration, the iteration which produces the most accurate binary segmentation among the sequence of output is often the third or fourth, leading to fast processing time, in the range from 2 to 5 seconds.

After applying the classification, some regions may have been incorrectly detected as dark spots.  A very simple filtering process is used to eliminate these false targets as the post-processing step. By using this filter, all the objects with the area less than 20 pixels omit from the processed image.

For accuracy assessment, from each sub-image 500 pixels have randomly been selected and then labeling made by visual interpretation (although further expansion is required for accuracy assessment e.g. using ground true data). The distance for measuring commission error, omission error, is set as one pixel. The results have been compared with the results of thresholding algorithm (applied to the same dataset) which is a very popular method in this field, and also with the results of the latest method in literature presented by Shu, et al. 2010 (Shu, Li et al. 2010) to demonstrate the effectiveness of the proposed approach.

In Shu, et al. 2010 model, the intensity threshold segmentation is applied to each window which is passed through the entire SAR image. Pixels with intensities below the threshold are regarded as potential dark-spot pixels while the others are potential background pixels. Then, the density of potential background pixels is estimated using kernel density estimation. Pixels with densities below a certain threshold are the real dark-spot pixels. At the last step, they used a contrast threshold to eliminate false targets (Shu, Li et al. 2010).

The average accuracy applied to the whole test dataset is 93.53 % with a standard deviation of 3.8 whereas the accuracy of the same dataset segmented by thresholding method is 67 %. In the worst case, the accuracy of 84.88 % was produced. The results of the accuracy assessment applied to the different types of anomalies are displayed in table. 4. and table. 5. As can be seen, the approach achieves satisfactory results on the well-defined dark spots than the not-well-defined ones.

The average accuracy for the well-defined dark spots is 96.97 % with a standard deviation of 0.67 and 2.75 % commission error average versus 90.09 % with a standard deviation of 2.25 and 11.00 % commission error average for the not-well-defined ones whereas in Shu, 2010' s work (Shu, Li et al. 2010) the average commission error for the well-defined dark spots is 5.5% versus 10.8% for the not-well-defined ones and the average omission error is 3.7% for the well-defined dark spots compared to 12.1% for the not-well-defined ones.

Table. 4. The average values of the accuracies for different types of anomalies.

| | Min % | Max % | Mean % | St.Dev |
|---|---|---|---|---|
| Well-Defined | 96.0 | 98.18 | 96.97 | 0.67 |
| Linear Well-Defined | 96.00 | 98.18 | 97.00 | 0.73 |
| Massive Well-Defined | 96.20 | 98.18 | 96.94 | 0.64 |
| Not Well-Defined | 84.88 | 93.75 | 90.09 | 2.25 |
| Linear Not Well-Defined | 85.00 | 93.75 | 90.36 | 2.36 |
| Massive Not Well-Defined | 84.88 | 92.23 | 89.81 | 2.22 |
| Linear Dark Spot | 85.00 | 98.18 | 93.68 | 3.79 |
| Massive Dark Spot | 84.88 | 98.18 | 93.38 | 3.98 |

Table. 5. The average values of commission and emission error (In %) achieved by WMM & PCNN for different groups of data

| | Min Om | Max Om | Mean Om | St.Dev Om | Min Cm | Max Cm | Mean Cm | St.Dev Cm |
|---|---|---|---|---|---|---|---|---|
| Well-Defined | 1.82 | 4.00 | 3.02 | 0.67 | 1.65 | 4.00 | 2.75 | 0.67 |
| Linear Well-Defined | 1.82 | 4.00 | 2.99 | 0.73 | 1.80 | 4.00 | 2.67 | 0.69 |
| Massive Well-Defined | 1.82 | 3.80 | 3.05 | 0.64 | 1.65 | 3.90 | 2.83 | 0.67 |
| Not Well-Defined | 6.25 | 15.12 | 9.90 | 2.25 | 8.20 | 14.20 | 11.00 | 1.84 |
| Linear Not Well-Defined | 6.25 | 15.00 | 9.63 | 2.36 | 8.20 | 13.60 | 10.32 | 1.88 |
| Massive Not Well-Defined | 7.77 | 15.12 | 10.18 | 2.22 | 9.40 | 14.20 | 11.70 | 1.59 |
| Linear Dark Spot | 1.82 | 15.00 | 6.31 | 3.80 | 1.80 | 1.36 | 6.49 | 4.15 |
| Massive Dark Spot | 1.82 | 15.12 | 6.62 | 3.98 | 1.65 | 14.20 | 7.26 | 4.69 |

The approach generates almost a similar accuracy on well-defined linear dark spots and well-defined massive dark spots but commission errors on linear dark spots are fewer in compare to massive dark spots. The average accuracies are 93.68 % with 6.49 % and 6.31 % commission and omission errors average and 93.38 % with 7.26 % and 6.62 % commission and omission errors average for the linear and massive dark spots, respectively, whereas in Shu, 2010’s work (Shu, Li et al. 2010) the average commission and omission errors for the linear dark spots are 9.4% and 10.5% compared to 5.4% and 2.9% for the massive dark spots, respectively.

The worst accuracies are 85.00 % with 13.60 % commission error and 84.88 % with 14.20 % commission error which is obtained for not well-defined linear dark spots and not well-defined massive dark spots.

It is necessary to identify the situations where the proposed approach generates poor accuracy and see why this method failed to work correctly in those cases. In general, the accuracy decreases in some cases because of the Wide Swath products and the strong variation of incidence angle from near to far range which affects the dynamic range of digital numbers.

Figure. 23 illustrates two typical examples. In Figure. 23 (first row), our approach failed because a very fresh oil spill is presented in a bright background and the contrast in some sections is too low. In Figure. 23 (second row), our approach failed because the background is heterogeneous and a large number of false alarms occur on the images after applying PCNN. Moreover, most of the false alarms are interconnected and difficult to remove using post-processing without affecting the detection of the real dark spot.

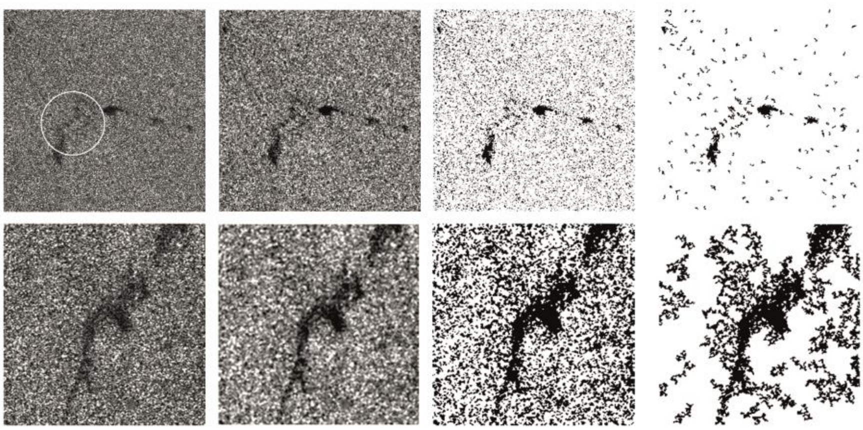

Figure. 23. Result of the proposed approach: First row is an example where a very fresh oil spill is presented in a homogeneous background and second row is an example where a not well-defined dark spot located in a very heterogeneous background (wind speed and sea state cause this heterogeneity).

Based on the authors' knowledge, the fastest method which has been reported in the literature is the spatial density thresholding model presented by Shu, et al. 2010 with the speed of 11 seconds (Shu, Li et al. 2010). Another example is the marked point process model, presented by Li, Y. and J. Li, 2010 (Li and Li 2010) which takes about half an hour to complete dark-spot detection on a 512×512 image using a MATLAB software.

Also the support vector machine method, presented by Mercier, G. and F. Girard-Ardhuin, 2006 (Mercier and Girard-Ardhuin 2006) which takes about a minute to complete dark-spot detection on a 512×512 image using a 1.8-GHz Linux Laptop.

Dark-spot detection by the proposed approach with a 512×512 image can be completed in about 7 seconds on a pc with an Intel Pentium dual-core, a speed of 2.2 GHz and a RAM memory of 2.00 GB which is rather competitive with respect to existing methods in the literature. This might have a significant impact on the reduction of the computational burden when large datasets need to be processed.

### Experimental results: second phase (the combination of adaptive WMM and MLP)

In this phase of my research, an attempt has been made to present an approach which overcomes the Non-adaptive WMM filter setting parameters by developing an adaptive WMM model which is a step ahead towards full automatic dark spot detection model discussed in the previous phase. Furthermore a pixel based classification model (Multilayer Perceptron Neural Networks) has been applied to the dataset to check the capability of a pixel based classification model in order to increase the accuracy of the discussed model in the previous section.

Like the previous phase, the model has been tested on a dataset of ENVISAT-ASAR (Image Mode (IM) and Wide Swath Mode (WSM) products which have a spatial resolution of 150 m with a swath width of 450 km) and ERS2-SAR (the precision image (PRI) product which has a pixel size of 12.5 m x 12.5 m with a swath width of 100 km) images.

I applied adaptive WMM filter to all 60 test images. The similarity of adaptive and non-adaptive WMM filtered image has been shown in figure. 24 In the example shown in figure. 24, the filtering intensity P = 0.7 and a 3x3 window has been used for Non-adaptive WMM (which is the best Non-adaptive WMM parameter combination for filtering SAR images).

Removing the noisy pixels in the images by using adaptive WMM overcomes the Non-adaptive WMM filter setting parameters while preserving the same accuracy of non-adaptive model, which is a step ahead towards full automatic dark spot detection model discussed in the previous phase.

In the classification phase by MLP approach, the number of units in the hidden layer and the training/testing phase settings (number of training cycles and the pixel selection for training/test the model) represent the fundamental tasks. Adjustment of these parameters affects the capability and sensitivity of the model to fit at the dynamics range of the backscattering values in the scene.

Several attempts have been made to properly select the number of units to be considered in the hidden layers. The pixels for train/test the net are 7,000 pixels which extracted from different types of dark spot and different sea status. The tested windows were chosen to be as different as possible in order to test the neural networks ability to generalize different types of dark formations. The training sets contain 60% and the test sets contain 40% of all pixels which are not belonging to the training sets.

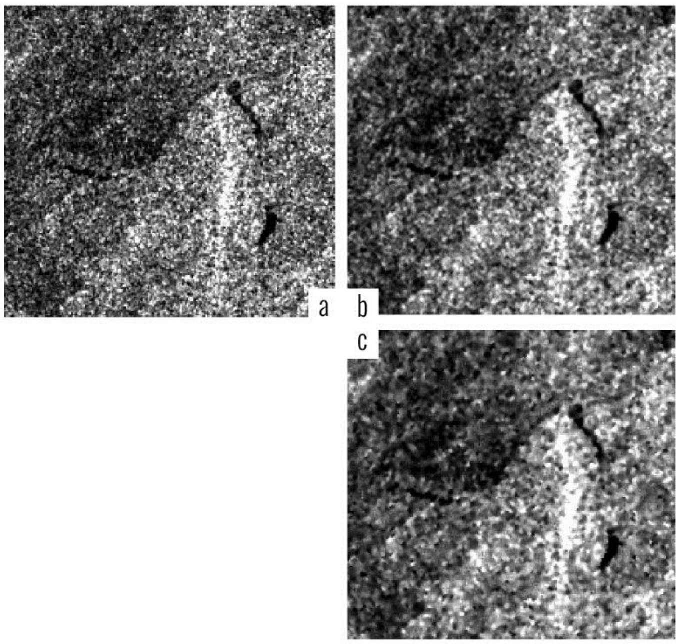


Figure. 24. Shows an example of adaptive (b) and Non-adaptive (c) WMM filters of the original images (a).

Pixel selection for train/test set has been done randomly and repeated six times. The presented results of root mean square error (RMSE) errors in figure. 25. are the average of these repetitions for each topology. The topology 1-4-2 has been finally chosen for its good performance in terms of classification accuracy, RMSE, and training time.

The number of about 5,000 training cycles was sufficient to get the network learned. The input of the net is the filtered image and the output providing classified pixels in terms of oil spill or others. One MLP NNs has been used for classifying all images. However, after training the network for one specific sensor and product, no further tuning is necessary.

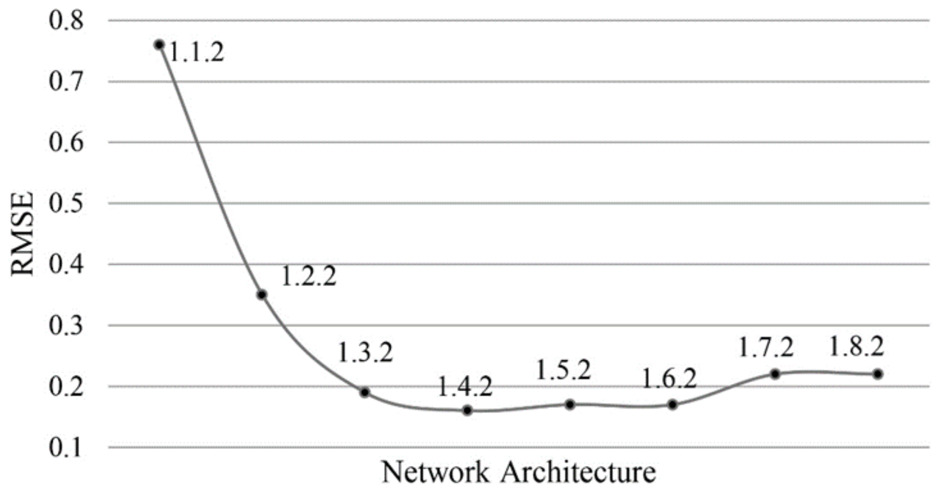


Figure. 25. RMSE errors for different NN topologies.

The results of the accuracy assessment have been compared with the results of Non-adaptive WMM & PCNN (Weibull Multiplicative Model and Pulsed Coupled Neural Networks) model presented in the previous phase.

Non-adaptive WMM & PCNN generates poor accuracy in some cases because of the Wide Swath products and the strong variation of incidence angle from near to far range which affects the dynamic range of digital numbers. The reason for comparing the presented results with the Non-adaptive WMM & PCNN results is to test the capability of the adaptive WMM & MLP model for increasing the accuracy of full automatic dark spot detection by using the Non-adaptive WMM & PCNN model.

Figure. 26 shows two sample test images from different types of dark spot and different sea status (the cases which Non-adaptive WMM & PCNN generates poor accuracy). The results of adaptive WMM filter and MLP segmentation are presented in the second and third row figure. 26, respectively. In fourth row figure. 26, the final results after post processing have been shown.

A not-well-defined massive dark spot and a not-well-defined linear dark spot are displayed in right and left columns, respectively. Not-well-defined dark spots occur when a very fresh oil spill is presented in a bright background or the background is heterogeneous and a large number of false alarms occur on the images after applying the model.

The whole test dataset (Segmented by MLP) accuracy has increased with 1.1 % and a significant improvement in standard deviation of 1.3 (94.65 % with a standard deviation of 2.5) in compared to the same dataset segmented by non-adaptive WMM & PCNN (93.53 % with a standard deviation of 3.8).

In the worst case, the accuracy of 87 % was produced which is higher than the worst case accuracy segmented by non-adaptive WMM & PCNN (which is 84.88 %). The results of the accuracy assessment applied to the different types of anomalies are displayed in table. 6 and table. 7.

The approach generates almost a similar accuracy on well-defined dark spots (well-defined linear dark spots accuracy is 96.70 % with a standard deviation of 0.64 and well-defined massive dark spots accuracy is 96.98 % with a standard deviation of 0.62) in compared to the accuracy on well-defined dark spots segmented by non-adaptive WMM & PCNN (well-defined linear dark spots accuracy is 97 % with a standard deviation of 0.73 and well-defined massive dark spots accuracy is 96.94 % with a standard deviation of 0.64).

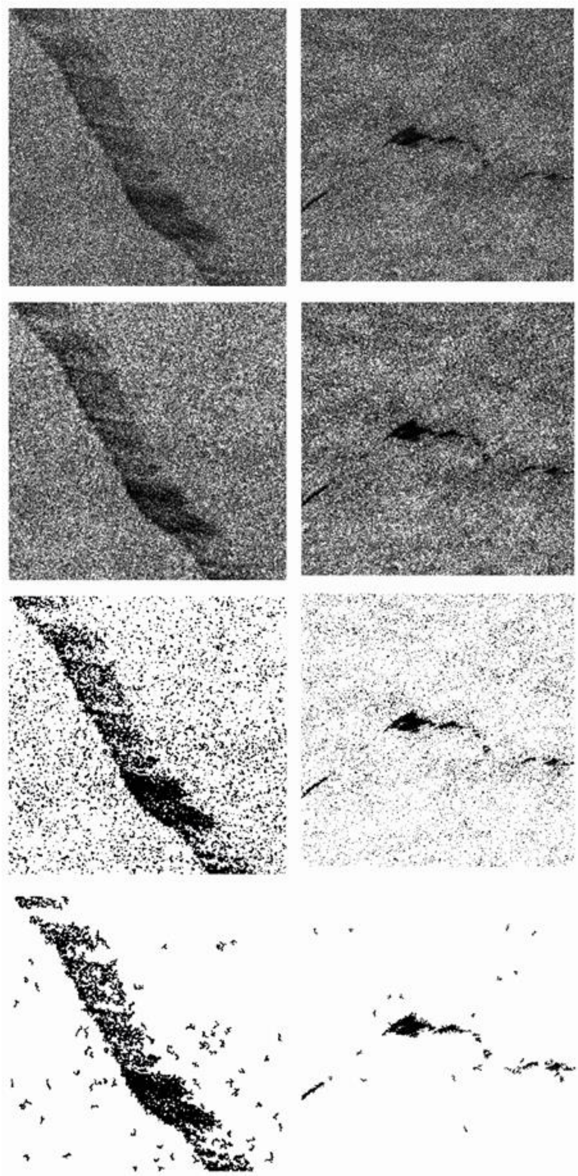

Figure. 26. Results of MLP on two typical examples where Non-adaptive WMM & PCNN generates poor accuracy.

Table. 6. The average values of the accuracies for different types of anomalies.

| | Min% | Max% | Mean% | StDev |
|---|---|---|---|---|
| Well-Defined | 95.50 | 98.00 | 96.70 | 0.64 |
| Linear Well-Defined | 95.50 | 97.80 | 96.50 | 0.59 |
| Massive Well-Defined | 96.00 | 98.00 | 96.98 | 0.62 |
| Not Well-Defined | 87.00 | 94.00 | 92.55 | 1.81 |
| Linear Not Well-Defined | 87.00 | 94.00 | 92.97 | 2.00 |
| Massive Not Well-Defined | 87.50 | 93.10 | 92.13 | 1.58 |
| Linear Dark Spot | 87.00 | 97.80 | 94.74 | 2.31 |
| Massive Dark Spot | 87.50 | 98.00 | 94.55 | 2.74 |

As it is expected, a significant improvement of 2.46 % in accuracy (with the improvement of 0.44 in standard deviation and 2.4 % in commission error) has been detected on the not well-defined dark spot dataset segmented by adaptive WMM & MLP (not well-defined linear dark spots accuracy is 92.97 % with a standard deviation of 2.00 and commission error of 8.22 %. Not well-defined massive dark spots accuracy is 92.13 % with a standard deviation of 1.58 and commission error of 8.97 %) in compared to the same dataset segmented by non-adaptive WMM & PCNN (not well-defined linear dark spots accuracy is 90.36 % with a standard deviation of 2.36 and commission error of 10.32 %. Not well-defined massive dark spots accuracy is 89.81 % with a standard deviation of 2.22 and commission error of 11.70 %.).

Table. 7. The average values of emission and commission error (In %) achieved by adaptive WMM & MLP.

| | Min Om | Max Om | Mean Om | StDev Om | Min Cm | Max Cm | Mean Cm | StDev Cm |
|---|---|---|---|---|---|---|---|---|
| Well-Defined | 2.00 | 4.50 | 3.25 | 0.64 | 1.10 | 3.50 | 2.30 | 0.62 |
| Linear Well-Defined | 2.20 | 4.50 | 3.48 | 0.59 | 1.10 | 3.50 | 2.24 | 0.62 |
| Massive Well-Defined | 2.00 | 4.00 | 3.01 | 0.62 | 1.40 | 3.20 | 2.37 | 0.64 |
| Not Well-Defined | 6.00 | 13.0 | 7.44 | 1.81 | 6.20 | 11.4 | 8.60 | 1.36 |
| Linear Not Well-Defined | 6.00 | 13.0 | 7.00 | 2.00 | 6.20 | 10.3 | 8.22 | 1.04 |
| Massive Not Well-Defined | 6.90 | 12.5 | 7.86 | 1.58 | 6.50 | 11.4 | 8.97 | 1.58 |
| Linear Dark Spot | 2.20 | 13.0 | 5.20 | 2.31 | 1.10 | 10.3 | 5.23 | 3.17 |
| Massive Dark Spot | 2.00 | 12.5 | 5.44 | 2.74 | 1.40 | 11.4 | 5.67 | 3.57 |

The worst accuracies are 87.00 % with 10.3 % commission error and 87.5 % with 11.4 % commission error which are obtained for not well-defined linear dark spots and not well-defined massive dark spots that are 2 % with 3.3 % commission error and 2.62 % with 2.8 % commission error higher than the worst accuracies obtained by non-adaptive WMM & PCNN for not well-defined linear dark spots and not well-defined massive dark spots, respectively.

MLP Neural Networks (as a pixel based classification model) is less sensitive to noise and gives good performance for spots with weak edges because they utilize the statistical information within or outside the training set and this is the reason of the higher accuracies obtained by adaptive WMM & MLP for not well-defined linear dark spots and not well-defined massive dark spots in compared to the accuracies obtained by non-adaptive WMM & PCNN for not well-defined linear dark spots and not well-defined massive dark spots.

## Conclusions

In this phase of my research, an attempt has been made to demonstrate the power of using the combination of WMM with PCNN and MLP as automated methods for dark-spot detection in SAR imageries. To test the capability of the proposed approach, I applied it to a dataset containing 60 ENVISAT, ERS2 images which cover all potential anomaly cases. The same parameters were used for all the test images.

Adaptive WMM model presented in this study overcomes the non-adaptive WMM filter setting parameters which is a step ahead towards full automatic dark spot detection model. The average accuracy for the overall dataset segmented by PCNN is 93.66 % and the average computational time for a detection window was 7 seconds using IDL software.

To study the detectability of different types of dark spots, I divided the test dataset into four groups. Results showed that this approach works best when the dark spots are well-defined or are located within a homogeneous background. It is less effective when the dark spots are not well-defined or are located within a heterogeneous background.

The whole test dataset (segmented by MLP NNs) accuracy is 94.65 % which is higher than the same dataset segmented by non-adaptive WMM & PCNN (93.53 %). The approach generates almost a similar accuracy on well-defined dark spots in compared to the accuracy on well-defined dark spots segmented by non-adaptive WMM & PCNN. Results showed that this approach works better in the situations (not well-defined linear dark spots and not well-defined massive dark spots) where non-adaptive WMM & PCNN generates poor accuracy.

A difficulty that is experienced in the use of many ANN models is the determination of appropriate characteristics for the training data, the architecture of the network (number of layers and nodes) and the method to avoid overtraining but once the topology and the other parameters are set, it can be used easily and very fast.

An important issue at operational level is the quality of the input images for automatic detection algorithms. Some considerations on the expected level of quality can be made in order to avoid false alarms or missed detections due to the data.

Further research is necessary to improve the accuracy of dark-spot detection when the dark spots are not-well-defined. The proposed approach can be applied to the future spaceborne C-band SAR which will replace with Sentinel-1 mission just with some parameters adjustment based on the type of data.

# Chapter IV

# Conclusion and suggestions for further work

In this work the capabilities of different remote sensing sensors have been evaluated in terms of their usefulness for detecting and monitoring oil spills. In fact, no single sensor can provide all the information needed for oil spill surveillance and many European and North American agencies are using a combination of sensors for oil spill monitoring. For both the optical and the SAR case the crucial detection problem has been effectively approached using a NN approach which has been varied according to the specific situation.

In the first phase of my study, the potential MLP NNs algorithm to automatically detect and extract oil spill in marine environment from Landsat ETM+ images has been presented and validated. In the second phase of my research, an attempt has been made to demonstrate the power of using the combination of WMM with PCNN and MLP as automated methods for dark-spot detection in SAR imagery. We can conclude that these machine learning algorithms have demonstrated once more their effectiveness, either in terms of accuracy of the results or in terms of computational burden, in handling data processing tasks in remote sensing. It has to be noted that the designed methodology can be easily extended to other sensors, in particular to the Sentinel missions, and that at this point the design of a multi-frequency platform suitable for the concurrent analysis of different data providers is straightforward. This will help to significantly improve the temporal resolution of the future oil spill detection services.

Regarding the future work, we think that most of the efforts should be dedicated on one side to improve the accuracy of the algorithms, for example including as input information also the possible presence of a ship in the surrounding of the dark spot, and on the other one to gain more information about the analyzed event. In particular the estimation of the quantity of oil dispersed and its type should be the main problems to be considered in future research activities. Addressing such issues, the potential of polarimetric SAR as available on RADARSAT-2 or TerraSAR-X data should be deeply investigated as well as the capabilities provided by the L-band UAVSAR system, characterized by a very low Noise

Equivalent Sigma Zero (NESZ), which is a rather important feature in this context.

Although at present there are several operational near real-time oil spill detection services such as European Maritime Safety Agency (EMSA) called as Clean SeaNet, the automatic systems have been tested off-line, so more validation activities should be performed for their assessment. On the other hand the increase of the automatic level in the operational schemes would be desired for a better exploitation of all satellite data that are going to be available in the next future.

## Acknowledgments

I wish to thank Prof. David Fernandes, Head of telecommunications department, Centro Técnico de Aeronáutica (CTA) - Instituto Tecnológico de Aeronáutica (ITA ), Brazil for their valuable cooperation and helpful suggestions. Data for my research has been provided by European Space Agency (ESA) on the Cat-1 proposal number 13926. The content included in this thesis, such as text, graphics, company names, brand names, images, data compilations, and software, is the property of their respective owners which has been cited accordingly.

# References


Anderson, J., J. Neff, B. Cox, H. Tatem and G. Hightower (1994). "Characteristics of Dispersions and Water-Soluble Extracts of Crude and Refined Oils and Their Toxicity to Estuarine Crustaceans and Fish." Mar Bio **75**.

Arora, M. K. and G. M. Foody (1997). "Log-linear modelling for the evaluation of the variables affecting the accuracy of probabilistic, fuzzy and neural network classifications." International Journal of Remote Sensing **18**(4): 785-798.

Arvelyna, Y., M. Oshima, A. Kristijono and I. Gunawan (2001). Proceedings of ACRS 2001—22nd Asian Conference on Remote Sensing.

Atkinson, P. M. and A. R. L. Tatnall (1997). "Neural networks in remote sensing - Introduction." International Journal of Remote Sensing **18**(4): 699-709.

Avezzano, R. G., F. Del Frate and D. Latini (2012). "Fully Automatic Oil Spill Detection from Cosmo-Skymed Imagery Using a Neural Network Approach." Sar Image Analysis, Modeling, and Techniques Xii **8536**.

Avezzano, R. G., D. Velotto, M. Soccorsi, F. Del Frate and S. Lehner (2011). "Neural Networks for Oil Spill Detection using TerraSAR-X Data." Sar Image Analysis, Modeling, and Techniques Xi **8179**.

Barbara E. Ornitz , M. A., Champ (2002). Oil spills first principles:prevention and best response, Elsevier.

Barbini, R., R. Fantoni, A. Palucci, S. Ribezzo, and H.J.L. (1991). "Fluorosensor lidar for environmental diagnostics." Quantum Electronics and Plasma Physics **29**: 383-387.

Bartsch, N., Gruner, K, Keydel, W, Witte (1987). "Contribution to Oil Spill Detection and Analysis with Radar and Microwave Radiomete: Results of the Archimedes II Campaign." IEEE Trans Geosci Remote.

Bartsch, N., Grüner, K., Keydel, W., Witte, F. (1987). "Contribution to Oil Spill Detection and Analysis with Radar and Microwave Radiometer: Results of the Archimedes II Campaign." IEEE Transactions on Geoscience and Remote Sensing **GE.25**(6): 677-690.

Belore, R. C. (1982). "Adevice for measuring oil slick thickness." Spill Tech. **7**(2): 44-47.

Benediktsson, J. A. and J. R. Sveinsson (1997). "Feature extraction for multisource data classification with artificial neural networks." International Journal of Remote Sensing **18**(4): 727-740.

Benediktsson, J. A., P. H. Swain and O. K. Ersoy (1990). "Neural network approaches versus statistical-methods in classification of multisource remote-sensing data." Ieee Transactions on Geoscience and Remote Sensing **28**(4): 540-552.

Benediktsson, J. A., P. H. Swain and O. K. Ersoy (1993). "Conjugate-gradient neural networks in classification of multisource and very-high-dimensional remote-sensing data." International Journal of Remote Sensing **14**(15): 2883-2903.

Benelli, G. and A. Garzelli (June 28-July 2, 1999). Oil-Spills Detection in SAR Images by Fractal Dimension Estimation. International Geoscience and Remote Sensing Symposium (IGARSS'99), Hamburg, Germany.

Borak, J. S. and A. H. Strahler (1999). "Feature selection and land cover classification of a MODIS-like data set for a semiarid environment." International Journal of Remote Sensing **20**(5): 919-938.

Brekke, C. and A. H. S. Solberg (2005). "Oil spill detection by satellite remote sensing." Remote Sensing of Environment **95**(1): 1-13.

Brown, C. and M. Fingas (2003a). "Review of the development of laser fluorosensors for oil spill application." Marine Pollution Bulletin **47**: 477-484.

Brown, C. and M. Fingas (2005). A review of current global oil spill surveillance, monitoring and remote sensing capabilities. 28th Arctic and Marine Oil Spill Program (AMOP), Tech. Seminar Calgary, Canada.

C. M. Bishop (2007). Pattern Recognition and Machine Learning. New York, Springer.

Calleri, F. a. P. L. B. (1993). Airborne fluorescence lidar system. Intl. Symp. Operationalization of Remote Sensing, Enschede: ITC.

Capstick, D. and R. Harris (2001). International Journal of Remote Sensing **18**: 3627.

Carpenter, G. A., S. Gopal, S. Macomber, S. Martens, C. E. Woodcock and J. Franklin (1999). "A neural network method for efficient vegetation mapping." Remote Sensing of Environment **70**(3): 326-338.

Chang, L., Z. S. Tang, S. H. Chang and Y. L. Chang (2008). "A region-based GLRT detection of oil spills in SAR images." Pattern Recognition Letters **29**(14): 1915-1923.

Chitroub, S. (2005). "Neural network model for standard PCA and its variants applied to remote sensing." International Journal of Remote Sensing **26**(10): 2197-2218.

Civco, D. L. (1993). "Artificial neural networks for land-cover classification and mapping." International Journal of Geographical Information Systems **7**(2): 173-186.

D. J. C. MacKay (2003). Information Theory, Inference, and Learning Algorithms. Cambridge, U. K., Cambridge University Press.

Del Frate, F., D. Latini and C. Pratola (2010). "Automatic object extraction from VHR satellite SAR images using Pulse Coupled Neural Networks." Sar Image Analysis, Modeling, and Techniques X **7829**.

Del Frate, F., A. Petrocchi, J. Lichtenegger and G. Calabresi (2000). "Neural networks for oil spill detection using ERS-SAR data." Ieee Transactions on Geoscience and Remote Sensing **38**(5): 2282-2287.

Del Frate, F. and L. Salvatori (2004). "Oil spill detection by means of neural networks algorithms: A sensitivity analysis." Igarss 2004: Ieee International Geoscience and Remote Sensing Symposium Proceedings, Vols 1-7: 1370-1373.

Derrode, S. and G. Mercier (2007). "Unsupervised multiscale oil slick segmentation from SAR images using a vector HMC model." Pattern Recognition **40**: 1135−1147.

Dick, R., Fruhwirth, M, Brown, C. (1992). Laser Fluorosensor Work in Canada. First Thematic Conference on Remote Sensing for Marine and Coastal Environments, ERIM.

Dyring, A., Fast, O. (2004). "MSS Puts the Aircraft in the Oil Spill Tracking Network." Interspill.

Eckhorn, R., H.J., Reitboeck, M., Arndt, P.W., Dicke, (1989). A neural network for feature linking via synchronous activity: results from cat visual cortex and from simulations. Cambridge, UK, Cambridge University Press.

Eckhorn, R., H.J., Reitboeck, M., Arndt, P.W., Dicke, (1990). "Feature linking via synchronization among distributed assemblies: simulation of results from cat cortex." Neural Computing **2**: 293–307.

Fay, J. A. (1971). Physical processes in the spread of oil in the surface layers of the North Sea. Proceedings of the Joint Conference on Prevension and Control of Oil Spills, Petroleum Institute, International Maritime Organisation, London.

Fernandes, D. (1998). Segmentation of SAR Images with Weibull Distribution. Proceedings of the IGARSS.

Fernandes, D. (2001). Weibul Texture Filter (WTF) for SAR images. Proceedings of the IGARSS.

Ferraro, G., S. Meyer-Roux, O. Muellenhoff, M. Pavliha, J. Svetak, D. Tarchi and K. Topouzelis (2009). "Long term monitoring of oil spills in European seas." International Journal of Remote Sensing **30**(3): 627-645.

Fingas, M. (2001). The basics of oil spill cleanup, Lewis Publishers.

Fingas, M. (2001). The Basics of Oil Spill Cleanup  Published, CRC Press.

Fingas, M. F. and C. E. Brown (1997). "Review of oil spill remote sensing." Spill Science & Technology Bulletin **4**(4): 199-208.

Fingas, M. F., C. E. Brown and J. V. Mullin (1998). A Comparison of the Utility of Airborne Oil Spill Remote Sensors and Satellite Sensors. Fifth Conference on Remote Sensing for Marine and Coastal Environments, Environmental Research Institute of Michigan.

Foody, G. M. (1995). "Using prior knowledge in artificial neural-network classification with a minimal training set." International Journal of Remote Sensing **16**(2): 301-312.

Foody, G. M. (2004). "Supervised image classification by MLP and RBF neural networks with and without an exhaustively defined set of classes." International Journal of Remote Sensing **25**(15): 3091-3104.

Foody, G. M., D. S. Boyd and M. E. J. Cutler (2003). "Predictive relations of tropical forest biomass from Landsat TM data and their transferability between regions." Remote Sensing of Environment **85**(4): 463-474.

Foody, G. M. and M. E. J. Cutler (2006). "Mapping the species richness and composition of tropical forests from remotely sensed data with neural networks." Ecological Modelling **195**(1-2): 37-42.

Friedman, K. S., W. G. Pichel, P. Clemente-Colo´n and X. Li (2002). "GoMEx-an experimental GIS system for the Gulf of Mexico Region using SAR and additional satellite and ancillary data." IGARSS'02 **6**: 3343- 3346.

Frizzelle, B. G. and A. Moody (2001). "Mapping continuous distributions of land cover: A comparison of maximum-likelihood estimation and artificial neural networks." Photogrammetric Engineering and Remote Sensing **67**(6): 693-705.

Frysinger, G., Asher, WE, Korenowski, GM, Barger, WR, Klusty, MA, Frew, NM, (1992). "Study of Ocean Slicks by Nonlinear Laser Processes in Second-Harmonic Generation." J Geophys Res: 5253.

Gade, M., W. Alpers, H. Huhnerfuss and V. Wismann (1997). Radar signatures of different oceanic surface films measured during the SIR-C/X-SAR missions.

Gens, R. (2008). "Oceanographic Applications of SAR Remote Sensing." GIScience and Rem Sens: 275.

Gong, P., R. Pu and B. Yu (2001). "Conifer species recognition: effects of data transformation." International Journal of Remote Sensing **22**(17): 3471-3481.

Goodenough, D. G., B. Guindon and P. M. Teillet (1980). Correction of synthetic aperture radar and multispectral scanner data sets. The Fifteenth International Symposium on Remote Sensing of Environment, USA.

Goodman, J. W. (1976). "Some fundamental properties of speckles." J. Opt. Soc. Am. **66**(11): 1145-1150.

Goodman, R. (1994). "Overview and future-trends in oil-spill remote-sensing." Spill Science & Technology Bulletin **1**(1): 11-21.

Goodman, R. H. (1989). Application of the technology in the remote sensing of oil slicks, Lodge, A.E. (Ed.), John Wiley & Sons Ltd.

Gradwohl, J. (1995). " Oil pollution. Archival version of the script of "Ocean Planet”." 2011, from http://seawifs.gsfc.nasa.gov/ocean_planet/html/peril_oil_pollution.html.

Gruner, K. R., T.; Smid, H. (1991). "A new sensor system for airborne measurements of maritime pollution and of hydrographic parameters." GeoJournal **24**(1): 103-117.

Hecht Nielsen, R. (1988). "Applications of counter propagation networks." Neural Networks **1**(2): 131-139.

Heigster, G. (1982). "Rank filters in digital image processing." Computer Graph. and Image Processing **19**: 148-164.

Henninger, D. L. and J. H. Carney (1983). Shuttle imaging Radar-A (SIR-A) data as a complement to Landsat Multi-spectral Scanner (MSS) data. International Geoscience and Remote Sensing Symposium (IGARSS'83), California.

Hielm, J. H. (1989). NIFO Comparative Trials, in The Remote Sensing of Oil Slicks, A.E.Lodge. United Kingdom, John Wiley and Sons, Chichester.

Hu, C., F. E. Müller-Karger, C. Taylor, D. Myhre, B. Murch, A. L. Odriozola and G. Godoy (2003). "MODIS detects oil spills in Lake Maracaibo, Venezuela." Eos **84**(33).

Hu, C. M., X. F. Li, W. G. Pichel and F. E. Muller-Karger (2009). "Detection of natural oil slicks in the NW Gulf of Mexico using MODIS imagery." Geophysical Research Letters **36**: -.

Huhnerfuss, H., W. Alpers, H. Dannhauer, M. Gade, P. A. Lange, V. Neumann and V. Wismann (1996). "Natural and man-made sea slicks in the North Sea investigated by a helicopter-borne 5-frequency radar scatterometer." International Journal of Remote Sensing **17**(8): 1567-1582.

Hühnerfuss, H., Alpers, W., Dannhauer, H., Gade, M., Lange, P.A., Neumann, V., Wismann,V. (1996). "Natural and Man-made Sea Slicks in the North Sea Investigated by a Helicopterborne 5-frequency Radar Scatterometer." Int. J. Remote Sensing **17**(8): 1567-1582.

Hurford, N. (1989). Review of remote sensing, in The Remote Sensing of Oil Slicks. An International Meeting organised by the Insititute of Petroleum, London, John Wiley.

Intera Technologies (1984). "Radar Surveillance in Support of the 1983 COATTF Oil Spill Trials." Environment Canada Report EE-51.

Jain, A. K., Mao, J., Mohiuddin, K.M., (1996). "Artificial neural networks: a tutorial." Comput. IEEE: 31-44.

Johnson, J. L. (1994). "Pulse-coupled neural nets - translation, rotation, scale, distortion, and intensity signal invariance for images." Applied Optics **33**(26): 6239-6253.

Johnson, J. L. and M. L. Padgett (1999). "PCNN models and applications." Ieee Transactions on Neural Networks **10**(3): 480-498.

Johnson, J. L., M. L. Padgett and O. Omidvar (1999). "Overview of pulse coupled neural network (PCNN) special issue." Ieee Transactions on Neural Networks **10**(3): 461-463.

Johnson, J. L. and D. Ritter (1993). "Observation of periodic-waves in a pulse-coupled neural-network." Optics Letters **18**(15): 1253-1255.

Jones, A. T., M. Thankappan, G. A. Logan, J. M. Kennard, C. J. Smith, A. K. Williams and G. M. Lawrence (2006). "Coral spawn and bathymetric slicks in Synthetic Aperture Radar (SAR) data from the Timor Sea, north-west Australia." International Journal of Remote Sensing **27**(10): 2063-2069.

Joshi, C., J. De Leeuw, A. K. Skidmore, I. C. van Duren and H. van Oosten (2006). "Remotely sensed estimation of forest canopy density: A comparison of the performance of four methods." International Journal of Applied Earth Observation and Geoinformation **8**(2): 84-95.

Karathanassi, V., K. Topouzelis, P. Pavlakis and D. Rokos (2006). International Journal of Remote Sensing **27**: 5235.

Karathanassi, V., K. Topouzelis, P. Pavlakis and D. Rokos (2006). "An object-oriented methodology to detect oil spills." International Journal of Remote Sensing **27**(23-24): 5235-5251.

Karathanassi, V., K. Topouzelis, P. Pavlakis and D. Rokos (2006). "An object-oriented methodology to detect oil spills." International Journal of Remote Sensing **27**(23): 5235-5251.

Karvonen, J. A. (2004). "Baltic Sea Ice SAR segmentation and classification using modified pulse-coupled neural networks." Ieee Transactions on Geoscience and Remote Sensing **42**(7): 1566-1574.

Kavzoglu, T. and P. M. Mather (2003). "The use of backpropagating artificial neural networks in land cover classification." International Journal of Remote Sensing **24**(23): 4907-4938.

Keramitsoglou, I., C. Cartalis and C. T. Kiranoudis (2006). "Automatic identification of oil spills on satellite images." Environmental Modelling and Software **21**(5): 640-652.

Kuruoglu, E. E. and J. Zerubia (2004). "Modeling SAR images with a generalization of the Rayleigh distribution." Ieee Transactions on Image Processing **13**(4): 527-533.

Landgrebe, D. A. (2003). Signal theory method, Wiley, New York.

Lee, J.-S. (1980). "Digit. Image Enhancement and Noise Filtering by Use of Local Statistics." IEEE Transac. on Pattern Analysis and Machine Interlligence **PAMI-2**(2): 165-168.

Lee, J. S., L. Jurkevich, P. Dewaele, P. Wambacq and A. Oosterlinck (1994). "Speckle filtering of synthetic aperture radar images: A review." Remote Sensing Reviews **8**(4): 313-340.

Leifer, I., W. J. Lehr, D. Simecek-Beatty, E. Bradley, R. Clark, P. Dennison, Y. Hu, S. Matheson, C. E. Jones, B. Holt, M. Reif, D. A. Roberts, J. Svejkovsky, G. Swayze and J. Wozencraft (2012). "State of the art satellite and airborne marine oil spill remote sensing: Application to the BP Deepwater Horizon oil spill." Remote Sensing of Environment **124**(0): 185-209.

Lek, S. and J. F. Guegan (1999). "Artificial neural networks as a tool in ecological modelling, an introduction." Ecological Modelling **120**(2-3): 65-73.

Li, Y. and J. Li (2010). "Oil spill detection from SAR intensity imagery using a marked point process." Remote Sensing of Environment **114**(7): 1590-1601.

Lichtenegger, J., G. Calabresi and A. Petrocchi (2000). "Detection and discrimination between oil spills and look-alike." XIX ISPRS Congress, XXXIII: 193.

Liu, A. K., C. Y. Peng and S. Y. Chang (1997). "Wavelet analysis of satellite images for coastal watch." IEEE Journal of Ocean Engineering **22**: 9−17.

Liu, P., C. Zhao, X. Li, M. He and W. Pichel (2010). "Identification of ocean oil spills in SAR imagery based on fuzzy logic algorithm." International Journal of Remote Sensing **31**(17-18): 4819-4833.

Liu, W. G., S. Gopal and C. E. Woodcock (2004). "Uncertainty and confidence in land cover classification using a hybird classifier approach." Photogrammetric Engineering and Remote Sensing **70**(8): 963-971.

Lopes, A., E. Nezry, R. Touzi and H. Laur (1993). "Structure detection and statistical adaptive speckle filtering in SAR images." International Journal of Remote Sensing **14**(9): 1735-1758.

Lopes, A., R. Touzi and E. Nezry (1990). "Adaptive speckle filters and scene heterogeneity." Ieee Transactions on Geoscience and Remote Sensing **28**(6): 992-1000.

Macklin, J. (1992). "The Imaging of Oil Slicks by Synthetic Aperture Radar." GEC Journal of Research **19**.

Marghany, M., A. P. Cracknell and M. Hashim (2009). "Modification of fractal algorithm for oil spill detection from RADARSAT-1 SAR data." International Journal of Applied Earth Observation and Geoinformation **11**(2): 96-102.

Marghany, M., M. Hashim and A. P. Cracknell (2007). "Fractal dimension algorithm for detecting oil spills using Radarsat-1 SAR." Lecture notes in computer science (LNCS): 1054−1062.

Mas, J. F. (2004). "Mapping land use/cover in a tropical coastal area using satellite sensor data, GIS and artificial neural networks." Estuarine Coastal and Shelf Science **59**(2): 219-230.

Mercier, G. and F. Girard-Ardhuin (2006). "Partially supervised oil-slick detection by SAR imagery using kernel expansion." Ieee Transactions on Geoscience and Remote Sensing **44**(10): 2839-2846.

Michelson, D. B., B. M. Liljeberg and P. Pilesjo (2000). "Comparison of algorithms for classifying Swedish landcover using Landsat TM and ERS-1 SAR data." Remote Sensing of Environment **71**(1): 1-15.

Migliaccio, M., Gambardella, A, Tranfaglia, A. (2007). "SAR Polarimetry to Observe Oil Spills." IEEE T Geosci Remote: 506.

Mueller, P. W. and A. M. Hoffer (1989). "Low-pass gnstial filtering of satellite radar data." Photogromm. Eng. Remote Senn: A97-897.

Mullins, O. C., M.-K. S. and Z. Y. (1992). "The electronic absorption edge of petroleum." Appl. Spectroscopy **46**(9): 1405-1411.

Mullins, O. C. and Z. Y. (1992). "First Observation of the Urback Tail in a multicomponent organic system." Appl. Spectroscopy **46**(2): 354-356.

Murthy, C. S., P. V. Raju and K. V. S. Badrinath (2003). "Classification of wheat crop with multi-temporal images: performance of maximum likelihood and artificial neural networks." International Journal of Remote Sensing **24**(23): 4871-4890.

Natural Resources Canada. (2014). Retrieved Aug 1, 2014, from http://ccrs.nrcan.gc.ca/resource/tutor/fundam/chapter5/28_e.php.

Neville, R., V. Thompson, K. Dagg and R. O'Neil (1979). An Analysis of Multispectral Line Scanner Imagery from Two Test Spills. First Workshop Sponsored by Working Group I of the Pilot Study on the Use of Remote Sensing for the Control of Marine Pollution, NATO Challenges of Modern Society.

Nezry, E., A. Lopes and R. Tmizi (1991). Detection of structural and textural features for SAR images filtering. IGARSS'91.

Nirchio, F., M. Sorgente, A. Giancaspro, W. Biamino, E. Parisato, R. Ravera and P. Trivero (2005). "Automatic detection of oil spills from SAR images." International Journal of Remote Sensing **26**(6): 1157-1174.

NOAA. (2014). "See Topic: Emergency Response, Responding to Oil Spills." Retrieved Aug 1, 2014, from http://response.restoration.noaa.gov.

Nunziata, F., Migliaccio, M, Sobieski, (2008). P. A BPM Two-Scale Contrast Model. IGARSS 2008.

O'Neil, R., Neville, RA, Thompson, V. T, (1983). "The Arctic Marine Oilspill Program (AMOP) Remote Sensing Study." Environment Canada Report EPS 4-EC-83e3.

Okamoto, K., Kobayashi, T, Masuko, H, Ochiai, S, Horie, H, Kumagai, H, (1996). "Results of Experiments Using Synthetic Aperture Radar Onboard the European Remote Sensing Satellite 1-4. Artificial Oil Pollution Detection." J Commun Res Lab **327**.

Osadchy, V. U., K. S. Shifrin and I. Y. Gurevich (1994). Remote sensing and measurement of the thickness of oil films on the sea surface using the reflectivity contrast.

Otremba, Z. and J. Piskozub (2001). "Modelling of the optical contrast of an oil film on a sea surface." Opt. Express **9**(8): 411-416.

Pal, M. and P. M. Mather (2005). "Support vector machines for classification in remote sensing." International Journal of Remote Sensing **26**(5): 1007-1011.

Paola, J. D. and R. A. Schowengerdt (1995). "A detailed comparison of back propagation neural-network and maximum-likelihood classifiers for urban land-use classification." Ieee Transactions on Geoscience and Remote Sensing **33**(4): 981-996.

Plaza, J., R. Pérez, A. Plaza, P. Martínez and D. Valencia (2001). Mapping oil spills on sea water using spectral mixture analysis of hyperspectral image data. SPIE.

Pu, R. L. and P. Gong (2004). "Determination of burnt scars using logistic regression and neural network techniques from a single post-fire Landsat 7 ETM+ image." Photogrammetric Engineering and Remote Sensing **70**(7): 841-850.

Ranganath, H. S. and G. Kuntimad (1999). "Object detection using pulse coupled neural networks." Ieee Transactions on Neural Networks **10**(3): 615-620.

Rio, J. N. and F. D. Lozano-García (2000). Remote Sensing of Environment **2**: 143.

Rybak, I. A., N. A. Shevtsova, L. N. Podladchikova and A. V. Golovan (1991). "A visual-cortex domain model and its use for visual information-processing." Neural Networks **4**(1): 3-13.

Rybak, I. A., N. A. Shevtsova and V. M. Sandler (1992). "The model of a neural network visual preprocessor." Neurocomputing **4**(1-2): 93-102.

S. Haykin (2008). Neural Networks and Learning Machines. New Jersey, Prentice Hall, Upper Saddle River.

Salisbury, J. W., D. M. Daria and F. F. Sabins (1993). "Thermal infrared remote-sensing of crude-oil slicks." Remote Sensing of Environment **45**(2): 225-231.

Samberg, A. (2005). Advanced oil pollution detection using an airborne hyperspectral lidar technology. Laser Radar Technology and Applications X. G. W. Kamerman. **5791:** 308-317.

Schalkoff, R. J. (1997). Artificial Neural Networks. New York, McGraw-Hill.

Seakem Oceanography (1988). "Remote sensing chronic oil discharges." Environment Canada Report EE-108 **46**.

Sekine, M. and Y. Mao (1990). Weibull Radar Clutter. London, U.K., IEE Press.

Seto, K. C. and W. G. Liu (2003). "Comparing ARTMAP neural network with the maximum-likelihood classifier for detecting urban change." Photogrammetric Engineering and Remote Sensing **69**(9): 981-990.

Sheng, Y. and Z. Xia (1996). International Geoscience and Remote Sensing Symposium IGARSS'96.

Shepherd, I. (2004). "Developing an operational oil-spill service in GMES." OCEANIDES **2**.

Shu, Y. M., J. Li, H. Yousif and G. Gomes (2010). "Dark-spot detection from SAR intensity imagery with spatial density thresholding for oil-spill monitoring." Remote Sensing of Environment **114**(9): 2026-2035.

Shupe, S. M. and S. E. Marsh (2004). "Cover- and density-based vegetation classifications of the sonoran desert using Landsat TM and ERS-1 SAR imagery." Remote Sensing of Environment **93**(1-2): 131-149.

Skoog, A. D. and J. J. LEARY (1991). Principals of instrumental analyses. USA, Saundress College.

Solberg, A., G. Storvik, R. Solberg and E. Volden (1999). "Automatic detection of oil spills in ERS SAR images." IEEE Transactions on Geocience and Remote Sensing **4**: 1916.

Solberg, A. H. S., C. Brekke and P. O. Husoy (2007). "Oil spill detection in Radarsat and Envisat SAR images." Ieee Transactions on Geoscience and Remote Sensing **45**(3): 746-755.

Solberg, R. and N. A. Theophilopoulos (1997). 4th International Conference on Remote Sensing for Marine and Coastal Environments.

Srivastava, H. and T. Singh (2010). "Assessment and development of algorithms to detection of oil spills using MODIS data." Journal of the Indian Society of Remote Sensing **38**(1): 161-167.

Svejkovsky, J., J. Muskat and J. Mullin (2009). "Adding a Multispectral Aerial System To the Oil Spill Response Arsenal." Sea Technology **50**(8): 17-+.

Taravat, A., D. Latini and F. Del Frate (2014). "Fully Automatic Dark-Spot Detection From SAR Imagery With the Combination of Nonadaptive Weibull Multiplicative Model and Pulse-Coupled Neural Networks." Geoscience and Remote Sensing, IEEE Transactions on **52**(5): 2427-2435.

Thankappan, M., Rollet,N.,Smith, C.J.H., Jones, A. , Logan, G., Kennard, J. (2007). Assessment of SAR ocean features using optical and marine survey data. Proceedings Envisat symposium, Switzerland 23–27 April.

Topouzelis, K., V. Karathanassi, P. Pavlakis and D. Rokos (2007). "Detection and discrimination between oil spills and look-alike phenomena through neural networks." Isprs Journal of Photogrammetry and Remote Sensing **62**(4): 264-270.

Topouzelis, K., V. Karathanassi, P. Pavlakis and D. Rokos (2008). "Dark formation detection using neural networks." International Journal of Remote Sensing **29**(16): 4705-4720.

Topouzelis, K., D. Stathakis and V. Karathanassi (2009). "Investigation of genetic algorithms contribution to feature selection for oil spill detection." International Journal of Remote Sensing **30**(3): 611-625.

Topouzelis, K. N. (2008). "Oil Spill Detection by SAR Images: Dark Formation Detection, Feature Extraction and Classification Algorithms." Sensors **8**(10): 6642-6659.

Touzi., R., A. Lopes and P. Bousquest (1988). "A statistical and geometrical edge detector for SAR images." IEEE Trans. Geosci. Remote Sens. **26**: 764-773.

Ulaby, F., Moore, RK, Fung, AK., (1989). Microwave Remote Sensing: Active and Passive, Artech House.

USGS. (2010). "http://hdds.usgs.gov/hdds/." HDDS  Retrieved December, 2014.

V. Vapnik (1998). Statistical Learning Theory. New York, Wiley.

Wadsworth, A., W. J. Looyen, R. Reuter and M. Petit (1992). "Aircraft experiments with visible and infrared-sensors." International Journal of Remote Sensing **13**(6-7): 1175-1199.

Waldemark, J., M. Millberg, T. Lindblad and K. Waldemark (2000). "Image analysis for airborne reconnaissance and missile applications." Pattern Recognition Letters **21**(3): 239-251.

Wang, X. and M. O.C. (1994). "Fluorescence life time studies of crude oils." Appl. Spectroscopy **48**(8): 977-984.

Wettle, M., P. J. Daniel, G. A. Logan and M. Thankappan (2009). "Assessing the effect of hydrocarbon oil type and thickness on a remote sensing signal: A sensitivity study based on the optical properties of two different oil types and the HYMAP and Quickbird sensors." Remote Sensing of Environment **113**(9): 2000-2010.

Wu, S. Y. and A. K. Liu (2003). "Towards an automated ocean feature detection, extraction and classification scheme for SAR imagery." International Journal of Remote Sensing **24**: 935−951.

Zell A., Mamier G., Michael Vogt, Niels Mache and S. D. Ralf Hubner, Kai-Uwe Herrmann, Tobias Soyez, Michael Schmalzl, Tilman Sommer, Artemis Hatzigeorgiou, Dietmar Posselt, Tobias Schreiner, Bernward Kett, Gianfranco Clemente, Jens Wiel, Jurgen Gatter (1995). "SNNS Stuttgart neural network simulator user manual." Inst. Parallel Distributed High Performance Syst., Univ. Stuttgart, Stuttgart, Germany.

Zhu, Z. L., L. M. Yang, S. V. Stehman and R. L. Czaplewski (2000). "Accuracy assessment for the US Geological Survey Regional Land-Cover Mapping Program: New York and New Jersey region." Photogrammetric Engineering and Remote Sensing **66**(12): 1425-1435.

Zielinski, O., Robbe, N. (2004). "Past and Future of Airborne Pollution Control." Interspill.

# Appendix

Taravat and Del Frate *EURASIP Journal on Advances in Signal Processing* 2012, **2012**:107
http://asp.eurasipjournals.com/content/2012/1/107

EURASIP Journal on Advances in Signal Processing
a SpringerOpen Journal

RESEARCH | Open Access

# Development of band ratioing algorithms and neural networks to detection of oil spills using Landsat ETM+ data

Alireza Taravat* and Fabio Del Frate

**Abstract**

Accurate knowledge of the spatial extents and distributions of an oil spill is very impor-tant for efficient response. This is because most petroleum products spread rapidly on the water surface when released into the ocean, with the majority of the affected area becoming covered by very thin sheets. This article presents a study for examining the feasibility of Landsat ETM+ images in order to detect oil spills pollutions. The Landsat ETM+ images for 1st, 10th, 17th May 2010 were used to study the oil spill in Gulf of Mexico. In this article, an attempt has been made to perform ratio operations to enhance the feature. The study concluded that the bands difference between 660 and 560 nm, division at 660 and 560 and division at 825 and 560 nm, normalized by 480 nm provide the best result. Multilayer perceptron neural network classifier is used in order to perform a pixel-based supervised classification. The result indicates the potential of Landsat ETM+ data in oil spill detection. The promising results achieved encourage a further analysis of the potential of the optical oil spill detection approach.

**Keywords:** oil spills, multi-spectral, Landsat ETM+, neural networks, remote sensing

## Introduction

Oil spills are causing serious damage to marine and coastal ecosystem. It is estimated that 0.25% of world oil production ends up in the ocean. However, the main contribution of oil pollution originating from transportation activities still originates not from ship accidents, but from routine ship operations like tank washing and engine effluent discharges [1]. Timely and accurate detection of oil slicks help to monitor oil spills and manage coastal resources. The detection of oil spills can efficiently be improved by the use of satellite images which are characterized by suitable special resolution for this purpose [2]. Remote sensing techniques include radar, microwave, infrared, and visible sensors [3]. However, most of oil spills are estimated by Synthetic Aperture Radar (SAR) data [3], which are limited by revisit frequency and coverage.

The exploitation of optical satellite images allows for large areas monitoring and remote zones control, providing more frequent information if compared to the use of SAR images only. Moreover, the possibility of detecting oil spills by optical satellite sensors has been demonstrated [4-6].

It is the optical properties and chemistry (OH, CN, and CH bonds) of oil that makes it detectable by remote sensing techniques in marine environment [1].

From an optical perspective, the effect of an oil layer on water can be described by two main processes:

(1) The specular reflection of light off the surface of the oil layer, and more importantly
(2) The absorption of up-welling light from the water column by the overlying oil layer [5,7].

The contrast of sea areas polluted by oil depends on the form of the oil substance. It is negative, positive, or zero with film, and only positive with suspensions [5].

In the visible region of the electromagnetic spectrum, oil has a higher surface reflectance than water [8]. So, reliable identification of oil spill by remote sensing is only possible if the difference in measured radiance between an oil covered and a clean surface is greater than the background variability.

* Correspondence: art23130@gmail.com
Information, Systems and Production Department, Tor Vergata University, 00133 Rome, Italy

In the literature, the two main methods of statistical and neural network-based classification have been proposed for detecting oil spills. Solberg et al. and Topouzelis et al. [9-11] detected oil slicks from SAR images by combining a statistical model with a rule-based approach. Del Frate et al. [12] detected oil spills based on a multilayer perceptron (MLP) neural network using ERS images. However, to the best of the authors' knowledge, automatic oil spill detection by neural networks in optical data is not reported in the literature. We observe that in the case of optical data, where a spectral signature for each pixel is available, a pixel-based algorithm can be designed. This is not possible with SAR where the detection is usually implemented starting from a single-band acquisition. This means that a preliminary image segmentation is necessary to extract the dark spot and an object classification to distinguish between actual oil spill and look-alikes is then applied.

In this article, an attempt has been made to perform ratio operations to enhance the oil spots, extracting the features by an MLP neural network, and demonstrate the potential of Landsat ETM+ data in oil spill monitoring in the Gulf of Mexico based on the optical properties of oil slicks detected by neural network.

## Methods

Landsat ETM+ images for the area from 29 N to 27 N and 87 W to 90 W for Gulf of Mexico, acquired in 1st, 10th, and 17th May 2010 were used to study the previously known oil spills [13]. Landsat ETM+ has eight bands which may be combined in various ways by assigning one band to each of the three visible channels: red, green, and blue, to create a false color image.

Subimages containing oil spills were extracted using the Area of Interest tool of ENVI (Environment for Visualizing Images) software to spare disk space and to make classification and image interpretation more expedient and focused.

The data were then projected in Geo (lat/long) projection and WGS84 datum. Further the image was exported into *.TIFF format for further analysis (slick detection, feature extraction, spectral enhancement, and filtering).

The stripes in Landsat ETM+ data (caused by the Scan Line Corrector in the ETM+ instrument failed On May 31, 2003) have been removed by a developed model which identifies stripe positions based on edge-detection and applies line-tracing algorithms. Pixels not affected by striping are used to construct spline functions describing spatial gray level distributions of an image. Detected stripes are corrected by replacing the pixels with more reasonable gray values computed from constructed spline functions.

To produce optimal contrast and variation for color composition of those individual bands, ratio operations were applied to the images with various band combinations. For the classification test, MLPs have been considered, which have been found to have the best suited topology for pixel level classifications [14].

These are feedforward networks, where the input flows only in one direction to the output, and each neuron of a layer is connected to all neurons of the successive layer but has no feedback to neurons in the previous layers

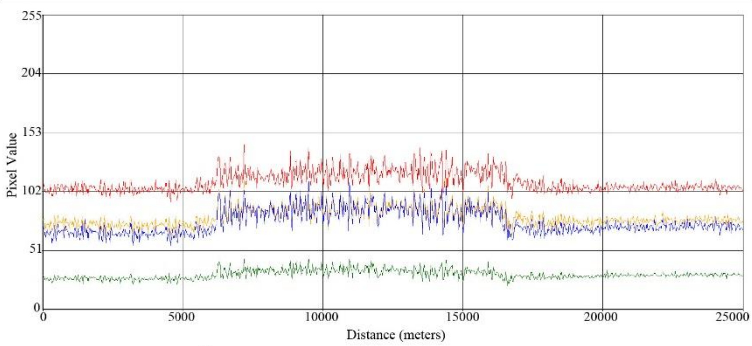


**Figure 1 Profile along transect A (1st May 2010, Original Image).**

[14]. The individual neuron is the elemental building block of each layer, and it is mainly characterized by its activation function. An activation function, $\phi(v)$, defines the output of a neuron in terms of the linear combination of inputs, v. There are different kinds of activation functions: the threshold function, the piecewise-linear function, and the sigmoid function [14]. The most commonly used is the sigmoid function. An example of the sigmoid function is the logistic function, defined by Equation (2) where $a > 0$ is the slope parameter;

$$\phi(V) = \frac{1}{(1 + e^{\ av})} \qquad (1)$$

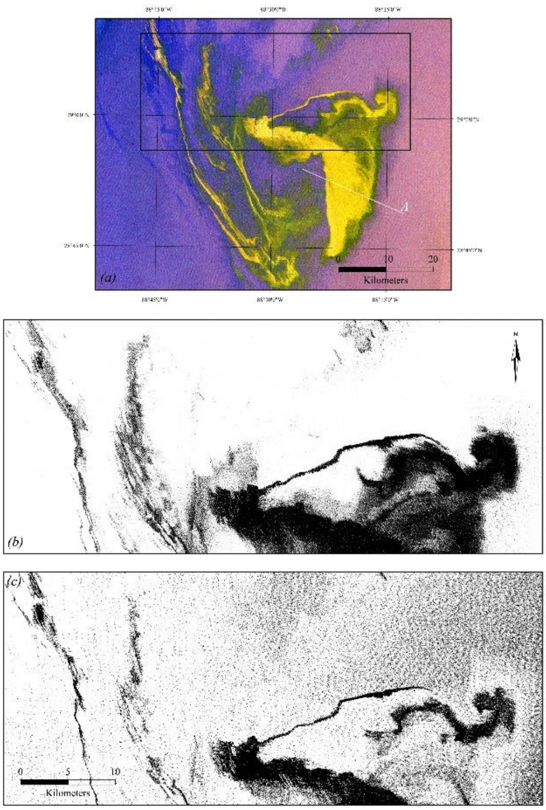


**Figure 2 Band ratioing and classification results. (a)** Color composite of band ratioing for Landsat ETM+ data collected May 1st, 2010, in the Gulf of Mexico. **(b)** NN classification result of image **(a)**. **(c)** Result of thresholding method applied on image **(a)**.

The activation functions defined in Equation. (1) range from 0 to +1. It is sometimes desirable to have the activation function range from -1 to +1, in which case the activation function assumes an anti-symmetric form with respect to the origin. For the corresponding form of a sigmoid function, we may use the hyperbolic tangent function, defined by

$$C(V) = \tanh(V) \qquad (2)$$

Allowing an activation function of the sigmoid type to assume negative values as prescribed by Equation (2) has analytic benefits [14]. In our study, the use of hyperbolic tangent function provided better results than those obtained with the sigmoid function of Equation (1).

The net was trained using the back propagation algorithm, which uses a gradient search technique and iteratively adjusts the weight coefficients in the network to minimize an error function equal to the mean square difference between the desired and the actual net output [14].

## Result and discussion

The earlier studies carried out by Hu et al. [6] reported that the shorter wavelengths were more sensitive to optical signature of oil; therefore, Landsat ETM+ data in spectral bands B1 (480 nm), B2 (560 nm), B3 (660 nm), B4 (825 nm) have been used in this study [6].

As it is already mentioned, the refractive index of oil is greater than that of sea water, but there are possibilities of masking the data, while performing atmospheric corrections [15]. Therefore, in order to identify the oil spill area, just geometrically corrected data have been used.

To identify the spectral signature of oil spill, a spectral profile along transect ($A$) was plotted. The visual interpretation in individual bands did not produce significant signature of oil (Figure 1). In order to identify the specific signatures of oil spill by enhancing the contrast, band ratio operations were performed. The ratios were computed using 65 different combinations of bands.

To determine which combination showed the best contrast between the surface slick and surrounding clear ocean water, we extracted data along several transect lines for each band combination [4]. The ratio combinations that showed excellent contrast (about -0.2, defined as $(R_s - R_c)/R_c$ where "$R_s$" and "$R_c$" stand for slick luminance and clear water luminance, whereas the contrast of the original bands are about 0.07) and the most significant for retrieving oil spill are given below:

$$RS1 = (B4/B2)/B1$$

$$RS2 = (B3/B2)/B1$$

$$RS3 = (B3/B2)/B1$$

These combinations can be interpreted based on spectral signature of oil and water background in landsat ETM+. Oil and water background show steadily increasing reflectance spectrum between wavelength 475-675 nm, while they have different level of absorption in 675-800 nm, thus, information of oil spill could be extracted by band ratio of B4/B2 and B3/B2 [8]. There is a decrease in water background reflection from 550-750 nm; so to get some information on background the

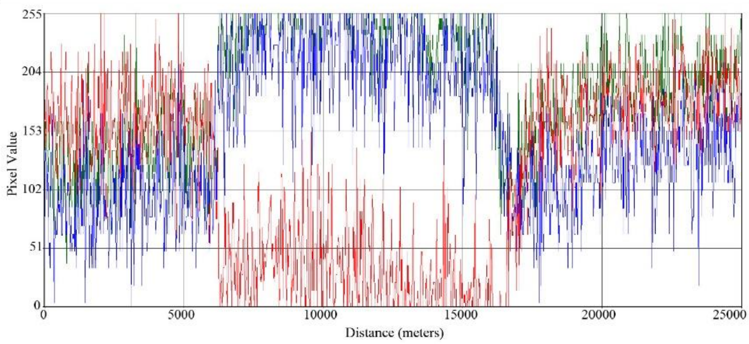


**Figure 3** Profile along transect A (1st May 2010, Image output of band rationing operation).

difference of bands 3 and 2 can be applied. Additionally, the difference between bands 3 and 2 is useful to visualize the data in RGB format.

The shorter wavelength at blue (B1) is normally found to be contaminated with the signatures of biogenic materials. Therefore, for removing biogenic materials

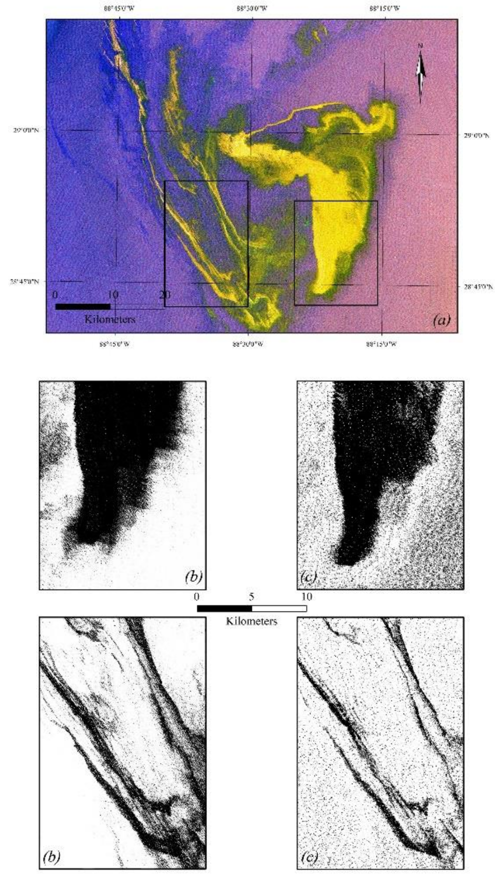


**Figure 4 Band ratioing and classification results.** **(a)** Subimages of color composite of band ratioing for Landsat ETM+ data collected May 17th, 2010, in the Gulf of Mexico. **(b)** Subimages of color composite of band ratioing for Landsat ETM+ data collected May 10th, 2010, in the Gulf of Mexico, used for training the NN. **(c)** NN classification result of image **(a)**. **(d)** NN classification result of image **(b)**.

effects, the results were normalized with respect to 480 nm [15].

Color-composite images can be created by assigning RS1, RS2, and RS3 values, computed from the Landsat ETM+ data into red, green, and blue channels, respectively. The algorithm developed for oil spill was applied for the data of Gulf of Mexico on $1^{st}$, $10^{th}$, and $17^{th}$ May 2010.

Figure 2a presents the ratio image of Gulf of Mexico at May $1^{st}$, 2010. The oil spill signatures were very well identified along transect A (Figure 3).

When thick oil spots are present in clear, deep ocean water, strong yellow and orange tones in the color-composite image are indicative of areas containing them (Figure 2a). These tones result from the relatively higher values of RS1 and RS2 and relatively lower values for RS3 for oil spot as compared to clear, deep ocean water (Figure 3). Blue and purple tones indicate the absence of oil or insufficient quantity or thickness to cause spectral differences associated with oil in spectral bands.

Once the best ratios to discriminate between the pixels contain oil and clear water have been determined, an MLP algorithm for pixel classification has been designed. The result has been compared with the result of Multiband thresholding algorithm which is the combined result of AND operation for thresholded RS1 and RS3 bands.

Several attempts have been made to properly select the number of units to be considered in the hidden layers. The pixels for train/test the net are 80,152 pixels which have been extracted from one image ($10^{th}$ May 2010, Gulf of Mexico) (Figure 4b). The training sets contain 60% and the test sets contain 40% of all pixels which are not belonging to the training set. Pixel selection for train/test set has been done randomly and repeated six times; so the presented results of root mean square error (RMSE) errors are the average of these repetitions for each topology (Figure 5). The topology 3-4-2 has been finally chosen for its good performance in terms of classification accuracy, RMSE, and training time. The number of about 10,000 training cycles was sufficient to get the network learned. The described topology is reported in Figure 6. The input of the net consists of RS1, RS2, and RS3 bands and the output providing classified pixels in terms of oil spill or others and one MLP NNs has been used for classifying all images.

Accuracy assessment has been carried out considering the other two images ($1^{st}$ May 2010, $17^{th}$ May 2010). For both of them 5,000 pixels have randomly been selected and then labeling made by visual interpretation. As it has been shown in Table 1, the overall rate of the accurately classified pixels in image collected at $1^{st}$ May 2010 is 97%, whereas the accuracy of the same image segmented by thresholding method is 43%. Also in the second test image ($17^{th}$ May 2010) the performance of the neural classification is satisfactory with an overall accuracy of 95%.

In Figures 2b and 7b, some subareas of image collected at May $1^{st}$ 2010 have been shown, where the better advantage of NN can clearly be observed based on visual interpretation.

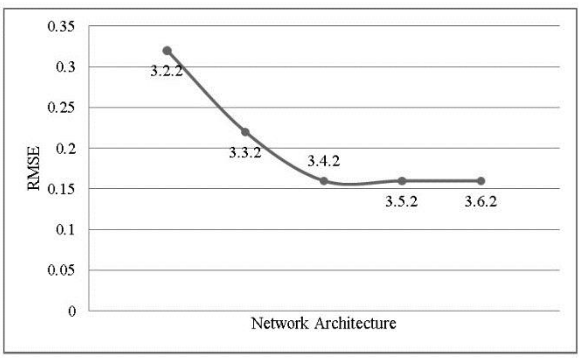


**Figure 5** RMSE errors for different NN topologies.

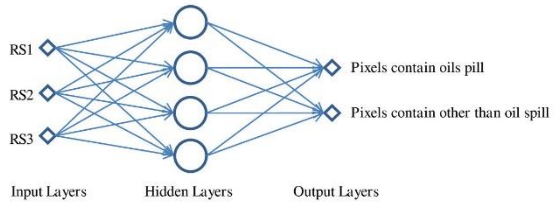


**Figure 6** Feedforward topology for an NN.

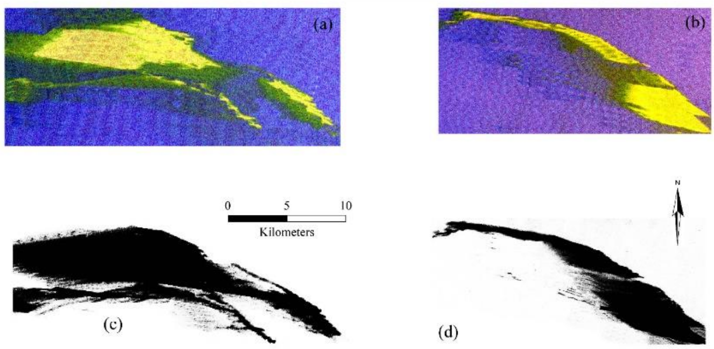


**Figure 7 Band ratioing and classification results. (a)** Color composite of band ratioing for Landsat ETM+ data collected May 1st 2010, in the Gulf of Mexico. **(b)** NN classification result of image **(a)**. **(c)** Result of thresholding method applied on image **(a)**.

**Table 1 The error matrix of classified images shows the accuracy assessment**

| Image | Well classified Pixels | Misclassified pixels | Accuracy % |
|---|---|---|---|
| ETM+ (1st, May 2010) | 4850 | 150 | 97% |
| ETM+ (10th, May 2010) | 4950 | 50 | 99% |
| ETM+ (17th, May 2010) | 4750 | 250 | 95% |

The neural network simulator (SNNS) developed at the University of Stuttgart, Stuttgart, Germany, has been used for the classification algorithm implementation and proved to be a high level and reliable software package [16].

## Conclusion

This article presents and demonstrates the potential of Landsat ETM+ to automatically detect and extract oil spill in marine environment. The band ratioing approach used in this study was found to work well for the identification of potential hydrocarbon contaminants in water. It has been observed that the bands difference between bands 3 (660 nm) and 2 (560 nm), division ratio of bands 3 (660 nm) and 2 (560 nm) and division ratio of bands 4 (825 nm) and 2 (560 nm) normalized by band 1 (480 nm) were most suitable to retrieve oil spill.

MLPs with different topologies have been applied to a set of features describing oil spill characteristics in order to perform a supervised classification. Best performances are obtained using an MLP neural network with 3:4:2 topology trained by the standard backpropagation algorithm. This algorithm has been designed for Landsat ETM + data but it can be applied on different multispectral data (WorldView2, Spot, etc.).

The largest challenge in detection of oil spills in SAR images is accurate discrimination between oil spills and look-alikes. Natural films cannot always be properly distinguished from oil spills based on a SAR image alone but additional information can be derived from optical sensors. Future oil spill systems should incorporate oil spill information from multisensory studies.

**Competing interests**

The authors declare that they have no competing interests.

Received: 11 July 2011 Accepted: 10 May 2012 Published: 10 May 2012

**References**

1. BE Omitz, MA Champ, *Oil Spills First Principles:Prevention and Best Response* (Elsevier, Amsterdam, 2002), p. 653
2. KA Kvenvolden, CK Cooper, Natural seepage of crude oil into the marine environment. Geo-Marine Lett. **23**(3), 140–146 (2003). doi:10.1007/s00367-003-0135-0
3. C Brekke, AHS Solberg, Oil spill detection by satellite remote sensing. Remote Sens Environ. **95**(1), 1–13 (2005). doi:10.1016/j.rse.2004.11.015
4. C Hu, X Li, WG Pichel, E Muller-Kerger, Detection of natural oil slicks in the NW Gulf of Mexico using MODIS imagery. Geophys Res Lett. **36**(1), L01604 (2009)
5. Z Otremba, J Piskozub, Modelling of the optical contrast of an oil film on a sea surface. Opt Exp. **9**(8), 411–416 (2001). doi:10.1364/OE.9.000411
6. C Hu., *et al*, MODIS detects oil spills in Lake Maracaibo, Venezuela. Eos Trans AGU. **84**(33), 313–317 (2003)
7. M Wettle., *et al*, Assessing the effect of hydrocarbon oil type and thickness on a remote sensing signal: a sensitivity study based on the optical properties of two different oil types and the HYMAP and Quickbird sensors. Remote Sens Environ. 11**3**(9), 2000–2010 (2009). doi:10.1016/j.rse.2009.05.010
8. J Svejkovsky, J Muskat, J Mullin, Adding a multispectral aerial system to the oil spill response Arsenal. Sea Technol. **50**(8), 17 (2009)
9. AHS Solberg, C Brekke, PO Husoy, Oil spill detection in Radarsat and Envisat SAR images. IEEE Trans Geosci Remote Sens. **45**(3), 746–755 (2007)
10. AHS Solberg, ST Dokken, R Solberg, Automatic detection of oil spills in Envisat, Radarsat and ERS SAR images. Geoscience and Remote Sensing Symposium, IGARSS '03. Proceeding. IEEE International (2003)
11. KN Topouzelis, Oil spill detection by SAR images: dark formation detection, feature extraction and classification algorithms. Sensors. **8**(10), 6642–6659 (2008). doi:10.3390/s8106642
12. F Del Frate., *et al*, Neural networks for oil spill detection using ERS-SAR data. IEEE Trans Geosci Remote Sens. **38**(5), 2282–2287 (2000). doi:10.1109/36.868885
13. USGS, http://hdds.usgs.gov/hdds/ (2010). HDDS 2010
14. CM Bishop, *Neural Networks for Pattern Recognition* (Oxford University Press, Oxford, 1995)
15. H Srivastava, T Singh, Assessment and development of algorithms to detection of oil spills using MODIS data. J Indian Soc Remote Sens. **38**(1), 161–167 (2010). doi:10.1007/s12524-010-0007-9
16. A Zell, *et al*, *SNNS Stuttgart neural network simulator user manual*, (Inst. Parallel Distributed High Performance Syst., Univ. Stuttgart, Stuttgart, Germany, 1995)

doi:10.1186/1687-6180-2012-107

**Cite this article as:** Taravat and Del Frate: **Development of band ratioing algorithms and neural networks to detection of oil spills using Landsat ETM+ data.** *EURASIP Journal on Advances in Signal Processing* 2012 2012:107.

# Fully Automatic Dark-Spot Detection From SAR Imagery With the Combination of Nonadaptive Weibull Multiplicative Model and Pulse-Coupled Neural Networks

Alireza Taravat, Daniele Latini, and Fabio Del Frate, *Senior Member, IEEE*

***Abstract*—Dark-spot detection is a critical step in oil-spill detection. In this paper, a novel approach for automated dark-spot detection using synthetic aperture radar imagery is presented. A new approach from the combination of Weibull multiplicative model (WMM) and pulse-coupled neural network (PCNN) techniques is proposed to differentiate between the dark spots and the background. First, the filter created based on WMM is applied to each subimage. Second, the subimage is segmented by PCNN techniques. As the last step, a very simple filtering process is used to eliminate the false targets. The proposed approach was tested on 60 Envisat and ERS2 images which contained dark spots. The same parameters were used in all tests. For the overall data set, an average accuracy of 93.66% was obtained. The average computational time for dark-spot detection with a 512 × 512 image is about 7 s using IDL software, which is the fastest one in this field at present. Our experimental results demonstrate that the proposed approach is very fast, robust, and effective. The proposed approach can be applied on any kind of synthetic aperture radar imagery.**

***Index Terms*—Dark spot detection, oil spill detection, pulse coupled neural networks, SAR image processing, synthetic aperture radar (SAR), Weibull multiplicative model.**

## I. INTRODUCTION

As A major aspect of marine pollution, oil release into the sea has become a common phenomenon, and it can have serious biological and economic impacts [1]. Cargo ships and pipelines submerged in the marine environment carry huge amounts of petroleum across the open ocean and in coastal areas [2]. Normally, small-scale release of oil into the sea is ascribed as "slicks," while large-scale ones are called "spills" [3].

Accurate detection and forecast of oil spill in a timely manner would be beneficial to resource management for monitoring and conservation of the marine environment. It is one of the most important applications for operational oceanography. In recent years, remote sensing instruments have become one of the most effective methods in marine oil-spill detection. Moreover, it has been demonstrated to be a tool that offers a nondestructive investigation method and has a significant added value to traditional methods.

A number of remote sensing systems are available for detecting oil slicks, namely, passive (i.e., optical sensors, infrared/ultraviolet systems, and microwave radiometers) and active (i.e., laser fluorosensors and radar systems) [4], [5]. Among them, synthetic aperture radar (SAR) can provide valuable synoptic information about the position and size of the oil spill due to its wide area coverage and day/night and all-weather capabilities [5], [6].

Detection of oil spills from SAR imagery can be divided into three steps: 1) dark feature detection; 2) computation and extraction of physical and geometrical features characterizing the dark feature; and 3) accurate discrimination between oil spills and look-alikes such as ice, internal waves, kelp beds, natural organics, jellyfish, algae, threshold wind speed areas (wind speed < 3 m/s), and rain cells [5], [7], [8]. These procedures can be done manually or automatically [9]–[13].

As a preliminary task, dark-spot detection is a critical step prior to feature information extraction and classification. Furthermore, the accuracies of feature extraction and classification greatly rely on the accuracy of dark-spot detection. In addition, dark-spot detection is traditionally the most time-consuming of the three steps. Thus, an efficient and effective dark-spot detection approach is essential for developing automated oil-spill detection systems [14].

In the literature, various types of models have been proposed for detecting dark spots, namely, manual selection by cropping a broader area containing the dark formation [13], [15], threshold algorithms (adapted or not) [9], [12], [16]–[18], marked point and spatial density thresholding methods [14], [19], wavelets [20]–[22], fractal dimension estimation [23][24], support vector machines [25], and neural networks [26]–[28].

In the present paper, an attempt has been made to develop a fast, robust, and effective automated approach that is adequate for practical oil-spill monitoring. A new approach from the combination of Weibull multiplicative model (WMM) and pulse-coupled neural network (PCNN) techniques is proposed for achieving this goal.

The PCNN segmentation capabilities have been already proofed in marine environment [29], but based on the authors' knowledge, it has not been tested for dark-spot detection. Apart

Manuscript received July 19, 2012; revised December 19, 2012 and February 26, 2013; accepted April 23, 2013. Date of publication July 12, 2013; date of current version March 3, 2014.

The authors are with Tor Vergata University, 00173 Rome, Italy (e-mail: art23130@gmail.com; latini.daniele@gmail.com; delfrate@disp.uniroma2.it).

Color versions of one or more of the figures in this paper are available online at http://ieeexplore.ieee.org.

Digital Object Identifier 10.1109/TGRS.2013.2261076

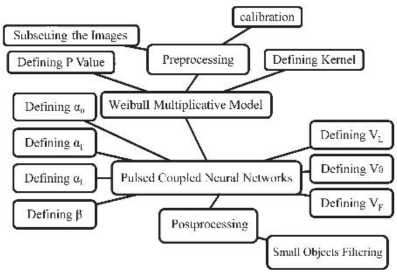


Fig. 1. Overview of the proposed approach.

from using the common PCNN algorithm, this approach further employs a WMM to enhance the separability between the dark spots and the background. The idea is to separate the detection process into two main steps, namely, WMM enhancement and PCNN segmentation. To highlight the main contribution of this paper, we refer to the whole approach as "WMM" and "PCNN."

This paper is organized in four sections. Section II contains a description of the principles behind the proposed approach. In Section III, a detailed description of each step in the dark-spot detection procedures and the experimental results obtained using Envisat and ERS2 images are analyzed and explained. The conclusion follows in Section IV.

## II. Methods

Two main difficulties occur when using the automatic model for dark-spot detection: 1) the speckles in SAR imagery due to the constructive and destructive interferences of the reflections from surfaces of objects and 2) the contrast between the dark spots and the background can vary, depending on the type of dark spot, the local sea state, and the resolution and incidence angle of the SAR imagery [30]–[33].

A new approach for dark-spot detection is proposed based on the principles described in the following discussion. In this approach, the combination of WMM and PCNN techniques is proposed to differentiate between the dark spots and the background.

First, the filter created based on WMM is applied to each subimage which contains dark spots. Second, the subimages are segmented by PCNN techniques. As the last step, a very simple filtering process is used to eliminate the false targets. A flowchart of the procedures is illustrated in Fig. 1.

### A. Nonadaptive WMM

The first step of dark feature detection is applying a filter. Filtering an original SAR image has two aims: first, to remove image speckles and, second, to smooth the image values [5], [30].

The first step toward removing speckle noise is to understand its statistical properties. Traditionally, invoking the central limit theorem, it has been assumed that the real and imaginary parts of the received wave follow Gaussian distribution, which, in turn, leads to the Rayleigh distribution [34]. Another popular model is the Weibull distribution which has shown a high degree of success in modeling urban scenes and sea clutter (most of the models were suggested based on empirical observations and were case specific) [35]–[37].

In this paper, we have used WMM (with the assumption that the amplitude or the intensity image has the Weibull distribution) in order to remove speckle and to enhance the contrast between the dark spot and the background [38]. In SAR images, the texture is embedded in the speckle, which is originated by the coherent reflection of waves in a rough surface. WMM applies a nonlinear transformation to generate the texture image from the original speckled image. The extraction of the texture image from the Weibull-distributed SAR image employs the local estimation of the scale and form parameters of the Weibull distribution [37].

The Weibull-distributed random variable $x$ with form parameter $\gamma_x > 0$ and scale parameter $\beta_x > 0$ has a probability density function given by

$$f(x) = \frac{\gamma_x}{\beta_x}\left(\frac{x}{\beta_x}\right)^{\gamma_x - 1} \quad exp\left[-\left(\frac{x}{\beta_x}\right)^{\gamma_x}\right].$$

The $m$-order moment can be expressed as

$$E[x^m] = m\beta_x^m \frac{\Gamma\left(\frac{m}{\gamma_x}\right)}{\gamma_x}.$$

For $\gamma_x = 2$, the Weibull distribution becomes a Rayleigh distribution, and for $\gamma_x = 1$, it becomes an exponential distribution. It can be shown that $x^a$, with $a > 0$, is also Weibull distributed. If $z = x^a$, with form and scale parameters given by $\gamma_z = \gamma_x/a$ and $\beta_z = \beta_x^a$, it follows that

$$f(z) = \frac{\gamma_z}{\beta}\left(\frac{z}{\beta_z}\right)^{\gamma_z - 1} \quad exp\left[-\left(\frac{z}{\beta_z}\right)^{\gamma_z}\right].$$

Consider $b$, with $a > b > 0$ in such a way that

$$z = x^a = x^b x^{a-b} = \frac{x^b}{E[x^b]} E[x^b] x^{a-b} = st$$

where $(s)$ is the speckle with unitary mean and $(t)$ is the texture of the Weibull-distributed variable $(z)$. $z$ is the variable for the SAR image

$$s = \frac{x^b}{E[x^b]} \qquad t = x^{a-b} E[x^b].$$

In this form, it is possible to express $z$ as a multiplication of $s$ by $t$, where $s$ is the speckle and $t$ is the texture of the Weibull-distributed variable $z$. Texture $t$ has Weibull distribution with form and scale parameter given, respectively, by

$$\gamma_t = \gamma_x/(a-b) \qquad \beta_t = \beta_x^{a-b} E[x^b]$$

and the speckle has Weibull distribution with form and scale parameter given, respectively, by

$$\gamma_s = \frac{\gamma_x}{b} \qquad \beta_s = \frac{\beta_x^b}{E[x^b]}.$$

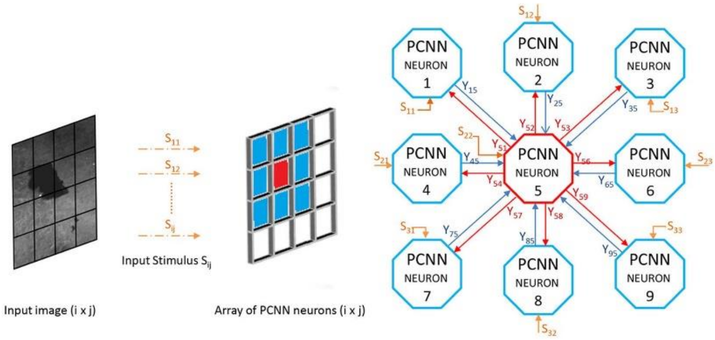


Fig. 2. General scheme of interneuron communication of the PCNN model.

Let

$$p = \frac{b}{a}, \qquad 0 \leq p < 1.$$

Then

$$t = x^{a-b}E[x^b] = x^{a(p-1)}E[x^{ap}] = z^{(1-p)}E[z^p]$$

using $p$-order moment equation $E[z^p]$

$$t = p\beta_z^p \frac{\Gamma\left(\frac{p}{\gamma_z}\right) z^{1-p}}{\gamma_z}$$

where $t$ can be considered as the filtered image and the factor $0 \leq p < 1$ gives the filtering intensity. If $p$ is close to 1, then $a \approx b$, and texture $t$ is constant (high filtering). If $p$ is close to 0, then $a \gg b$, and $t \approx z$ (low filtering). For each pixel in the Weibull-distributed image, $\gamma z$ and $\beta z$ are locally estimated in a window of dimension $N \times N$ surrounding the pixel to be filtered.

### *B. PCNNs*

The PCNN theory is based on the early work of Eckhorn in the 1990s [39]. The PCNN model is inspired by biological studies on the mechanism underlying the visual cortex of the small mammals. This specific region of the brain, which is a part of the completed mammalian visual system, receives information from the eyes and converts it into a stream of pulses. The receptors are interconnected; when one receives the information, it alters the behavior of other surrounding receptors.

PCNNs have been proved to be very useful for different fields of image processing and image recognition [40], [41], with promising results in applications regarding object extractions, edge detection, texture analysis [42]–[44], multichannel image analysis [45], image fusion [46], and target recognition [47]. This model has the capability to extract (in an automatic way) essential information from an image, such as edges and textures. Moreover, it has the ability to isolate objects with very similar and contiguous values.

The PCNN is a single-layer, 2-D, and laterally connected network of integrate-and-fire neurons, with a $1:1$ correspondence between the image pixels and the network neurons. They receive the input directly from the original image, forming the binary pulsing results. The PCNN is categorized in the unsupervised neural network group, so it does not need any training stage. The output images at different iterations typically represent some segment or edge information of the input image. In Fig. 2, a general scheme of interneuron communication has been shown. In this model, the network has the same dimension as the processed product, and every neuron corresponds to a pixel, from which it receives an input stimulus $(S_{ij})$. In this paper, $S_{ij}$ corresponds to the sigma naught value $\sigma 0$ (backscattering values). This is the value that, after radiometric calibration, is obtained from the digital number representing the strength of the radar pulse returned to the antenna.

The Eckhorn's PCNN neuron model is shown in Fig. 3. It consists of an input part, a linking part, and a pulse generator. The neuron receives the input signals from feeding and linking inputs. The feeding input is the primary input from the neuron's receptive area which receives the input stimulus from the considered pixel as well as the local stimulus related to its surrounding pixels. The linking input is the secondary input and receives only local stimulus. The difference between these inputs is that the feeding connections have a slower characteristic response time constant than the linking connections.

The input compartment composed by both the feeding and linking inputs can be defined by the following expressions:

$$F_{ij}[n] = e^{-\alpha F}.F_{ij}[n-1] + S_{ij} + V_F \sum_{kl} M_{ijkl}Y_{kl}[n-1]$$
$$L_{ij}[n] = e^{-\alpha_L}.L_{ij}[n-1] + V_L \sum_{kl} W_{ijkl}Y_{kl}[n-1]$$

where $S_{ij}$ is the input stimulus which is equal to the value of the pixel $(ij)$. The neuron $(ij)$, belonging to a 2-D grid of PCNN neurons, takes $S_{ij}$ as input through the feeding branch. The

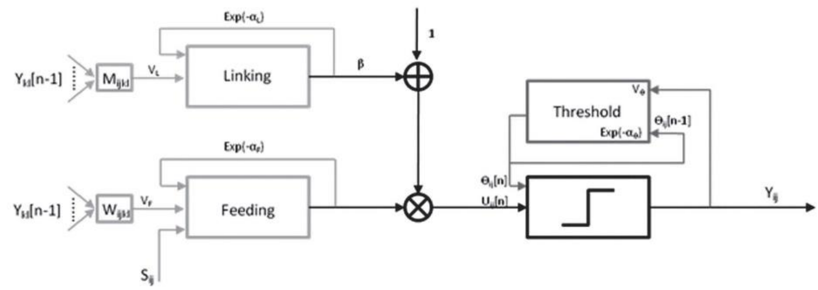


Fig. 3. Schematic representation of a PCNN neuron.

compartment keeps memory of the previous state through the terms $F_{ij}[n-1]$ and $L_{ij}[n-1]$, where both of them decay in time by the exponent terms $\alpha F$ and $\alpha L$. Generally, $\alpha F < \alpha L$, conferring a slower response time to the feeding input and hence more influence than the linking input.

Each of these neurons communicates with surrounding neurons $(kl)$ through the matrix of synaptic weights given by $M$ and $W$, respectively. $M$ and $W$ traditionally follow very symmetric patterns and refer to the Gaussian weight functions with the distance. $Y$ indicates the output of the surrounding neurons from a previous iteration $[n-1]$. $V_F$ and $V_L$ are normalizing parameters which are used to scale the resultant correlations of the surrounding outputs to prevent saturation. These two control the incidence of the neuron's receptive area.

The states of the feeding and linking inputs are combined into the linking compartment to create the internal state of the neuron $U$. The combination is controlled by the linking strength $\beta$.

The internal activity is given by

$$U_{ij}[n] = F_{ij}[n]\{1 + \beta L_{ij}[n]\}.$$

In the pulse generator compartment, the internal state of the neuron is compared to a dynamic threshold $\Theta$ to produce the output $Y$ by

$$Y_{ji}[n] = \begin{cases} 1, & \text{if } U_{ij}[n] > \theta_{ij}[n] \\ 0, & \text{Otherwise.} \end{cases}$$

The threshold mechanism is described as

$$\theta_{ij}[n] = e^{-\alpha\theta}.\theta_{ij}[n-1] + V_\theta Y_{ij}[n].$$

When neuron fires $(Yij[n] = 1)$, the dynamic threshold $(\theta_{ij}[n])$ increases starting from its value in the previous iteration $(\theta_{ij}[n-1])$, and then, it decreases in time by the exponent $\alpha_\theta$ until the neuron fires again. Parameter $V\theta$ is necessary to adjust the effect of the neuron state to prevent the saturation and also to control the thresholding value. The term $\alpha\theta$ adjusts the level of decreasing the threshold value during the iteration process.

Considering the communications among one neuron and its surrounding, the interaction occurs when the output of the neuron is high $(Y = 1)$. When a neuron fires, an autowave (an autowave is defined as a normal propagating wave that does not reflect or refract [44], [48]) is generated and emanates from the source point to the rest of the image during the iteration process. This process generates a pulsing neuron, which has a sufficiently low value of threshold, in other parts of the image. Another important effect of the interneuron communication is synchronicity, which occurs when a neuron internal activity $U$ is close to the pulsing threshold $\theta$ and one or more of the surrounding neurons fire. In synchronicity, the contribution of the pulsing neighbors can affect (depending on the linking strength) the pulsing of the considered neuron.

In this paper, the parameters have been set to obtain the best results in the early iterations. The first and second iterations are responsible for the initialization and stabilization of the PCNN. Starting from the third one, the synchronicity and autowave mechanisms are triggered, and we can observe an improvement on the accuracy of the segmentation. In the range of third, fourth, and, in some cases, fifth iterations (Fig. 4), we can visually detect the best results; over the sixth iteration, the results are rough, and in the long run, the PCNN saturates, which means that it becomes insensitive to the parameter evolutions during the iterations.

## III. Experimental Results

In order to test the efficiency of the proposed approach, we used Envisat ASAR and ERS2 SAR data. ERS-2 SAR and Envisat-ASAR operate in C-band (4–8 GHz and $\lambda$ 3.75–7.5 cm). ERS-2 SAR images of the precision image (PRI) product have a pixel size of 12.5 m × 12.5 m, with a swath width of 100 km. Envisat ASAR images include the Image Mode (IM) and Wide Swath Mode (WSM) products. The IM product is similar to the PRI product of the ERS-2 SAR, while the WSM product has a spatial resolution of 150 m, with a swath width of 450 km.

The data set has been categorized into four groups (Table I) based on different types of dark spot and different sea statuses (Fig. 5). After the calibration process, subimages containing

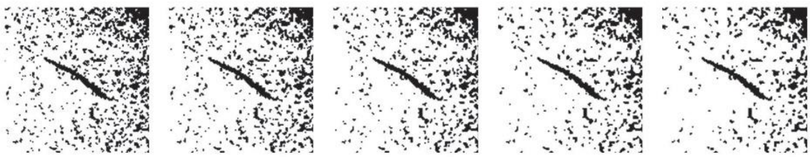

Fig. 4. Output images at different iterations which represent some segment or edge information of the input image.

TABLE I
DARK-SPOT TYPE CATEGORIES BASED ON DIFFERENT TYPES OF DARK SPOTS AND DIFFERENT SEA STATUSES

| Dark spot types | Description |
|---|---|
| Massive Well-Defined Dark Spot | A massive dark spot located within a homogeneous background where the boundary between the dark spot and the surrounding water is very clear |
| Linear Well-Defined Dark Spot | A linear dark spot located within a homogeneous background where the boundary between the dark spot and the surrounding water is very clear (eg. Oil spills discharged by ships) |
| Massive Not Well-Defined Dark Spot | A massive dark spot within a homogeneous background where the boundary between the dark feature and the surrounding water is not well defined |
| Linear Not Well-Defined Dark Spot | A linear dark spot within a homogeneous background where the boundary between the dark feature and the surrounding water is not well defined |

anomalies were extracted to make extraction and image interpretation more expedient. The test data set contains 40 images with 256 $\times$ 256 pixels (around 4 km$^2$) and 20 images with 512 $\times$ 512 pixels (around 36 km$^2$). This 60-image data set contains all potential anomalies detected under a variety of sea conditions.

Standard radar image preprocessing procedures using the Next ESA SAR Toolbox version 4C-1.1 software were applied to the images. This included radiometric calibration to generate a backscatter ($\sigma^0$) image and geometric correction to georeference the input images into the Universal Transverse Mercator projection with the World Geodetic System 1984 as datum.

The first column of Fig. 5 shows the original images after preprocessing. The results of WMM filter and PCNN segmentation are presented in the second and third columns (Fig. 5), respectively. In the fourth column of Fig. 5, the final results after postprocessing have been shown. A well-defined massive dark spot and a linear dark spot located within a homogeneous background where the boundary between the dark spot and the surrounding water is very clear are displayed in the first and second rows, respectively. The third and fourth rows show the detection of a not well-defined massive dark spot and a linear dark spot within a homogeneous background (the boundary between the dark feature and the surrounding water is not well defined) [14], [19]. Visual inspection shows that the proposed approach achieves acceptable detection results under a variety of conditions.

We applied the WMM approach to all 60 test images using the filtering intensity $P = 0.7$ and a window of dimension $3 \times 3$ surrounding the pixel to be filtered to estimate $y_z$ and $\beta_z$. These values were obtained where the best visual detection results were achieved. Using kernel sizes of 5 $\times$ 5, 7 $\times$ 7, and 9 $\times$ 9 gives us results where the edges of the objects (darks spots) have been blurred, so in these cases, we have the image with the texture information destroyed.

The segmentation task is based on the PCNN approach. In this neural network model, the setting of the parameters ($\alpha_L$, $\alpha_F$, $\alpha_\theta$, $V_L$, $V_F$, $V_\theta$, and $\beta$) represents the fundamental task in the phase of the design project because it must have the capability, and sensitivity, to fit at the dynamics range of the backscattering values in the scene. The parameter values need some adjustment according to the type of data. However, no further tuning is, in general, necessary once the sensor (Envisat, COSMO-SkyMed, TerraSAR-X, RADARSAT-1, ScanSAR, etc.) and the product (Wide Swath, Spotlight, Strip map, etc.) are defined. The best visual detection results are the results where the WMM model removes the noisy pixels in the images while preserving texture information.

In this experimental work, a unique best setting has been obtained for both Envisat and ERS products using the following parameter values: $\alpha_L = 0.3$, $\alpha_F = 1$, $\alpha_\theta = 1$, $V_L = 0.6$, $V_F = 0.8$, $V_\theta = 1.2$, and $\beta = 0.4$. The 3 $\times$ 3 square matrices of synaptic weights $M$ and $W$ are defined with a linking radius $r = 1.5$; therefore, the considered pixel receives linking inputs from the eight neighbors. The weighting factor for a linking input is $1/d^2$, where $d$ is defined as the Euclidean distance from the considered pixel. For every elaboration, the iteration which produces the most accurate binary segmentation among the sequence of output is often the third or fourth, leading to fast processing time, in the range from 2 to 5 s.

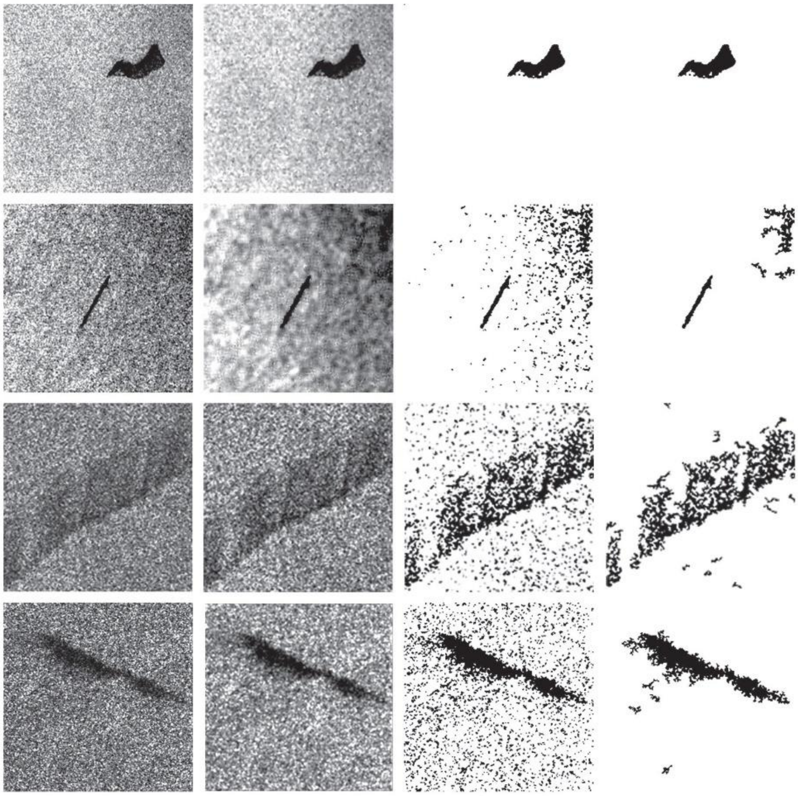

Fig. 5. Results of the proposed approach on four typical examples. (First column) Original SAR images after preprocessing. (Second column) WMM filtering. (Third column) PCNN results. (Fourth column) Final results after postprocessing.

After applying PCNN, some regions may have been incorrectly detected as dark spots. A very simple filtering process is used to eliminate these false targets as the post-processing step. By using this filter, all of the objects with the area less than 20 pixels are omitted from the processed image.

For accuracy assessment, from each subimage, 500 pixels have randomly been selected, and then, labeling is made by visual interpretation. The distance for measuring commission error and omission error is set as 1 pixel. The results have been compared with the results of the thresholding algorithm (applied to the same data set), which is a very popular method in this field, and also with the results of the latest method in the literature presented by Shu *et al.* [14] to demonstrate the effectiveness of the proposed approach.

In the Shu *et al.* model, intensity threshold segmentation is applied to each window which is passed through the entire SAR image. Pixels with intensities below the threshold are regarded as potential dark-spot pixels, while the others are potential background pixels. Then, the density of the potential background pixels is estimated using kernel density estimation. Pixels with densities below a certain threshold are the real dark-spot pixels. At the last step, they used a contrast threshold to eliminate false targets [14].

The average accuracy applied to the whole test data set is 93.53%, with a standard deviation of 3.8, whereas the accuracy

TABLE II
AVERAGE VALUES OF COMMISSION AND OMISSION ERRORS (IN PERCENT) ACHIEVED BY WMM AND PCNN FOR DIFFERENT GROUPS OF DATA

| | MinOm | MaxOm | MeanOm | St.DevOm | MinCm | MaxCm | MeanCm | St.DevCm |
|---|---|---|---|---|---|---|---|---|
| Well-Defined | 1.82 | 4.00 | 3.02 | 0.67 | 1.65 | 4.00 | 2.75 | 0.67 |
| Linear Well-Defined | 1.82 | 4.00 | 2.99 | 0.73 | 1.80 | 4.00 | 2.67 | 0.69 |
| Massive Well-Defined | 1.82 | 3.80 | 3.05 | 0.64 | 1.65 | 3.90 | 2.83 | 0.67 |
| Not Well-Defined | 6.25 | 15.12 | 9.90 | 2.25 | 8.20 | 14.20 | 11.00 | 1.84 |
| Linear Not Well-Defined | 6.25 | 15.00 | 9.63 | 2.36 | 8.20 | 13.60 | 10.32 | 1.88 |
| Massive Not Well-Defined | 7.77 | 15.12 | 10.18 | 2.22 | 9.40 | 14.20 | 11.70 | 1.59 |
| Linear Dark Spot | 1.82 | 15.00 | 6.31 | 3.80 | 1.80 | 1.36 | 6.49 | 4.15 |
| Massive Dark Spot | 1.82 | 15.12 | 6.62 | 3.98 | 1.65 | 14.20 | 7.26 | 4.69 |

TABLE III
AVERAGE VALUES OF THE ACCURACIES FOR DIFFERENT TYPES OF ANOMALIES

| | Min % | Max % | Mean % | St.Dev |
|---|---|---|---|---|
| Well-Defined | 96.0 | 98.18 | 96.97 | 0.67 |
| Linear Well-Defined | 96.00 | 98.18 | 97.00 | 0.73 |
| Massive Well-Defined | 96.20 | 98.18 | 96.94 | 0.64 |
| Not Well-Defined | 84.88 | 93.75 | 90.09 | 2.25 |
| Linear Not Well-Defined | 85.00 | 93.75 | 90.36 | 2.36 |
| Massive Not Well-Defined | 84.88 | 92.23 | 89.81 | 2.22 |
| Linear Dark Spot | 85.00 | 98.18 | 93.68 | 3.79 |
| Massive Dark Spot | 84.88 | 98.18 | 93.38 | 3.98 |

of the same data set segmented by the thresholding method is 67%. In the worst case, an accuracy of 84.88% was produced. The results of the accuracy assessment applied to the different types of anomalies are displayed in Tables II and III. As can be seen, the approach achieves satisfactory results on the well-defined dark spots than the not well-defined ones. The average accuracy for the well-defined dark spots is 96.97%, with a standard deviation of 0.67 and 2.75% commission error average, versus 90.09% with a standard deviation of 2.25 and 11.00% commission error average for the not well-defined ones, whereas in Shu' s work [14], the average commission error for the well-defined dark spots is 5.5%, versus 10.8% for the not well-defined ones, and the average omission error is 3.7% for the well-defined dark spots, compared to 12.1% for the not well-defined ones.

The approach generates almost a similar accuracy on the well-defined linear dark spots and the well-defined massive dark spots, but the commission errors on the linear dark spots are fewer compared to the massive dark spots. The average accuracies are 93.68%, with 6.49% and 6.31% commission and omission error averages, and 93.38%, with 7.26% and 6.62% commission and omission error averages, for the linear and massive dark spots, respectively, whereas in Shu's work [14], the average commission and omission errors for the linear dark spots are 9.4% and 10.5%, compared to 5.4% and 2.9% for the massive dark spots, respectively. The worst accuracies are 85.00% with 13.60% commission error and 84.88% with 14.20% commission error, which are obtained for the not well-defined linear dark spots and the not well-defined massive dark spots.

It is necessary to identify the situations where the proposed approach generates poor accuracy and to see why this method failed to work correctly in those cases. In general, the accuracy decreases in some cases because of the Wide Swath products and the strong variation of the incidence angle from near to far range which affects the dynamic range of digital numbers. Fig. 6 illustrates two typical examples. In Fig. 6 (first row), our approach failed because a very fresh oil spill is presented in a bright background and the contrast in some sections is too low. In Fig. 6 (second row), our approach failed because the background is heterogeneous and a large number of false alarms occur on the images after applying PCNN. Moreover, most of the false alarms are interconnected and difficult to remove using postprocessing without affecting the detection of the real dark spot.

Based on the authors' knowledge, the fastest method which has been reported in the literature is the spatial density thresholding model presented by Shu *et al.* with the speed of 11 s [14]. Another example is the marked point process model, presented by Li and Li [19], which takes about half an hour to complete dark-spot detection on a $512 \times 512$ image using a MATLAB software.

Also, the support vector machine method presented by Mercier and Girard-Ardhuin [25] takes about a minute to complete dark-spot detection on a $512 \times 512$ image using a 1.8-GHz Linux laptop. Dark-spot detection by the proposed approach with a $512 \times 512$ image can be completed in about 7 s on a personal computer with an Intel Pentium dual-core, a speed of 2.2 GHz, and a RAM memory of 2.00 GB, which is much faster than some existing methods in the literature. This might have a significant impact on the reduction of the computational burden when large data sets need to be processed.

## IV. CONCLUSION

In the present paper, an attempt has been made to demonstrate the power of using the combination of WMM and PCNN as an automated method for dark-spot detection in SAR imageries. To test the capability of the proposed approach, we have applied it to a data set containing 60 Envisat and ERS2

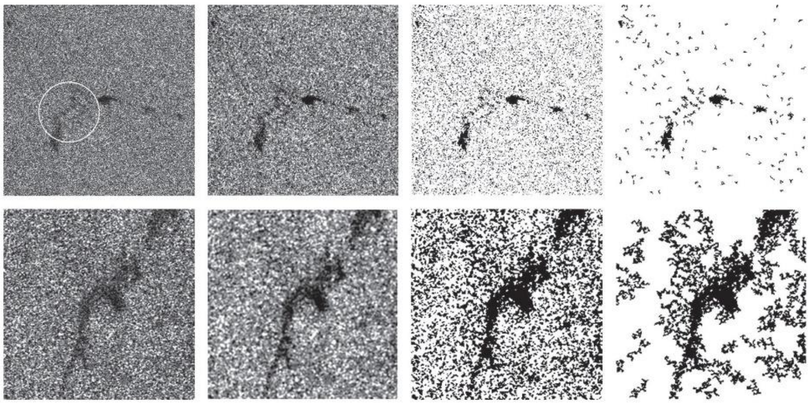

Fig. 6. Results of the proposed approach. The first row is an example where a very fresh oil spill is presented in a homogeneous background, and the second row is an example where a not well-defined dark spot is located in a very heterogeneous background (wind speed and sea state cause this heterogeneity).

images which cover all potential anomaly cases. The same parameters were used for all the test images.

The average accuracy for the overall data set was 93.66%, and the average computational time for a detection window was 7 s using IDL software. To study the detectability of different types of dark spots, we have divided the test data set into four groups. Results showed that this approach works best when the dark spots are well-defined or are located within a homogeneous background. It is less effective when the dark spots are not well defined or are located within a heterogeneous background. Overall, the results demonstrate that the proposed approach for dark-spot detection is effective, fast, and robust. Further research is necessary to improve the accuracy of dark-spot detection when the dark spots are not well defined. The proposed approach can be applied to the future spaceborne C-band SAR which will replace Sentinel-1 mission, just with some parameter adjustments based on the type of data.

## Acknowledgment

The authors would like to thank Prof. D. Fernandes, Head of the Telecommunications Department, Centro Técnico de Aeronáutica (CTA)—Instituto Tecnológico de Aeronáutica (ITA), Brazil, for his valuable cooperation and helpful suggestions. Data were provided by the European Space Agency on Cat-1 proposal numbers 1418 and 13926.

## References

[1] W. H. Alpers and A. Espedal, "Oils and surfactants," in *Synthetic Aperture Radar Marine User's Manual*, R. J. Christopher and J. R. Apel, Eds. Washington, DC, USA: US Dept. Commerce, 2004.

[2] P. Verma, A. R. Wate, and S. Devotta, "Simulation of impact of oil spill in the ocean—A case study of Arabian Gulf," *Environ. Monit. Assess.*, vol. 146, no. 1–3, pp. 191–201, Nov. 2008.

[3] R. H. Goodman. *Application of the Technology in the Remote Sensing of Oil Slicks*, A. E. Lodge, Ed. Hoboken, NJ, USA: Wiley, 1989.

[4] M. Fingas. *The Basics of Oil Spill Cleanup.* Boca Raton. FL, USA: Lewis Publ., 2001.

[5] C. Brekke and A. H. S. Solberg, "Oil spill detection by satellite remote sensing," *Remote Sens. Environ.*, vol. 95, no. 1, pp. 1–13, Mar. 15, 2005.

[6] G. Ferraro, S. Meyer-Roux, O. Muellenhoff, M. Pavliha, J. Svetak, D. Tarchi, and K. Topouzelis, "Long term monitoring of oil spills in European seas," *Int. J. Remote Sens.*, vol. 30, no. 3, pp. 627–645, Feb. 2009.

[7] A. T. Jones, M. Thankappan, G. A. Logan, J. M. Kennard, C. J. Smith, A. K. Williams, and G. M. Lawrence, "Coral spawn and bathymetric slicks in synthetic aperture radar (SAR) data from the Timor Sea, North-West Australia," *Int. J. Remote Sens.*, vol. 27, no. 10, pp. 2063–2069, May 2006.

[8] M. Thankappan, N. Rollet, C. J. H. Smith, A. Jones, G. Logan, and J. Kennard, "Assessment of SAR ocean features using optical and marine survey data," presented at the ENVISAT Symp., Montreux, Switzerland, Apr. 23–27, 2007. [Online]. Available: https://earth.esa.int/envisatsymposium/proceedings/contents.html

[9] F. Nirchio, M. Sorgente, A. Giancaspro, W. Biamino, E. Parisato, R. Ravera, and P. Trivero, "Automatic detection of oil spills from SAR images," *Int. J. Remote Sens.*, vol. 26, no. 6, pp. 1157–1174, Mar. 2005.

[10] V. Karathanassi, K. Topouzelis, P. Pavlakis, and D. Rokos, "An object-oriented methodology to detect oil spills," *Int. J. Remote Sens.*, vol. 27, no. 23, pp. 5235–5251, Dec. 2006.

[11] I. Keramitsoglou, C. Cartalis, and C. T. Kiranoudis, "Automatic identification of oil spills on satellite images," *Environ. Modell. Softw.*, vol. 21, no. 5, pp. 640–652, May 2006.

[12] A. H. S. Solberg, C. Brekke, and P. O. Husoy, "Oil spill detection in RADARSAT and Envisat SAR images," *IEEE Trans. Geosci. Remote Sens.*, vol. 45, no. 3, pp. 746–755, Mar. 2007.

[13] F. Del Frate, A. Petrocchi, J. Lichtenegger, and G. Calabresi, "Neural networks for oil spill detection using ERS-SAR data," *IEEE Trans. Geosci. Remote Sens.*, vol. 38, no. 5, pp. 2282–2287, Sep. 2000.

[14] Y. M. Shu, J. Li, H. Yousif, and G. Gomes, "Dark-spot detection from SAR intensity imagery with spatial density thresholding for oil-spill monitoring," *Remote Sens. Environ.*, vol. 114, no. 9, pp. 2026–2035, Feb. 2010.

[15] J. Lichtenegger, G. Calabresi, and A. Petrocchi, "Detection and discrimination between oil spills and look-alike," in *XIX ISPRS Congress, XXXIII*, 2000, pp. 193–200.

[16] R. Solberg and N. A. Theophilopoulos, "ENVISYS—A solution for automatic oil spill detection in the Mediterranean," in *Proc. 4th Int. Conf. Remote Sens. Marine Coastal Environ.*, 1997, pp. 3–12.

[17] A. Solberg, G. Storvik, R. Solberg, and E. Volden, "Automatic detection of oil spills in ERS SAR images," *IEEE Trans. Geoci. Remote Sens.*, vol. 37, no. 4, pp. 1916–1924, Jul. 1999.

[18] L. Chang, Z. S. Tang, S. H. Chang, and Y. L. Chang, "A region-based GLRT detection of oil spills in SAR images," *Pattern Recognit. Lett.*, vol. 29, no. 14, pp. 1915–1923, Oct. 2008.
[19] Y. Li and J. Li, "Oil spill detection from SAR intensity imagery using a marked point process," *Remote Sens. Environ.*, vol. 114, no. 7, pp. 1590–1601, Jul. 15, 2010.
[20] S. Derrode and G. Mercier. "Unsupervised multiscale oil slick segmentation from SAR images using a vector HMC model," *Pattern Recognit.*, vol. 40, no. 3, pp. 1135–1147, Mar. 2007.
[21] S. Y. Wu and A. K. Liu, "Towards an automated ocean feature detection, extraction and classification scheme for SAR imagery," *Int. J. Remote Sens.*, vol. 24, no. 5, pp. 935–951, Jan. 2003.
[22] A. K. Liu, C. Y. Peng, and S. Y. Chang, "Wavelet analysis of satellite images for coastal watch," *IEEE J. Ocean Eng.*, vol. 22, no. 1, pp. 9–17, Jan. 1997.
[23] G. Benelli and A. Garzelli. "Oil-spills detection in SAR images by fractal dimension estimation," in *Proc. IGARSS*, Hamburg, Germany, Jun. 28–Jul. 2 1999, pp. 218–220.
[24] M. Marghany, M. Hashim, and A. P. Cracknell, "Fractal dimension algorithm for detecting oil spills using RADARSAT-1 SAR," in *Proc. LNCS*, 2007, pp. 1054–1062.
[25] G. Mercier and F. Girard-Ardhuin, "Partially supervised oil-slick detection by SAR imagery using kernel expansion," *IEEE Trans. Geosci. Remote Sens.*, vol. 44, no. 10, pp. 2839–2846, Oct. 2006.
[26] K. Topouzelis, V. Karathanassi, P. Pavlakis, and D. Rokos, "Detection and discrimination between oil spills and look-alike phenomena through neural networks," *ISPRS J. Photogramm. Remote Sens.*, vol. 62, no. 4, pp. 264–270, Sep. 2007.
[27] K. Topouzelis, V. Karathanassi, P. Pavlakis, and D. Rokos, "Dark formation detection using neural networks," *Int. J. Remote Sens.*, vol. 29, no. 16, pp. 4705–4720, Aug. 2008.
[28] K. Topouzelis, D. Stathakis, and V. Karathanassi, "Investigation of genetic algorithms contribution to feature selection for oil spill detection," *Int. J. Remote Sens.*, vol. 30, no. 3, pp. 611–625, Feb. 2009.
[29] J. A. Karvonen, "Baltic Sea ice SAR segmentation and classification using modified pulse-coupled neural networks," *IEEE Trans. Geosci. Remote Sens.*, vol. 42, no. 7, pp. 1566–1574, Jul. 2004.
[30] K. N. Topouzelis, "Oil spill detection by SAR images: Dark formation detection, feature extraction and classification algorithms," *Sensors*, vol. 8, no. 10, pp. 6642–6659, Oct. 2008.
[31] N. Bartsch. K. Grüner, W. Keydel, and F. Witte, "Contribution to oil spill detection and analysis with radar and microwave radiometer: Results of the Archimedes II campaign," *IEEE Trans. Geosci. Remote Sens.*, vol. GE-25, no. 6, pp. 677–690, Nov. 1987.
[32] H. Hühnerfuss. W. Alpers. H. Dannhauer, M. Gade, P. A. Lange, V. Neumann, and V. Wismann, "Natural and man-made sea slicks in the North Sea investigated by a helicopter-borne 5-frequency radar scatterometer," *Int. J. Remote Sens.*, vol. 17. no. 8. pp. 1567–1582, May 1996.
[33] J. H. Hielm, *NIFO Comparative Trials, in The Remote Sensing of Oil Slicks*, A. E. Lodge, Ed. Chichester, U.K.: Wiley, 1989.
[34] E. E. Kuruoglu and J. Zerubia, "Modeling SAR images with a generalization of the Rayleigh distribution," *IEEE Trans. Image Process.*, vol. 13, no. 4, pp. 527–533, Apr. 2004.
[35] M. Sekine and Y. Mao, *Weibull Radar Clutter*. London, U.K.: IEE Press, 1990.
[36] J. S. Lee, L. Jurkevich, P. Dewaele, P. Wambacq, and A. Oosterlinck, "Speckle filtering of synthetic aperture radar images: A review," *Remote Sens. Rev.*, vol. 8, no. 4. pp. 313–340. Feb. 1994.
[37] D. Fernandes, "Segmentation of SAR images with Weibull distribution," in *Proc. IGARSS*. 1998. pp. 24–26.
[38] D. Fernandes. "Weibull texture filter (WTF) for SAR images," in *Proc. IGARSS*, 2001, pp. 642–644.
[39] R. Eckhorn, H. J. Reitboeck, M. Arndt, and P. Dicke. "Feature linking via synchronization among distributed assemblies: Simulations of results from cat visual cortex," *Neural Comput.*, vol. 2, no. 3, pp. 293–307, Sep. 1990.
[40] T. Lindblad and J. M. Kinser. *Image Processing Using Pulse-Coupled Neural Networks*. Berlin, Germany: Springer-Verlag, 2005.
[41] Z. Wang, Y. Ma, F. Cheng, and L. Yang, "Review of pulse-coupled neural networks," *Image Vis. Comput.*, vol. 28, no. 1, pp. 5–13, Jan. 2010.
[42] Y. Ma. L. Liu, K. Zhan, and Y. Wu, "Pulse-coupled neural networks and one-class support vector machines for geometry invariant texture retrieval," *Image Vis. Comput.*, vol. 28, no. 11, pp. 1524–1529, Nov. 2010.
[43] F. Palazzo, D. Latini, V. Baiocchi, F. Del Frate, F. Giannone, D. Dominici, and S. Remondiere, "An application of COSMO-SkyMed to coastal erosion studies," *Eur. J. Remote Sens.*, vol. 45, pp. 361–370, 2012.
[44] F. Del Frate, D. Latini, C. Pratola, and F. Palazzo, "PCNN for automatic segmentation and information extraction from X-band SAR imagery," *Int. J. Image Data Fusion*, vol. 4, no. 1, pp. 75–88, Mar. 2013.
[45] W. W. Chang, L. Guo, Z. Y. Fu, and K. Liu, "Hyperspectral multi-band image fusion algorithm by using pulse coupled neural networks," *J. Infrared Millim. Waves*, vol. 29, no. 3, pp. 205–209, Jun. 2010.
[46] W. Huang and Z. L. Jing, "Multi-focus image fusion using pulse coupled neural network," *Pattern Recognit. Lett.*, vol. 28, no. 9, pp. 1123–1132, Jul. 2007.
[47] Q. Liu, Y. D. Ma, S. G. Zhang, and W. S. He, *Image Target Recognition Using Pulse Coupled Neural Networks Time Matrix*. Beijing, China: Beijing Univ. Aeronaut. Astronaut. Press, 2007.
[48] L. F. Shang, Z. Yi, and L. P. Ji, "Binary image thinning using autowaves generated by PCNN," *Neural Process. Lett.*, vol. 25, no. 1, pp. 49–62. Feb. 2007.

**Alireza Taravat** received the M.Sc. degree in geoinformatics from Pune University, Pune, India, in 2010. He is currently working toward the Ph.D. degree in geoinformation at Tor Vergata University, Rome, Italy.

Since February 2013, he has been a Research Assistant with the D.I.C.I.I Department, University of Rome "Tor Vergata." He was involved in the best ideas challenge in European earth observation competition 2012. He has acted as Principal Investigator in remote sensing projects supported by the European Space Agency. His main research activities include remote sensing, image processing, and analysis of multitemporal data, data fusion, machine learning, target detection, and feature extraction. In particular, his interests are related to algorithm development for target detection and classification in ocean remote sensing applications.

**Daniele Latini** was born in Rome, Italy, in 1983. He received the Laurea degree in telecommunication engineering from the University of Rome "Tor Vergata," Rome, in 2010, where he is currently working toward the Ph.D. degree in geoscience and remote sensing.

Since 2010, he has been working in the field of remote sensing with the Earth Observation Laboratory, Tor Vergata. contributing to projects funded by the European Space Agency and the Italian Space Agency. He is a Visiting Student Researcher with the Jet Propulsion Laboratory, California Institute of Technology, Pasadena, CA, USA. His main research interests are synthetic aperture radar (SAR) remote sensing exploiting the potential of new generation satellites (COSMO-SkyMed and TerraSAR-X) using approach based on neural networks, polarimetry, and DInSAR techniques. He focused his activities on monitoring marine environment and coastal area, particularly ship detection, oil-spill detection, coastline erosion phenomena, and subsidence effects due to water seepage.

**Fabio Del Frate** (M'03–SM'09) received the Laurea degree in electronic engineering and the Ph.D. degree in computer science from the Tor Vergata University, Rome, Italy, in 1992 and 1997, respectively.

From September 1995 to June 1996, he was a Visiting Scientist with the Research Laboratory of Electronics, Massachusetts Institute of Technology, Cambridge, MA, USA. In 1998 and 1999, he was a Research Fellow with the European Space Research Institute, European Space Agency (ESA), Frascati, Italy. He is currently a Research Professor with the Tor Vergata University, where he teaches courses on applied electromagnetics and remote sensing. He has acted and is the Principal Investigator in several remote sensing projects supported by the ESA. He is the author or coauthor of more than 100 proceedings and journal papers with a special focus on the applications of neural networks to remote sensing inversion problems.

Dr. Del Frate has been a session organizer and a member of technical committees in different international conferences about remote sensing. He has been a Guest Editor of the European Association for Signal Processing *Journal on Advances in Signal Processing*, and he serves as an Associate Editor of the IEEE GEOSCIENCE AND REMOTE SENSING LETTERS.